INTERCALATION OF SULFUR IN EPITAXIAL GRAPHENE ON RUTHENIUM(0001) STUDIED BY MEANS OF SCANNING TUNNELING MICROSCOPY AND SPECTROSCOPY

Tesis doctoral presentada por

Ramón Bernardo Gavito

Para optar al título de doctor en Ciencias Físicas

Departamento de Física de la Materia Condensada

Universidad Autónoma de Madrid

Madrid, 2015

Tesis presentada para optar al grado de Doctor en Ciencias Físicas

Directores de tesis:

Dr. Daniel Granados Ruiz

Prof. Rodolfo Miranda Soriano

Universidad Autónoma de Madrid
Departamento de Física de la Materia Condensada

Instituto Madrileño de Estudios Avanzados
Nanociencia

A Punky, Floyd y Elena

TABLE OF CONTENTS

TABLE OF CONTENTS ..... **I**

RESUMEN ..... **III**

ABSTRACT ..... **V**

LIST OF ACRONYMS USED IN THIS TEXT ..... **VII**

1 INTRODUCTION AND MOTIVATION **1**

1.1 GRAPHENE: PROPERTIES AND APPLICATIONS 1
1.2 PRODUCTION OF GRAPHENE 2
1.3 INTERCALATION OF ELEMENTS UNDERNEATH GRAPHENE 3
1.4 MOTIVATION 3
1.5 OUTLINE OF THIS THESIS 4
1.6 REFERENCES 4

2 EXPERIMENTAL METHODS AND SET-UPS **9**

2.1 SCANNING TUNNELING MICROSCOPY 9
2.1.1 Basics *9*
2.1.2 STM theory *9*
2.2 SCANNING TUNNELING SPECTROSCOPY 11
2.3 SAMPLE CHARACTERIZATION TECHNIQUES (LEED/AES) 12
2.4 INSTRUMENTATION 14
2.4.1 General description *15*
2.4.2 Fast entry chamber and tip preparation chamber *15*
2.4.3 Sample preparation chamber *16*
2.4.4 VT-STM chamber *17*
2.4.5 LT-STM chamber *18*
2.5 REFERENCES 18

3 STRUCTURAL PROPERTIES OF S/RU(0001) **21**

3.1 S/RU(0001) SAMPLE PREPARATION 21
3.2 (2X2) AND ($\sqrt{3}$X$\sqrt{3}$)R30° RECONSTRUCTIONS OF S/RU(0001) 22
3.3 DOMAIN-WALL PHASE OF S/RU(0001) 27
3.4 C(2X4) RECONSTRUCTION OF S/RU(0001) 33
3.5 CONCLUSIONS 35
3.6 REFERENCES 36

4 INTERCALATION OF SULFUR IN GRAPHENE/RU(0001) **39**

4.1 INTRODUCTION 39
4.1.1 Graphene/Ru(0001) *39*
4.1.2 Intercalation of elements in graphene/Ru(0001) *41*
4.2 GRAPHENE/S/RU(0001) SAMPLE PREPARATION 42
4.2.1 Graphene on Ruthenium(0001) sample preparation *42*
4.2.2 Intercalation of sulfur in graphene/Ru(0001) *43*
4.3 INTERCALATED SULFUR DOMAIN-WALLS IN GRAPHENE/RU(0001) 43
4.3.1 Influence of the moiré superstructure in the DW structure of graphene/S/Ru(0001) *48*
4.4 INTERCALATED C(2X4) SULFUR DOMAINS 54
4.5 TOPOLOGICAL DEFECTS IN DW-INTERCALATED GRAPHENE/S/RU(0001) 58
4.6 CONDUCTANCE RESONANCES IN GRAPHENE/S/RU(0001) AND GRAPHENE/RU(0001) AFTER EXPOSURE TO H_2S 63
4.7 CONCLUSIONS 69
4.8 REFERENCES 69

5 STRIPED GRAIN BOUNDARIES IN SULFUR-INTERCALATED GRAPHENE: FORMATION AND MANIPULATION 77

5.1 STRIPED GRAIN BOUNDARIES SPONTANEOUS FORMATION IN GRAPHENE/S/RU(0001) 77
5.2 FABRICATION AND MANIPULATION OF GRAIN BOUNDARIES IN GRAPHENE/RU(0001) AND GRAPHENE/S/RU(0001) 84
5.3 CONCLUSIONS 91
5.4 REFERENCES 91

CONCLUSIONES GENERALES 93

GENERAL CONCLUSIONS 95

APPENDIX A – LIST OF MATERIAL PROPERTIES 97

A.1 REFERENCES 98

APPENDIX B – RECIPROCAL SPACE REPRESENTATION OF THE DIFFERENT STRUCTURES APPEARING IN S/RU(0001) AND GRAPHENE/S/RU(0001) 98

B.1 S/RU(0001) 103
B.2 GRAPHENE/S/RU(0001) 108

RESUMEN

En esta tesis se estudia la interacción del sulfuro de hidrógeno (H_2S) con el grafeno crecido epitaxialmente sobre el plano basal del rutenio (Ru(0001)). El crecimiento de las muestras y su caracterización se realizó mediante microscopía y espectroscopia de efecto túnel (STM/STS) en ultra alto vacío (UHV). Parte de la caracterización se realizó a baja temperatura y se utilizaron de manera complementaria otras técnicas de caracterización en UHV.

El grafeno epitaxial sobre Ru(0001) (grafeno/Ru(0001)) se crece mediante descomposición catalítica de etileno en condiciones de UHV. El grafeno/Ru(0001) muestra una interacción intensa entre el grafeno y el sustrato que resulta en una modulación topográfica y electrónica en forma de patrón de moiré debido a la pequeña diferencia en el parámetro de red de ambos. El grafeno así crecido está fuertemente anclado al Ru(00001) y altamente dopado (tipo-n), perdiendo su carácter semimetálico y su característica relación de dispersión lineal.

Las imágenes de STM demuestran que la exposición de grafeno/Ru(0001) a H_2S resulta en la intercalación de azufre entre el grafeno y el sustrato. Los experimentos sugieren que se produce mediante la formación de defectos puntuales en la superficie del grafeno. Los átomos de azufre intercalados se estructuran formando diferentes reconstrucciones que son descritas y analizadas. Para complementar la descripción geométrica de las estructuras que forma el azufre intercalado, se han realizado experimentos de adsorción de azufre en Ru(0001) sin la capa de grafeno epitaxial.

Las diferentes reconstrucciones de la capa de azufre intercalado en el sistema estudiado alteran las propiedades del grafeno que hay sobre ella. La densidad superficial de átomos de azufre y sus características geométricas reducen la interacción del grafeno con el Ru(0001) en diferente medida, como evidencia la reducción en la corrugación del patrón de moiré en los experimentos de STM.

Para analizar en más detalle la influencia de las diferentes configuraciones del azufre sobre las propiedades del sistema se realizaron experimentos de STS a baja temperatura que muestran la aparición de una serie de resonancias equiespaciadas en torno al nivel de Fermi tras la exposición a H_2S. El desplazamiento de estos picos a mayores energías con el aumento de la densidad de azufre sugiere la reducción del dopaje del grafeno intercalado con respecto al grafeno/Ru(0001). Su origen no ha podido ser establecido, pero se proponen posibles explicaciones para su aparición.

Por último, se llevaron a cabo experimentos de manipulación de la superficie de grafeno/S/Ru(0001) utilizando la punta del STM. Cuando la densidad de la capa intercalada permite la movilidad del azufre se ha conseguido crear patrones geométricos desplazando los átomos intercalados de manera que se recupera la interacción entre el grafeno y el Ru(0001) en zonas concretas. Las estructuras así creadas tienen tamaños nanométricos y son estables a temperatura ambiente.

ABSTRACT

This thesis studies the interaction of hydrogen sulfide (H_2S) with graphene epitaxially grown on the basal plane of ruthenium (Ru(0001)). Sample growth and characterization is carried out by means of scanning tunneling microscopy and spectroscopy (STM/STS) in ultra-high vacuum (UHV) conditions. Part of the characterization was done at low temperature, and complementary UHV characterization techniques were also used.

Epitaxial graphene on Ru(0001) (graphene/Ru(0001)) is grown by catalytic decomposition of ethylene in UHV conditions. Graphene/Ru(0001) shows a strong interaction between graphene and its substrate that results in a topographic and electronic modulation emerging as a moiré pattern due to the lattice mismatch between both materials. The resulting graphene layer is strongly bound to Ru(0001) and highly doped (n-type), losing its semi-metallic character and its characteristic linear dispersion relation.

STM images show that exposing graphene/Ru(0001) to H_2S results in the intercalation of sulfur between graphene and its substrate. The experiments suggest that intercalation occurs via the formation of local defects in the graphene's surface. The intercalated sulfur atoms are structured forming different reconstructions which are described and analyzed. In order to complement the geometrical description of the intercalated sulfur layer, experiments on the adsorption of sulfur on Ru(0001) have been carried out.

The different reconstructions of the intercalated system alter the properties of the graphene layer on top. The surface density of sulfur atoms and their geometrical characteristics reduce the interaction between graphene and Ru(0001) in different ways, as it is evident from the corrugation reduction of the moiré in STM experiments.

In order to get a deeper insight on the influence of the geometrical configurations of sulfur on the system's properties we performed low-temperature STS experiments. They show the emergence of a series of evenly spaced resonances close to the Fermi level after H_2S exposure. The shift of these resonances towards higher energies with increasing sulfur density suggest the reduction of the doping of the intercalated graphene with respect to graphene/Ru(0001). Their origin is not clear, but some possible explanations are suggested.

Lastly, manipulation experiments were carried out using the STM tip. When the density of the intercalated layer is low enough to allow for the sulfur mobility, geometric patterns have been drawn on the surface by moving the intercalated atoms in such a way that the strong graphene-Ru interaction is recovered at specific places. The so-created structures have lateral sizes in the nanometer range and are stable at room temperature.

LIST OF ACRONYMS USED IN THIS TEXT

AES – Auger electron spectroscopy

AFM – Atomic force microscope/microscopy

ARPES – Angle resolved photo-emission spectroscopy

CVD – Chemical vapor deposition

DOS – Density of states

DW – Domain wall(s)

DDW – Dense domain wall(s)

DFT – Density functional theory

FCC – Face centered cubic

FER – Field-emission resonance(s)

FET – Field-effect transistor

FFT – Fast Fourier transform

GFET – Graphene field-effect transistor

GIC – Graphite intercalation compound

HCP – Hexagonal close packed

HOPG – Highly-oriented pyrolytic graphite

ILC – Intercalation layered compound

LDOS – Local density of states

LEED – Low-energy electron diffraction

LHe – Liquid helium

LN_2 – Liquid nitrogen

LT-STM – Low-temperature scanning tunneling microscope

QMS – Quadrupole mass spectrometer

QW – Quantum well

RT – Room temperature

SHDW – Superheavy domain wall(s)

STM – Scanning tunelling microscope/microscopy

STS – Scanning tunelling spectroscopy

TEM – Transmission electron microscope/microscopy

UHV – Ultra-high vacuum

UPS – Ultra-violet photoemission spectroscopy

VT-STM – Variable-temperature scanning tunneling microscope

XPS – X-ray photoemission spectroscopy

1 INTRODUCTION AND MOTIVATION

This chapter introduces some basic concepts about the outstanding properties of graphene and the state of the art of its production techniques. The main discoveries on intercalated graphene systems are also discussed briefly. This introduction is intended to serve as a starting point for the reading of this thesis, which deals with the intercalation of sulfur in graphene epitaxially grown on the basal plane of a ruthenium substrate (graphene/S/Ru(0001)). The outline and motivation of the thesis is described at the end of the chapter.

1.1 GRAPHENE: PROPERTIES AND APPLICATIONS

The physical realization of graphene supposed a revolution in the field of surface science, since it became the first obtained two-dimensional material. A new field of study in material science opened, and graphene's properties and application are being deeply investigated since its discovery [1].

From the point of view of materials, graphene can be considered single-layer graphite, which has been separated from the bulk by breaking the interlayer interaction. Geometrically it consists on a honeycomb array of carbon atoms which can be described as a triangular lattice with a base of two carbon atoms, or two intermixed triangular lattices. Each of the triangular lattices are inequivalent, the electrons of one of them being unable to intern into the other [2]. This gives rise to a pseudospin that makes graphene an interesting material in the field of spintronics due to the existence of valley polarization [3].

Graphene presents very good properties in many aspects, being the most striking of them the electronic properties. It has very high carrier mobility (over $10^4 cm^2/V \cdot s$), making it an excellent conductor [4], but it also can behave as a semiconductor under certain conditions. This behavior comes from its particular band structure, which is linear around de Fermi level in the K and K' points of the two inequivalent triangular lattices, with the valence and conduction bands crossing in the Dirac point, a singularity in the density of states that granted graphene the category of zero-band-gap semiconductor. Doping graphene by changing the substrate, adding impurities or by introducing more graphene layers can change its band structure and open a finite band gap in its electronic structure. These properties, mainly the high carrier mobility and the possibility of tailoring the band-gap shape and energy size, make it a good candidate for improving electronic devices such as p-n junction diodes and field effect transistors (FETs). Graphene field effect transistors (GFETs) have been already developed in laboratories and show a promising horizon [5] [6].

Optical properties of pristine graphene are also in the scope of current research. It presents an absorption coefficient of near 2.3% [7], which is quite large considering it is only one atom thick. This absorption coefficient depends exclusively on the fine structure constant [8]. Absorption in the terahertz regime has attracted special interest, and plasmons in graphene absorb over 13% [9] of the incoming radiation at those energies. For these reason graphene has been proposed as a good candidate to produce biological sensors [10] [11], terahertz radiation detectors [12] [13] and terahertz oscillators [14]. These optical properties will depend on different parameters, such as the grade of disorder or the substrate [15], as the interaction of graphene with other materials can alter its electronic structure and open a forbidden energy gap between its valence and conduction bands.

The mechanical properties of graphene are also very good in terms of its Young's modulus, which is in the order of 1TPa [16], very close to that of the carbon nanotubes. Inclusion of graphene platelets in ceramic matrixes has successfully increased the strength and fracture toughness of the composite material [17].

Even the magnetic properties of graphene have attracted interest in the last years due to its unexpected behavior. Substrate induced ferromagnetism of monolayer graphene [18] and room-temperature ferromagnetic order was found in reduced graphene oxide sheets [19]. In the last example, this effect is attributed to the existence of defects and topological structures inducing a long-range coupling of the spin units. The imbalance of the two sublattices of graphene due to vacancies has also lead to predict that zig-zag edges of graphene nanoislands and ribbons present a spontaneous magnetization [20]. Scanning tunneling spectroscopy (STS) of 7,7,8,8-tetracyano-p-quinodimethane (TCNQ) molecules on graphene/Ru(0001) show Kondo resonances modulated by the graphene-Ru(0001) interaction [21]; the electronic moiré pattern that appears in graphene deposited on Ru(0001) [22] gives rise to the appearance of a magnetic moment in an otherwise non-magnetic molecule.

1.2 PRODUCTION OF GRAPHENE

One of the main challenges regarding the use of the different properties of graphene and the actual implementation of its potential properties involves the production of pristine graphene layers on the desired substrate, using a reproducible technique that gives a good yield of material with the required lateral dimensions.

Mechanical exfoliation of graphene was the first technique used to isolate this novel material in order to measure its physical properties. It is a cheap technique that results in good quality graphene flakes, but its use is restricted to academic purposes only, since the graphene obtained this way usually results in cascaded flakes of different thicknesses, the width of the monolayer regions spanning only over a few nanometers. Also, the material is obtained in random places across the substrate. It is a good technique for research laboratories, since the amount of material required for study and prototyping is small, and it is not restricted to graphene, but it serves for other 2D-materials. Technical advances have improved the graphene yield, width and site-selectivity of this technique, but it is still not good enough for production purposes.

Chemical exfoliation of graphene and other 2D-materials presents similar problems as the previous method. Graphene flakes are introduced in specific solvents that break the interlayer bonds and end up dispersed in a solution. Deposition of the flakes by sedimentation or solvent evaporation gives a higher yield of monolayers, but the site selectivity is still an issue.

The most promising techniques regarding graphene production for industrial and commercial purposes are those based in carbon deposition by chemical interaction of gas flows, i.e., chemical vapor deposition (CVD) techniques. One of the most successful approaches involves the CVD growth of graphene in copper foils; with the proper parameters, a good quality graphene can be grown in rather wide areas, even in the centimeter range. The graphene thus obtained is usually coated by an electronic- or photo-resist so it can then be transferred to an arbitrary substrate by dissolving the copper foil in a specific etchant; developing and removing the resist leaves the graphene deposited in the desired substrate. The resulting graphene is mostly single layered, but it usually presents a large amount of grains of different orientation, dictated by the grains of the original copper substrate.

Another CVD growth technique widely used in materials science involves the catalytic decomposition of hydrocarbons in presence of transition metals parting from UHV conditions.

Allowing a flow of hydrocarbons, such a methane or ethylene, into a UHV chamber at which a catalytic metal at high temperature is present, the C-H bonds are broken and the carbon radicals form a graphene lattice in the surface of the substrate. This technique has been successfully applied in metals such as ruthenium, iridium, rhodium and platinum, and results in a good quality graphene which is single crystalline in wide areas of the substrate. Nonetheless, this method is restricted to a very specific family of substrates, and transfer of the obtained graphene into arbitrary substrates has not been achieved.

1.3 INTERCALATION OF ELEMENTS UNDERNEATH GRAPHENE

Intercalation layered compounds (ILCs) have been developed during the last decades since they are composites that provide improved or new properties with respect to the original materials. ILCs are fabricated out of different layered materials [23], being graphite one of the most used. There is a wide variety of graphite intercalation compounds (GIC) with different emerging properties such including ferromagnetism [24] [25], zero-field pseudo-Landau levels [26] and superconductivity [27] [28] [29].

The irruption of graphene in surface science opened a completely new field of study due to its outstanding properties [1] [30]. Intercalation of different species between graphene and its supporting substrate has been suggested in order to alter the properties of the systems as happened with graphite and the GICs. Epitaxial graphene grown on catalytic metals results in wide single-layer graphene domains with a very good crystallinity [31] [32] [33]. Although the materials and techniques involved are very expensive for production it is perfect for research, since it allows getting high-quality graphene in different substrates with different interaction intensities. For example, epitaxial graphene on Ru(0001) (graphene/Ru(0001)) results in a strongly interacting system that disrupts the properties of pristine graphene and develops a moiré pattern with a periodicity of ~3nm [22] [34]. This moiré disrupts the electronic landscape [31] [35]. On the other hand, graphene on Ir(111) or Pt(111) interacts weakly and its properties are closer to those of free-standing graphene [33] [36].

Intercalation materials based on epitaxial graphene have been developed using many different substrates and intercalation species [37] [38] [39] [40] [41] [42]. As a result, the properties of these systems are altered mostly due to changes on the graphene-substrate interaction, and the interaction of graphene with the intercalated species.

1.4 MOTIVATION

This thesis deals with the intercalation of sulfur in previously grown graphene/Ru(0001) samples. In particular, we use Ru(0001) as a substrate, which results in a highly crystalline graphene monolayer. Graphene/Ru(0001) presents very regular a moiré emerging from the lattice mismatch of graphene and the substrate and a strong interaction between both of them, with a topographic and electronic periodicity of ~3nm. One of the main goals of this thesis is to obtain a method to effectively decouple graphene from Ru(0001) in order to obtain wide single-crystalline graphene samples. The properties emerging from the interaction of the double periodicity of graphene/Ru(0001) with that of the different reconstructions of the intercalated sulfur layer is also an important motivation for this thesis.

1.5 OUTLINE OF THIS THESIS

This thesis presents the following structure:

Chapter 2 describes the experimental methods and set-ups used during the course of this thesis. First, an introduction to the basics of scanning tunneling microscopy (STM) and spectroscopy (STS) is presented, as they are the main techniques used in this thesis. They give very local information on the topographic and electronic properties of the surface under study. The second section of this chapter describes the two ultra-high vacuum systems used in this thesis, one of them containing a variable-temperature STM and the other a low-temperature STM.

Chapter 3 deals with the S/Ru(0001) system at different coverage ranges. We are interested in the different lattices sulfur can form when chemisorbed on ruthenium, since they will have an important influence in the properties of the intercalated system. The description of the samples preparation is followed by the study of these reconstructions by means of STM.

Chapter 4 is centered in the intercalation of sulfur in graphene/Ru(0001) and the properties of the intercalated system. The growth of graphene on Ru(0001) is described, followed by the sulfur-intercalation method used. STM and STS analysis of the resulting system is described in the following sections, centering in the differences of its properties as a function of the intercalated layer geometry.

Chapter 5 is devoted to the formation and manipulation of grain boundaries (GBs) in graphene/S/Ru(0001) that appear after annealing the samples. It starts describing the required conditions for the GBs to form and then its geometric properties are described. The end of this chapter deals with the deterministic manipulation of these GBs with the STM tip.

The general conclusions extracted from the present work are presented at the end of this thesis, followed by a list of the author publications and contributions to international conferences.

1.6 REFERENCES

[1] K. Novoselov, A. Geim, S. Morozov, D. Jiang, M. Katsnelson, I. Grrigorieva, S. Dubonos and A. Firsov, "Two-dimensional gas of massless Dirac fermions in graphene," *Nature,* vol. 438, pp. 197-200, 2005.

[2] A. Castro Neto, F. Guinea, N. Peres, K. Novoselov and A. Geim, "The electronic properties of graphene," *Review of Modern Physics,* vol. 81, pp. 109-161, 2009.

[3] A. Akhmerov and C. Beenakker, "Detection of valley polarization in graphene by a superconducting contact," *Physical Review Letters,* vol. 98, p. 157003, 2007.

[4] L. Ponomarenko, R. Yang, T. Mohiuddin, M. Katnelson, K. Novoselov, S. Morozov, A. Zhukov, F. Schedin, E. Hill and A. Geim, "Effekt of a high-κ environment on charge carrier mobility in graphene," *Physical Review Letters,* vol. 102, p. 206603, 2009.

[5] Y.-M. Lin, K. Jenkins, A. Valdes-Garcia, J. Small, J. Farmer and P. Avouris, "Operation of graphene transistors at gigahertz frequencies," *Nano Letters,* vol. 9, no. 1, pp. 422-426, 2009.

[6] Y.-M. Lin, C. Dimitrakopoulos, K. Jenkins, D. Farmer, H.-Y. Chiu, A. Grill and P. Avouris, "100-GHz transistors from wafer-scale epitaxial graphene," *Science,* vol. 327, no. 5966, p. 662, 2010.

[7] K. Mak, M. Sfeir, Y. Wu, C. Lui, J. Misewich and T. Heinz, "Measurement of the optical conductivity of graphene," *Physical Review Letters,* vol. 101, p. 196405, 2008.

[8] R. Nair, P. Blake, A. Grigorenko, K. Novoselov, T. Booth, T. Stauber, N. Peres and A. Geim, "Fine structure constant defines visual transparency of graphene," *Science,* vol. 320, p. 1308, 2008.

[9] L. Ju, B. Geng, J. Horng, C. Girit, M. Martin, Z. Hao, H. Bechtel, X. Liang, A. Zettl, Y. Shen and F. Wang, "Graphene plasmonics for tunable terahertz metamaterials," *Nature Nanotechnology,* vol. 6, pp. 630-634, 2011.

[10] Y. Liu, X. Dong and P. Chen, "Biological and chemical sensors based on graphene materials," *Chemical Society Reviews,* vol. 41, pp. 2283-2307, 2012.

[11] Kuila, T.; Bose, S.; Khanra, P.; Mishra, A.K.; Kim, N.H.; Lee, J.H., *Biosensors and Bioelectronics,* vol. 26, no. 12, pp. 4637-4648, 2011.

[12] T. Low and P. Avouris, "Graphene plasmonics for terahertz to mid-infrared applications," *ACS Nano,* vol. 8, no. 2, pp. 1086-1101, 2014.

[13] X. Cai, A. Sushkov, M. Jadidi, L. Nyakiti, R. Myers-Ward, D. Gaskill, T. Murphy, M. Fuhrer and H. Drew, "Plasmon-enhanced terahertz photodetection in graphene," *Nanoletters,* vol. 15, no. 7, pp. 4295-4302, 2015.

[14] F. Rana, "Graphene terahertz plasmon oscillators," *Transactions on nanotechnology,* vol. 7, no. 1, pp. 91-99, 2008.

[15] J. Dawlaty, S. Shivaraman, J. Strait, P. George, M. Chandrashekhar, F. Rana, M. Spencer, D. Veksler and Y. Chen, "Measurement of the optical absorption spectra of epitaxial graphene from terahertz to visible," *Applied Physics Letters,* vol. 93, p. 131905, 2008.

[16] C. Lee, X. Wei, J. Kysar and J. Hone, "Measurement of the elastic properties and intrinsic strength of monolayer graphene," *Science,* vol. 321, no. 5887, pp. 385-388, 2008.

[17] I. Ovid'ko, "Mechanical properties of graphene," *Reviews on Advanced Materials Science,* vol. 34, pp. 1-11, 2013.

[18] Z. Wang, C. Tang, R. Sachs, Y. Barlas and J. Shi, "Proximity-induced ferromagnetism in graphene revealed by the anomalous hall effect," *Physical Review Letters,* vol. 114, no. 1, p. 016603, 2015.

[19] Y. Wang, Y. Huang, Y. Song, X. Zhang, Y. Ma, J. Liang and Y. Chen, "Room-temperature ferromagnetism of graphene," *Nano Letters,* vol. 9, no. 1, pp. 220-224, 2009.

[20] J. Fernández-Rossier, "Magnetism in graphene nanoislands," *Physical Review Letters,* vol. 99, p. 177204, 2007.

[21] M. Garnica, D. Stradi, F. Calleja, S. Barja, C. Díaz, M. Alcamí, A. Arnau, A. Vázquez de Parga, F. Martín and R. Miranda, "Probing the site-dependent Kondo response of nanostructured graphene with organic molecules," *Nano Letters,* vol. 14, pp. 4560-4567, 2014.

[22] D. Stradi, S. Barja, C. Díaz, M. Garnica, B. Borca, J. Hinarejos, D. Sánchez-Portal, M. Alcamí, A. Arnau, A. Vázquez de Parga, R. Miranda and F. Martín, "Electron localization in epitaxial graphene on Ru(0001) determined by moiré corrugation," *Physical Review B,* vol. 85, p. 121404, 2012.

[23] M. Dresselhaus, Intercalation in layered materials, New York: Springer Science+Bussines Media, 1986.

[24] L. Ebert, "Intercalation compounds of graphite," *Annual Review of Materials Research,* vol. 6, pp. 181-211, 1976.

[25] T. Kaloni, M. Upadhyay Kahaly and U. Schwingenschlögl, "Induced magnetism in transition metal intercalated graphitic systems," *Journal of Materials Chemistry,* vol. 21, pp. 18681-18685, 2011.

[26] D. Guo, T. Kondo, T. Machida, K. Iwatake, S. Okada and J. Nakamura, "Observation of Lanndau levels in potassium-intercalated graphite under a zero magnetic field," *Nature Communications,* vol. 3, p. 1068, 2012.

[27] N. Hannay, T. Geballe, B. Matthias, K. Andres, P. Schmidt and D. MacNair, "Superconductivity in graphitic compounds," *Physical Review Letters,* vol. 14, no. 7, pp. 225-226, 1965.

[28] I. Belash, A. Bronnikov, O. Zharikov and A. Palnichenko, "On the superconducctivity of graphite intercalation compounds with sodium," *Solid State Communications,* vol. 64, no. 12, pp. 1445-1447, 1987.

[29] R. Al-Jishi, "Model for superconductivity in graphite intercalation compounds," *Physical Review B,* vol. 28, no. 1, pp. 112-116, 1983.

[30] N. Peres, F. Guinea and A. Castro Neto, "Electronic properties of disordered two-dimensional carbon," *Physical Review B,* vol. 73, p. 125411, 2006.

[31] A. Vázquez de Parga, F. Calleja, B. Borca, M. Passeggi Jr., J. Hinarejos, F. Guinea and R. Miranda, "Periodically rippled graphene: Growth and spatially resolved electronic structure," *Physical Review Letters,* vol. 100, p. 056807, 2008.

[32] J. Coraux, A. N'Diaye, M. Engler, C. Busse, D. Wall, N. Buckaine, F.-J. Meyer zu Heringdorf, R. van Gastel, B. Poelsema and T. Michely, "Growth of graphene on Ir(111)," *New Journal of Physics,* vol. 11, no. 023006, pp. 1-22, 2009.

[33] P. Sutter, J. Sadowski and E. Sutter, "Graphene on Pt(111): Growth and substrate interaction," *Physical Review B,* vol. 80, no. 245411, pp. 1-10, 2009.

[34] B. Wang, M. Caffio, C. Bromley, H. Früchtl and R. Schaub, "Coupling epitaxy, chemical bonding, and work function at the local scale in transition metal-supported graphene," *ACS Nano,* vol. 4, pp. 5773-5782, 2010.

[35] B. Borca, S. Barja, M. Garnica, D. Sánchez-Portal, V. Silkin, E. Chulkov, F. Hermanns, J. Hinarejos, A. Vázquez de Parga, A. Arnau, P. Echenique and R. Miranda, "Potential energy landscape for hot electrons in periodically nanostructured graphene," *Physical Review Letters,* vol. 105, p. 036804, 2010.

[36] I. Pletikosic, M. Kralj, P. Pervan, R. Brako, J. Coraux, A. N'Diaye, C. Busse and T. Michely, "Dirac cones and minigaps for graphene on Ir(111)," *Physical Review Letters,* vol. 102, no. 056808, pp. 1-4, 2009.

[37] J. Mao, L. Huang, Y. Pan, M. Gao, J. He, H. Zhou, H. Guo, Y. Tian, Q. Zou, L. Zhang, H. Zhang, Y. Wang, S. Du, X. Zhou, A. Castro Neto and H.-J. Gao, "Silicon layer intercalation of centimeter-scale, epitaxially grown monolayer graphene on Ru(0001)," *Applied Physics Letters,* vol. 100, p. 093101, 2012.

[38] Z. Zhou, B. Habenicht, Q. Guo, Z. Yan, Y. Xu, L. Liu and D. Goodman, "Graphene moiré structure grown on a pseudomorphic metal overlayer supported on Ru(0001)," *Surface Science,* vol. 611, pp. 67-73, 2013.

[39] L. Jin, Q. Fu, R. Mu, D. Tan and X. Bao, "Pb intercalation underneath a graphene layer on Ru(0001) and its effect on graphene oxidation," *Physical Chemistry Chemical Physics,* vol. 13, pp. 16655-16660, 2011.

[40] L. Huang, Y. Pan, L. Pan, M. Gao, W. Xu, Y. Que, H. Zhou, Y. Wang, S. Du and H.-J. Gao, "Intercalation of metal islands and films at the interface of epitaxialy grown graphene and Ru(0001) surfaces," *Applied Physics Letters,* vol. 99, p. 163107, 2011.

[41] C. Enderlein, Y. Kim, A. Bostwick, E. Rotenberg and K. Horn, "The formation of an energy gap in graphene on ruthenium by controlling the interface," *New Journal of Physics,* vol. 12, p. 033014, 2010.

[42] P. Sutter, J. Sadowski and E. Sutter, "Chemistry under cover: Tuning metal-graphene interaction by reactive intercalation," *Journal of the American Chemical Society,* vol. 132, pp. 8175-8179, 2010.

2 EXPERIMENTAL METHODS AND SET-UPS

2.1 SCANNING TUNNELING MICROSCOPY

Scanning tunneling microscopy (STM) is the main technique used in this thesis and the microscopes represent the most important part of our experimental system. In the following subsections a brief explanation of its working principles is introduced, followed by a more detailed theoretical description.

2.1.1 Basics

A STM consists in a tapered metallic tip which is placed into close proximity to the surface of conducting samples by means of a high precision piezoelectric positioning system. The magnitude the microscope measures is the tunneling current passing through the tip-sample gap when a voltage is applied between them. In order to track the tunneling current changes, the electronics require a highly sensitive current measuring system [1].

The positioning system consists in a piezoelectric scanning stage which is able to achieve picometric precision when applying high voltages between the different pairs of electrodes. It allows movement in the X-Y plane, as well as in the Z direction. The most common operation mode is the constant current mode, at which a feedback system controls the tip-sample distance by moving the scanner in the Z direction in order to keep the tunneling current constant, and recording the vertical displacement of the tip. The resulting image is formed by representing the vertical displacement of the tip at each point of the X-Y plane, and it represents a convolution between the actual topography of the sample and its electronic structure at a fixed voltage. The topographic images shown in this thesis are obtained using this operation mode.

2.1.2 STM theory

Most of the theoretical approaches to the tunneling process taking place in the tunnel junction of an STM system are based in the formalism developed by J. Bardeen [2] to explain the tunneling processes taking place in the metal-insulator-metal junctions. It allows explaining the current flowing between two tunneling electrodes from their wave functions and unperturbed energies. In the case of our STM, the two electrodes are the STM tip and the surface of the sample, and the insulating layer is the vacuum gap between them.

The tunneling current between the STM tip and the sample can be expressed in first order Bardeen's formalism by:

$$I = \frac{2\pi e}{\hbar} \sum_{\mu\nu} f(E_\mu)[1 - f(E_\nu + eV)]\left|M_{\mu\nu}\right|^2 \delta(E_\mu - E_\nu), \tag{2.1}$$

being $f(E)$ the Fermi-Dirac distribution, V the applied voltage between the tip and the surface, $M_{\mu\nu}$ the matrix element between μ states of the tip and ν states of the sample, and E_μ and E_ν the energies of the electronic states of tip and surface respectively. In this formalism, $M_{\mu\nu}$ depends exclusively on the wave functions of the tip (ψ_μ) and the surface (ψ_ν), and can be written as follows:

$$M_{\mu\nu} = \frac{\hbar}{2m} \int d\mathbf{S} \cdot \left(\psi_\mu^* \nabla\psi_\nu - \psi_\nu \nabla\psi_\mu^*\right), \tag{2.2}$$

the integral being performed over any plane within the tunneling barrier. J. Tersoff and D. R. Hamann [3] developed a theory of STM based on Bardeen's formalism that included the calculation of the wave functions of tip and sample. This allows predicting a quantitative value for the tunneling current. In their work they consider the surface a planar electrode, while the tip is modelled as a locally spherical potential in close proximity of the sample. In this approximation, the tip and surface wave functions have the form:

$$\psi_\mu = \frac{1}{\Omega_t^{1/2}} c_t k R e^{kR} (k|\mathbf{r} - \mathbf{r_0}|)^{-1} e^{-k|\mathbf{r}-\mathbf{r_0}|}, \tag{2.3}$$

$$\psi_\nu = \frac{1}{\Omega_s^{1/2}} \sum_{\mathrm{G}} a_{\mathrm{G}} exp\left[(k^2 + |\mathbf{k_G}|^2)^{1/2} z\right] exp(i\mathbf{k_G} \cdot \mathbf{x}), \tag{2.4}$$

where Ω_t and Ω_s are the tip and sample volumes, R the local radius centered in the curvature center of the tip ($\mathbf{r_0}$), $k = (2m\Phi)^{1/2}/\hbar$ is the decay length in vacuum, Φ the work function, and $\mathbf{k_G} = \mathbf{k}_\parallel + \mathbf{G}$ is the wave vector where $\mathbf{k}_\parallel$ is the surface Bloch wave vector of the states and $\mathbf{G}$ is a surface reciprocal lattice vector. Expanding the wave function of the tip in the same form as that of the surface and neglecting any angular dependence, the integral in the matrix element $M_{\mu\nu}$ can be evaluated and results:

$$M_{\mu\nu} = \frac{\hbar}{2m} \frac{4\pi}{k\Omega_t^{1/2}} k R e^{kR} \Psi_\nu(\mathbf{r_0}). \tag{2.5}$$

When $k_B T$ is small, i.e., at low temperatures, the Fermi-Dirac distribution can be approximated by the Heavyside step function, θ. This leaves the tunneling current:

$$I = \frac{32\pi^3}{\hbar k^4} e^2 V \Phi^2 R^2 e^{2kR} \frac{1}{\Omega_t} \sum_{\nu\mu} |\Psi_\upsilon(\mathbf{r_0})|^2 \delta\big(E_\mu - E_F\big) \delta(E_\nu - E_F). \tag{2.6}$$

The local density of states (LDOS) per energy interval of the tip and the sample can be expressed as:

$$\rho_t(E_F) = \frac{1}{\Omega_t} \sum_{\mu} \delta\big(E_\mu - E_F\big), \tag{2.7}$$

$$\rho_s(E_F, \mathbf{r_0}) = \sum_{\nu} |\Psi_\nu(\mathbf{r_0})|^2 \delta(E_\nu - E_F). \tag{2.8}$$

In the case of $\rho_s(E_F, \mathbf{r_0})$, we are considering the surface LDOS at the tip position $\mathbf{r_0}$. The tunneling current can be approximated as a function of the LDOS as:

$$I \propto \sum_{\nu} |\Psi_\nu(\mathbf{r_0})|^2 \delta(E_\nu - E_F) \equiv \rho_s(E_F, \mathbf{r_0}). \tag{2.9}$$

This approximation considers an atomically sharp tip with a constant LDOS. This results in the tunneling current being proportional to the LDOS of the surface. This model was extended by N.

Lang [4] considering both tip and sample as planar electrodes with and adsorbed atom on each of them, with a small bias voltage applied between both. In this approximation, the tunneling current in an energy window eV results:

$$I \propto \int_{E_F}^{E_F+eV} dE \rho_t(E-eV)\rho_s(E)T(z,E,eV). \tag{2.10}$$

In this approximation, the tunneling current depends in the LDOS of both tip and sample and on the transmission coefficient of an electron inside the tunneling barrier, $T(z,E,eV)$. The convolution of these three contributions is what makes the interpretation of STM images at fixed voltages so complicated. Analysis of the data obtained by scanning tunneling spectroscopy (STS), explained in detail in the next section, helps to overcome some of these difficulties.

2.2 SCANNING TUNNELING SPECTROSCOPY

The theoretical description of STM given in the previous section shows that it is a powerful tool in order to understand the local electronic properties of surfaces. It has subnanometric resolution in the three spatial dimensions and the measured current contains information on the LDOS of the surface below the tip. Scanning tunneling spectroscopy (STS) techniques push further the possibilities of the STM in order to get a deeper insight of the electronic properties of the studied surfaces.

We can consider two operation modes when performing STS experiments. When measuring the LDOS of the surface close to the Fermi level, we will use the **constant height** spectroscopy mode. At every point of the sample, the tip-surface distance is fixed by stabilizing the measured current at a specific bias voltage. Once the feedback has reached a stable point it is turned off, leaving the tip still at a certain height. A voltage sweep is performed, recording the tunneling current at each bias step. A modulation voltage combined with lock-in electronics allows us to simultaneously measure the derivative of the current signal; if lock-in techniques are not available, the numerical derivative can serve for the same purpose at the cost of resolution in energy. The resulting dI/dV curve gives us a spectrum proportional to the LDOS of the surface at the point below the tip. Repeating the same process at every point during a scan results in a LDOS map of the whole scanning area.

The tunneling current obtained this way can be calculated from equation 2.10. The transmission coefficient inside the integral can be written in the semi-classical Wentzel-Kramers-Brillouin (WKB) approximation as:

$$T(z,E,eV) = exp\left(-\frac{2z\sqrt{2\pi}}{\hbar}\sqrt{\left(\frac{\Phi_s+\Phi_t}{2}\right)+\left(\frac{eV}{2}\right)-E}\right), \tag{2.11}$$

which shows a transmission coefficient dependence on the applied tip-sample bias voltage V. This dependence on the bias voltage is the largest when $E=0$ for negative biases or when $E=eV$ for positive ones. In the case of positive bias voltages, the electrons close to the Fermi energy of the tip can cross the tunnel barrier into the unoccupied states of the surface; for negative biases the process is inverted, and the electrons close to the Fermi energy of the surface can jump into the unoccupied states of the tip. This considerations imply that STS can be used to probe the LDOS of the sample, but the resolution is higher for the unoccupied states of the surface ($eV>0$) than for the occupied ones ($eV<0$). Taking in account the expression for the transmission coefficient

given in equation 2.11 and the expression for the tunneling current in equation 2.10, it is easy to see that the derivative of the current signal in the constant height mode is proportional to the LDOS of the surface:

$$\frac{dI}{dV} \propto \rho_s \tag{2.12}$$

If the voltage range we want to measure is too large, the acquisition electronics can saturate, since the measured current can grow dramatically with voltage when new conduction channels are open. In order to overcome this limitation, a second operation mode is available, namely the **constant current** mode. In this case, the feedback is left connected while performing the bias sweeps, so the measured current will be set at a fixed value. All the events that would result in a current increase in the previously explained mode will be reflected in this case in the retraction of the tip, since the feedback system will try to separate it from the surface in order to keep the current constant. dZ/dV curves will then give information on the LDOS of the surface under the tip, but lateral resolution will suffer, since the tunneling gap grows wider every time the tip retracts.

The constant current mode is a spectroscopy method that allows us to probe different conduction channels that are not necessarily dependent on the LDOS of the sample. When the bias voltage is larger than the mean value of the work functions of the sample and the tip, it gives access to certain unoccupied states called field emission resonances (FERs). They are related to the image states of the surface and give information on the surface potential. The FERs where first observed in 1967 by A. J. Jason [5] by means of field ion microscopy, and the first time they were accessed via STM was in an experiment conducted by Binning et al. in 1985 [6]. There are many parameters influencing the position and FWHM of the FERs when probed by STM, such as the shape of the tip or the tip-surface distance [7], but it is a useful technique to obtain qualitative information on the variation of the surface potential of oxide films grown on metals [8], ionic films [9], or nanostructured surfaces such as Ag/Pt(111) [10] and graphene/Ru(0001) [11]. We will use this technique in the case of graphene/S/Ru(0001) in a similar fashion as in [11], since the moiré appearing in this system is similar to that of graphene/Ru(0001).

2.3 SAMPLE CHARACTERIZATION TECHNIQUES (LEED/AES)

Our experimental systems are equipped with four-grid electron diffractometers that allow us to characterize and check the condition of the samples before introducing them into the STM chamber. A four-grid electron diffractometer consists in an electron gun which is capable of projecting an electron beam of up to 30μA with energies ranging between 15 and 3500eV. An ensemble of electrostatic lenses allows focusing the beam into the sample. Four gold-plated molybdenum grids rest on a phosphorous screen. The electrons of the beam are collected in the phosphorous screen after interacting with the sample in order to obtain low energy electron diffraction (LEED) patterns. One of the grids is negatively biased below the acceleration voltage in order to filter the electrons undergoing inelastic processes, which constitute 99% of the reflected electrons [12] and do not contribute to the diffraction pattern.

LEED experiments use an electron beam of 50-500eV, an energy range at which the wavelength of the electrons is comparable to the interatomic distances of solids. The mean free path of electrons of these energies is just of a few atomic layers [12]. According to Huygens principle, the atoms in the outermost atomic layers should re-emit electrons when impinged by an incoming electron beam. The interference between the re-emitted electrons will only be constructive along those directions at which the difference between paths corresponds to an integer number of

wavelengths. Thus, the emitted electrons will only exit the sample in those well-defined directions, forming a diffraction pattern. Since both the electron gun and the screen vectors are perpendicular to the surface of the sample, the LEED pattern corresponds to the reciprocal lattices of the outermost layers in the planes parallel to the surface [12]. Figure 2-1 is a LEED pattern of graphene/S/Ru(0001) showing the diffraction patterns of graphene, Ru(0001) and one of the possible geometries of the intercalated sulfur layer.

The four-grid diffractometer also gives us the possibility to perform Auger electron spectroscopy (AES) experiments. To do so, the beam energy is set to 3000eV and the integrated electron current reaching the phosphorous screen is measured. One of the grids is set at a certain suppression voltage V_{sup} so the electrons reaching the screen are those in the range between V_{sup} and the energy of the beam. Applying a modulation voltage to another grid and using a lock-in amplifier, the derivative of the current signal is obtained, which is the current associated with the electrons with energy corresponding to V_{sup}. This way, by varying V_{sup} we obtain the energy spectrum of the electrons reaching the screen (Figure 2-2).

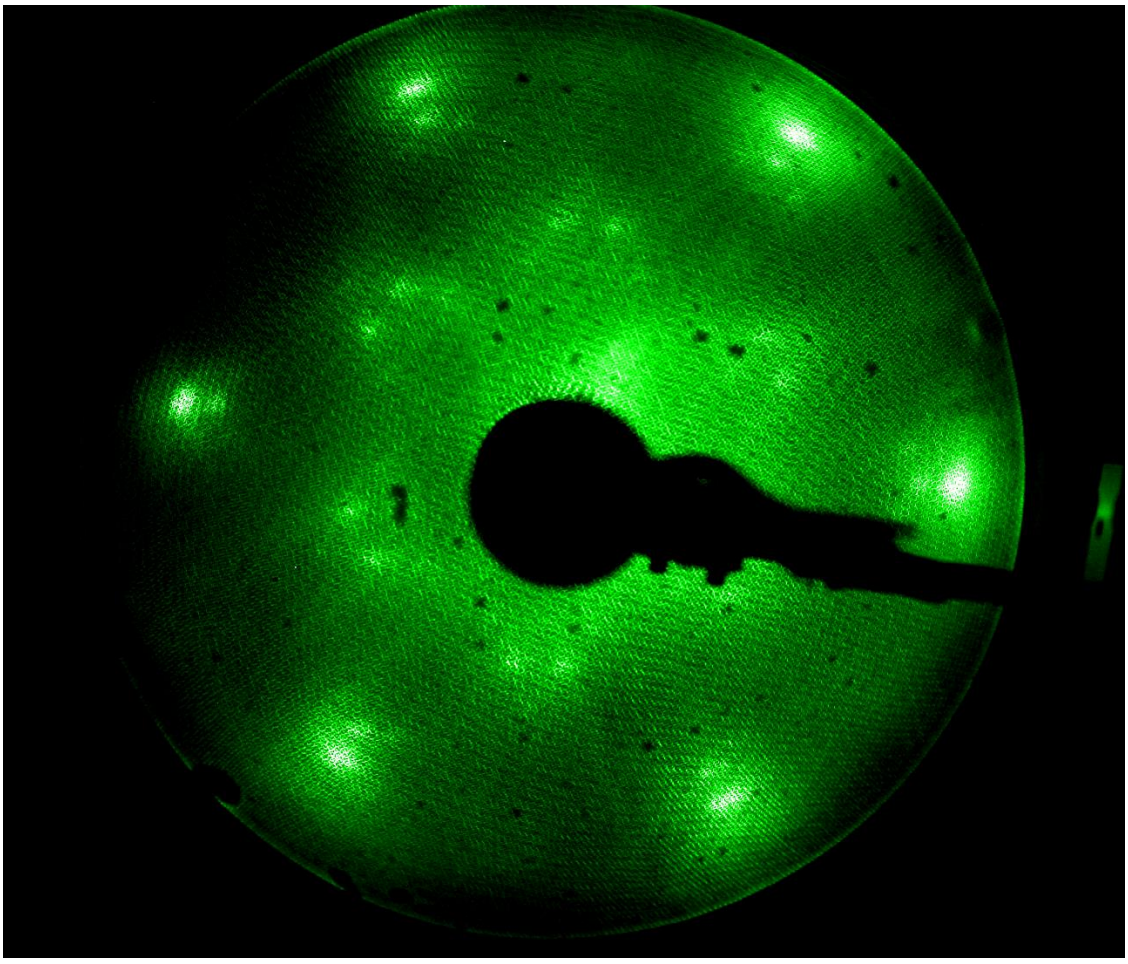

Figure 2-1 – Photography of the phosphorous screen showing the LEED diffraction pattern of a graphene/S/Ru(0001). In the image, the reciprocal lattices of the graphene honeycomb (outer spots), the Ru(0001) surface (one step closer to the center of the screen) and the dense-domain-wall reconstruction of sulfur (complex star-shaped spot pattern near the center of the screen) can be observed.

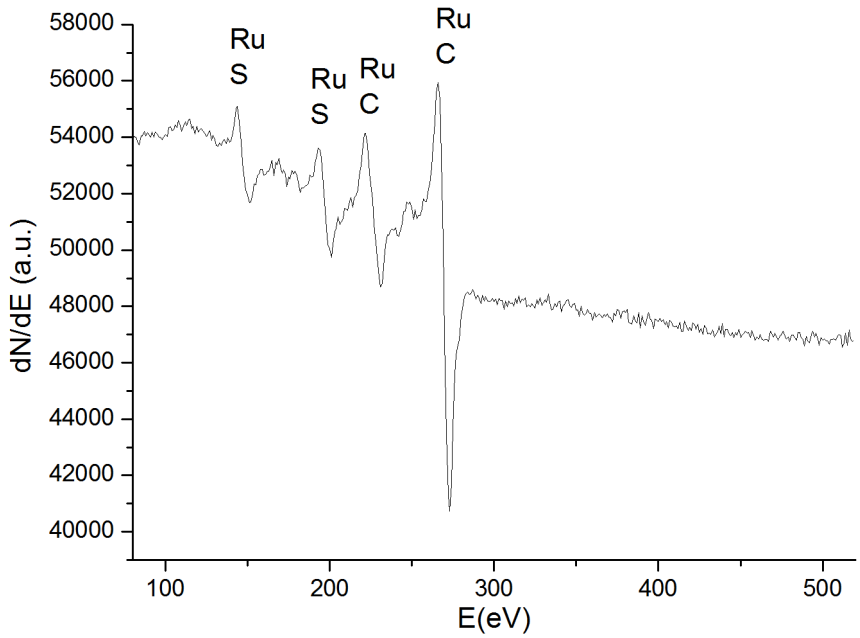

Figure 2-2 – Auger spectrum of a graphene/S/Ru(0001) sample. The energies characteristic peaks of ruthenium coincide with those of sulfur and carbon. The elastic peak has been removed from the graph.

AES spectra consist in a large peak corresponding to those electrons suffering an elastic process, and a long tail. Beneath the tail, certain peaks appear at the energies at which the electrons undergo one (primary electrons) or more (secondary electrons) inelastic processes. One of the possible inelastic processes an electron can experience when reaching a surface is the Auger process. The incoming electron extracts an electron from a deep level of an atom of the sample. A second electron from a less deep level falls into the first level and the energy liberated in the relaxation process extracts a third electron that escapes the sample at a well-defined energy that depends only in the energy difference of the two levels involved, which is characteristic for each atomic species. The energies involved in Auger processes are tabulated for energies between 10 and 2000eV, range at which the electron mean free path is of a few atomic layers [12], so the AES spectra give information on the chemical composition of the sample.

LEED experiments were used during this thesis to check the surface reconstructions of the S/Ru(0001) (see Chapter 3) and graphene/S/Ru(0001) (Chapter 4) samples before introducing them in the STM. AES spectra were performed in both S/Ru(0001) and graphene/S/Ru(0001) samples to check the composition of the samples and discard the presence of contaminants from different species that could be present in the vacuum chamber or embedded in the bulk ruthenium crystal. Further analysis was not possible since the characteristic peaks of ruthenium coincide in energy with those of sulfur and carbon [13].

2.4 INSTRUMENTATION

The experiments shown in this thesis have been carried on in two different UHV systems. The initial experiments regarding S/Ru(0001) and graphene/S/Ru(0001) growth, and the characterization of both systems by means or STM measurements at room temperature, were performed at a UHV system equipped with a variable-temperature STM (VT-STM) located at the Surface Physics Department of the Universidad Autónoma de Madrid (UAM). Once the growth of the samples with different parameter was understood and characterized at room temperature, STM and STS experiments at 77K and 4K were done in a different UHV chamber equipped with

a low-temperature STM (LT-STM) located at the Scanning Probe Microscopies and Surfaces Laboratory at the Madrid Institute for Advanced Studies in Nanoscience (IMDEA-Nanoscience). Three different ruthenium single crystals were used during the course of this thesis.

This section presents both experimental set-ups. Since these two systems share many characteristics (tip- and sample-preparation chambers), we will describe the common parts and highlight the differences between both systems, if any. The descriptions of each individual STM chamber are given at the end of the section.

2.4.1 General description

The design of both UHV systems was done by Dr. Juan José Hinarejos and was described thoroughly in the theses of Dr. Fabián Calleja [14] and Dr. Sara Barja [15]. Both UHV systems share the same basic structure, consisting in a fast entry chamber, a tip preparation chamber, a sample preparation chamber and a STM chamber. The design and fabrication of the fast entry and preparation chambers were carried on at the UAM. Both the VT-STM and LT-STM chambers are commercial systems from Omicron [16]. For the LT-STM we used the electronics provided by Omicron, while for controlling the VT-STM we used Omicron-compatible electronics designed by Specs [17]. Both systems are mounted on an aluminum frame resting on active pneumatic damping systems (Newport I-2000) to uncouple the systems from external vibrations.

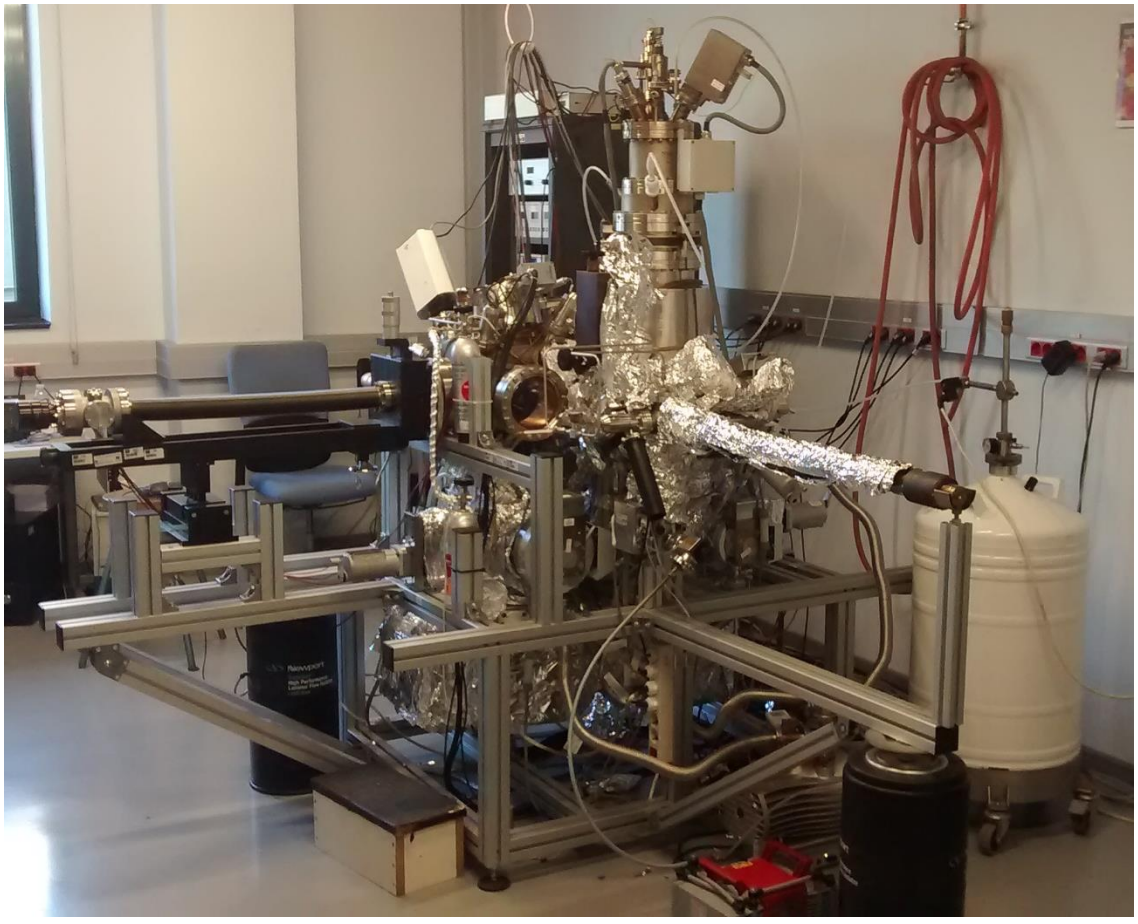

Figure 2-3 – LT-STM

2.4.2 Fast entry chamber and tip preparation chamber

The fast entry chamber is a small steel chamber that serves to insert end extract samples and tips from the systems without breaking the vacuum in the rest of the system. In order to

introduce/extract samples and tips from/to atmosphere, the chamber is equipped with a quick-access door. The chamber is pumped by a turbo molecular pump (Pfeiffer TMU 071P) backed by a membrane pump (Pfeiffer MVP 055-3). The transfer from the fast entry chamber to the tip- and sample-preparation chambers is achieved thanks to a magnetic transfer rod.

The tip preparation chamber is connected at one end to the fast entry chamber and at the other to the sample preparation chamber by a two gate valves. It is pumped by a turbo molecular pump (Pfeiffer TMU 261P) connected to a 2-stage piston pump (Pfeiffer XtraDry 150-2). The vacuum in the chamber is measured by a Bayard-Alpert pressure sensor (Edwards D02999380).

The STM tips are fabricated outside the chamber from a 99.99% purity tungsten polycrystalline wire (Ø0.4mm). The wires are then tapered by electrochemical etching in a 5M KOH solution. The tips thus fabricated are covered by a thick oxide layer that needs to be removed before starting any experiment. The tip is annealed in the tip preparation chamber by contacting it to a tantalum foil and passing current through it. Since the higher resistance in the circuit is located at the tip-Ta contact, we manage to heat the tip without damaging the tip holder. In order to clean the tip apex, it is sputtered with 2.5keV Ar^+ ions in the sample preparation chamber for thirty minutes.

The tip preparation chamber was designed for two purposes: anneal the sample and evaporate different materials to functionalize the tip. This last feature is used for specific purposes, such as performing spin-polarized experiments or shifting the work function of the tip. In the experiments conducted in this thesis there was no need for tip functionalization, so the role of the tip-preparation chamber is reduced to annealing the tip after introducing it to the UHV system and in order to clean it and reshape it in case it got damaged during some experiment.

2.4.3 Sample preparation chamber

The sample preparation chamber is equipped with the standard facilities used in UHV systems. These include a quadrupole mass spectrometer (QMS) (Pfeiffer Prisma 80), an ion gun (Specs IQE 11-A), gas inlets (Ar, O_2, N_2, C_2H_4, H_2S) controlled by leak valves, a LEED system equipped with AES capabilities (Omicron SpectaLEED), and several evaporators for different materials and molecules. In the VT-STM, this chamber is directly connected to the STM chamber and both of them are simultaneously pumped by a turbo molecular pump backed by a rotary pump, and an ionic pump. In the case of the LT-STM, these chambers are separated by a gate valve, and the sample preparation chamber is pumped by a 2-stage piston pump (Pfeiffer XtraDry 150-2), a turbo molecular pump (Pfeiffer TMU 512P) and an ionic pump (Gamma Vacuum). After baking and degassing the system, a Bayard-Alpert type vacuum gauge (ranging from $6\cdot10^{-3}$ to $4\cdot10^{-11}$mbar) indicates a base pressure of 10^{-10}mbar.

The chamber is equipped with an UHV manipulator which allows movement in three directions (X-Y-Z) and 360º rotation around the Z axis. Its purpose is to place and orientate the samples in front of the different preparation tools, and to translate it to and from the transfer rod and the STM chambers. The precision screws in the X-Y plane allow displacements of 0.5μm, while the precision in them Z axis is of 0.5mm.

The head of the manipulator is compatible with Omicron tip and sample holders and allows heating by electron bombardment, as it has a tungsten filament and the sample can be connected to high voltage sources via feedthroughs. Our sample preparations require Ar^+ ion sputtering, annealing and exposure to different gases (O_2, C_2H_4 and H_2S). The intrinsics of each preparation are given at their corresponding chapters (Chapter 3 for S/Ru(0001) and Chapter 4 for graphene/Ru(0001) and graphene/S/Ru(0001)).

2.4.4 VT-STM chamber

The VT-STM chamber is directly connected to the sample preparation chamber and both of them share the pumping system described above. The VT-STM stage presents a damping system, apart from the pneumatic support of the whole system, consisting in three springs from which the stage is suspended. The stage can be locked, so it is not hanging from the springs, in order to perform the transfer to and from the manipulator by means of a wobble stick present in the chamber. When it is left suspended, a series of radial copper plates intercalate with alternating magnets that give rise to eddy currents, preventing the stage to touch the chamber walls. This gives an extra isolation from external perturbations that result in an enhanced stability, allowing us to get resolutions down to a few picometers.

The variable temperature capabilities of this microscope are given by the combination of a Liquid helium (LHe) flow cryostat with a heating system integrated in the Omicron sample holders. The cryostat and the sample are thermally contacted by a copper braid, allowing us to control de cooling by the flow of LHe. Since the LHe flow introduces vibrations that can tamper the experiments, the helium flow is limited by stability considerations, and the lower temperature we can get without introducing too much vibrations is 70K. Rising the temperature above room-temperature is achieved by passing an electric current through the ceramic resistance integrated in the double-decker Omicron sample holders.

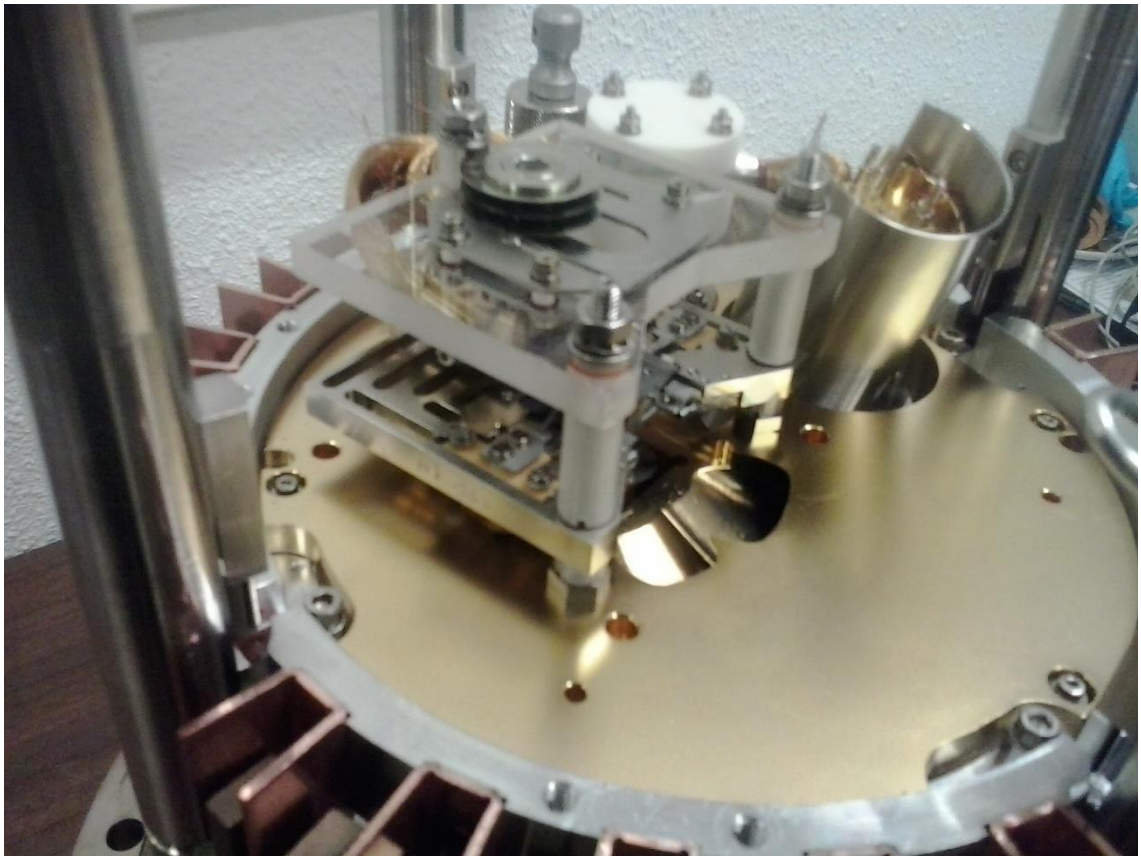

Figure 2-4 – VT-STM head.

Since we had a LT-STM at our disposal which could give us lower temperatures without reducing the resolution due to induced vibrations, we didn't use the cooling capabilities of the VT-STM and all the experiments carried on with it were performed at 300K. Lower temperature STM and STS experiments in this thesis are performed used the LT-STM described in the next subsection.

During the course of this thesis, we modified the head of the manipulator and the VT-STM so they could fit the standard sample holders used in the LT-STM and other equipment, instead of the massive double-decker sample holders. This allowed us to transfer samples between systems without needing to unweld and weld them again to the different sample holders, avoiding the risk of damaging the samples in the process.

2.4.5 LT-STM chamber

The LT-STM chamber is connected to the sample preparation chamber through a gate valve and, unlike in the VT-STM case, has its own pumping system. It consists in a turbo molecular pump (Pfeiffer TMU 261P) backed by a 2-stage piston pump (Pfeiffer XtraDry 150-2), plus a ionic pump (Gamma Vacuum). The base pressure obtained after bakeout is of 10^{-10}mbar, but the Bayard-Alpert gauge reads values in the 10^{-11}mbar range after cooling down to 4K.

In order to lower the temperature, the LT-STM chamber contains a cryostat that consists in a LHe bath cryostat which is surrounded by a liquid nitrogen (LN_2) bath cryostat. The LT-STM stage lies below the cryostat and is equipped with an additional damping system based on spring suspension and eddy current damping, very similar to that of the VT-STM. The combination of this damping system and the pneumatic support of the whole system, we get stability enough to take images with resolution in the picometer range. The whole stage has a lifting mechanism that can carry it to three different positions, namely, the cool position, where the stage is in direct thermal and mechanical contact with the LHe cryostat in order to assure the fast cooling of the sample; the exchange position, at which the stage is mechanically locked but it is not in thermal contact with the cryostat, is the position used to exchange tip and samples from the manipulator to the microscope and back; and the measuring position, at which the stage is released and left suspended, so the eddy current damping system allows for precision measurements. This cooling and isolation system gives the LT-STM thermal stability for up to 28h.

In the LT-STM chamber, but out of the cryostat, we have support facilities needed to carry on the experiments, such as a wobble stick to transfer the samples and tips to and from the LT-STM, and a sample carrousel with six storage positions used to store tips and samples for future experiments.

2.5 REFERENCES

[1] G. Binnig, H. Rohrer, C. Gerber and E. Weibel, "Surface studies by scanning tunneling microscpy," *Physical Review Letters,* vol. 49, no. 1, pp. 57-61, 1982.

[2] J. Bardeen, "Tunneling from a many-particle point of view," *Physical Review Letters,* vol. 6, no. 57, 1961.

[3] J. Tersoff and D. Hamann, "Theory of the scanning tunneling microscope," *Physical Review B,* vol. 31, no. 805, 1985.

[4] N. Lang, "Spectroscopy of single atoms in the scanning tunneling microscope," *Physical Review B,* vol. 34, no. 5947, 1986.

[5] A. Jason, "Field-induced resonance states at a surface," *Physical Review B,* vol. 156, no. 266, 1967.

[6] G. Binnig, K. Frank, H. Fuchs, N. García, B. Reihl, H. Rohrer, F. Salvan and A. Williams, "Tunneling spectroscopy and inverse photoemission: image and field states," *Physical Review Letters,* vol. 55, no. 991, 1985.

[7] J. Pascual, C. Corriol, G. Ceballos, I. Aldazabal, H.-P. Rust, K. Horn, J. Pitarke, P. Echenique and A. Arnau, "Role of the electric field in surface electron dynamics above the vacuum level," *Physical Review B,* vol. 75, p. 165326, 2007.

[8] E. Rienks, N. Nilius, H.-P. Rust and H.-J. Freund, "Surface potential of a polar oxide film: FeO on Pt(111)," *Physical Review B,* vol. 71, p. 241404, 2005.

[9] M. Pivetta, F. Patthey, M. Stengel, A. Baldereschi and W. Schneider, "Local work function moiré pattern on ultrathin ionic films: NaCl on Ag(100)," *Physical Review B,* vol. 72, p. 115404, 2005.

[10] P. Ruffieux, K. Ait-Mansour, A. Bendounan, R. Fasel, L. Patthey, P. Groning and O. Groning, "Mapping the electronic surface potential of nanostructured surfaces," *Physical Review Letters,* vol. 102, p. 086807, 2009.

[11] B. Borca, S. Barja, M. Garnica, D. Sánchez-Portal, V. Silkin, E. Chulkov, F. Hermanns, J. Hinarejos, A. Vázquez de Parga, A. Arnau, P. Echenique and R. Miranda, "Potential energy landscape for hot electrons in periodically nanostructured graphene," *Physical Review Letters,* vol. 105, p. 036804, 2010.

[12] A. Zangwill, Physics at Surfaces, Cambridge: Cambridge University Press, 1988.

[13] M. van Staden and J. Roux, "The superposition of carbon and ruthenium Auger spectra," *Applied Surface Science,* vol. 44, no. 4, pp. 259-262, 1990.

[14] F. Calleja, Influencia de la estructura electrónica local en las propiedades de las superficies y su estudio mediante microscopía de efecto túnel, Madrid: PhD. Thesis, Universidad Autónoma de Madrid, 2007.

[15] S. Barja, Grafeno epitaxial en metales de transición: Estudio mediante microscopía y espectroscopia de efecto túnel, Madrid: PhD Thesis, Universidad Autónoma de Madrid, 2012.

[16] Omicron NanoTechnology, GmbH, [Online]. Available: http://www.omicron.de.

[17] Specs, [Online]. Available: http://www.specs.de.

3 STRUCTURAL PROPERTIES OF S/RU(0001)

The starting point of our investigations regarding the intercalation of sulfur underneath graphene grown on Ru(0001) requires the characterization of S/Ru(0001). The structural and electronic properties of this system will influence the intercalated one. In this chapter we summarize the different structures that an adsorbed layer of sulfur can form on a Ru(0001) substrate as a function of coverage.

3.1 S/RU(0001) SAMPLE PREPARATION

In order to grow sulfur layers on Ru(0001) we expose the previously clean ruthenium single crystal to a controlled atmosphere of pure hydrogen sulfide (H_2S) starting from UHV conditions. Varying the partial pressure of H_2S and the exposure time we are able to control the sulfur coverage of the substrate surface, thus controlling the phase of the sulfur overlayer. Different variations of this method were previously used in [1] and [2], and results in a complex phase diagram of ordered phases of increasing density (Figure 3-1).

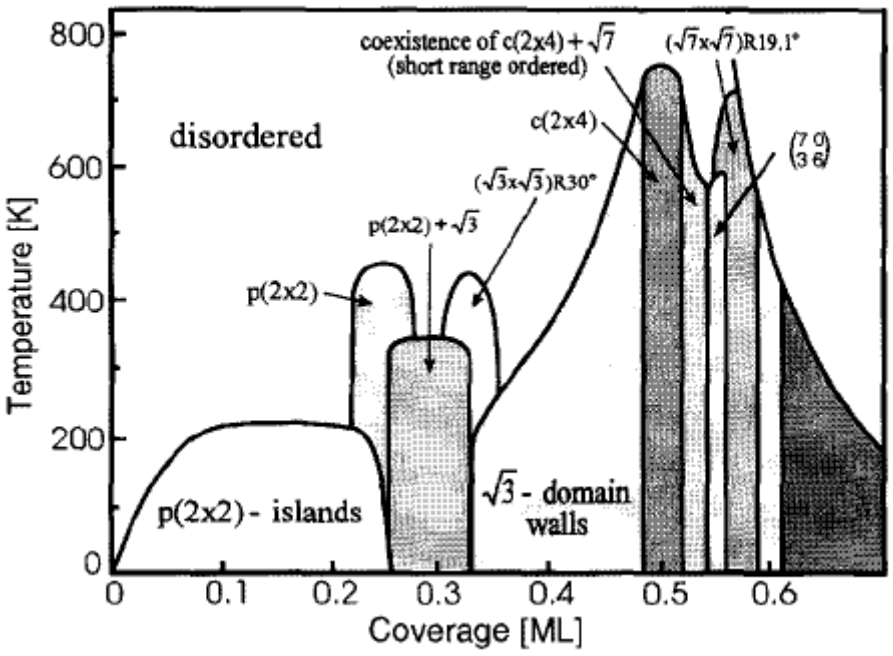

Figure 3-1 – Phase diagram of S/Ru(0001) obtained by LEED. The figure was extracted from [3]

We are especially interested in the transition between the hexagonal (2x2) and (√3x√3)R30º, and the rectangular c(2x4)-2S phases, which appear in the coverage range of $0.25<\theta<0.5$ and include a domain-wall (DW) mediated transition; for this reason we always perform the exposure at room temperature. Denser phases would require a higher deposition temperature (500K) because at higher coverages the sticking coefficient is reduced and extra energy is required both to break the H-S bonds, and to dissociate the trapped hydrogen in order to increase the adsorption efficiency [1].

We start cleaning and flattening the Ru(0001) substrate. To do so we use a standard preparation method involving three cycles of argon ion sputtering (acceleration voltage V_a=1.42kV, 10^{-6}mbar of Ar, 7 minutes) and posterior annealing at 1400K for 1 minute. After the sputtering-annealing cycles, the sample is annealed at 1150K in an oxygen atmosphere of 10^{-7}mbar for three minutes.

Annealing the sample in an oxygen atmosphere produces a thin layer of oxygen covering the whole Ru(0001) surface, preventing the formation of undesired graphene patches coming from the diffusion of carbon impurities present in the bulk ruthenium crystal. This process prevents any other contaminant to adsorb to the surface. After each annealing, a temperature flash of 1400K during thirty seconds favors desorption of oxygen [4].

After the last of these annealing cycles is completed we perform the exposure to the H_2S gas at room temperature. The pressure and time will depend on the particular phase we want to obtain. H_2S dissociates easily in the presence of clean ruthenium [1], so exposures as subtle as 10^{-8}mbar for 45 seconds result in the formation of layers close to a complete layer of the (2x2) reconstruction (θ=0.25). Saturation of the surface while exposing at room temperature always results in the formation of a complete c(2x4)-2S layer, without traces of higher density phases up to exposures of 10^{-6}mbar for 10 minutes. Figure 3-16, at the end of this chapter, shows the time and pressure ranges used to obtain the different phases.

3.2 (2x2) AND (√3x√3)R30° RECONSTRUCTIONS OF S/RU(0001)

The first ordered phase that results from the sulfur adsorption on the ruthenium basal plane forms a (2x2) reconstruction. It consists in a hexagonal lattice of sulfur atoms distributed along the three symmetry directions of the substrate with lattice constant double of that of ruthenium. A complete layer of this geometry corresponds to a coverage of θ=0.25 [5]. Increasing the coverage above that point leads to the formation of a denser commensurate phase, namely a (√3x√3)R30º reconstruction, at which the sulfur lattice has an interatomic distance of √3 times the substrate lattice constant, and it keeps a hexagonal symmetry, but its main symmetry directions are rotated thirty degrees with respect to those of the substrate [5]. In both cases, the adsorption site is one of the three equivalent threefold symmetry sites. Figure 3-2 shows a room-temperature STM image of both hexagonal reconstructions. A schematic representation of both geometries, with the sulfur atom positions relative to the Ru(0001) substrate, is shown in Figure 3-3. The peak-to-peak apparent corrugation of the (2x2) reconstruction is 0.33±0.03Å, and that of the (√3x√3)R30º reconstruction is 0.26±0.02Å when measured at 4K with a sample bias of 1V and a tunneling current of 500pA.

Geometrically, on a hexagonal substrate three inequivalent threefold-symmetry adsorption sites exist. These sites are the top (the adatom lays on top of a substrate atom), HCP (ABA stacking, the adatom occupies a site that would lead to a hexagonal close packed reconstruction) and FCC (ABC stacking, the adatom is placed in a site that forms the close packed plane of a face-centered cubic crystal) sites. The adsorption energy of an atom on a surface depends on the nature of both the substrate and the adsorbate. In the case of sulfur on Ru(0001), it has been experimentally proven that the preferred adsorption site is the HCP threefold symmetry site [6]. This is in disagreement with calculations in [7], that predict that the preferred site for sulfur adsorption on most transition metals after H_2S dissociation is the FCC. Nevertheless these calculations don't include ruthenium. Density functional theory (DFT) calculations for the adsorption of different atomic and molecular species on the basal plane of ruthenium confirm the higher stability of the HCP site for a sulfur coverage of θ=0.25 [8]. Figure 3-3 shows the schematic representations of the (2x2) and (√3×√3)*R*30° reconstructions with the sulfur atoms adsorbed on the HCP sites.

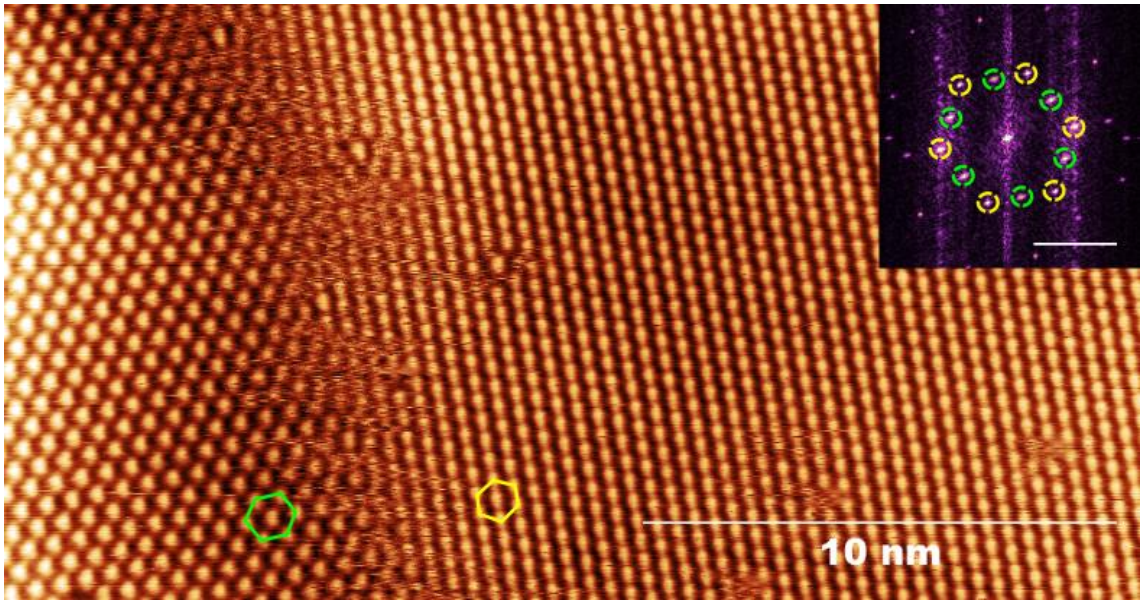

Figure 3-2 – 300K STM topographic image of an interface between the (2x2) (green) and (√3x√3)R30° (yellow) reconstructions, along with the FFT of the image (inset), at which the corresponding spots of each reconstruction have been marked in their respective colors.

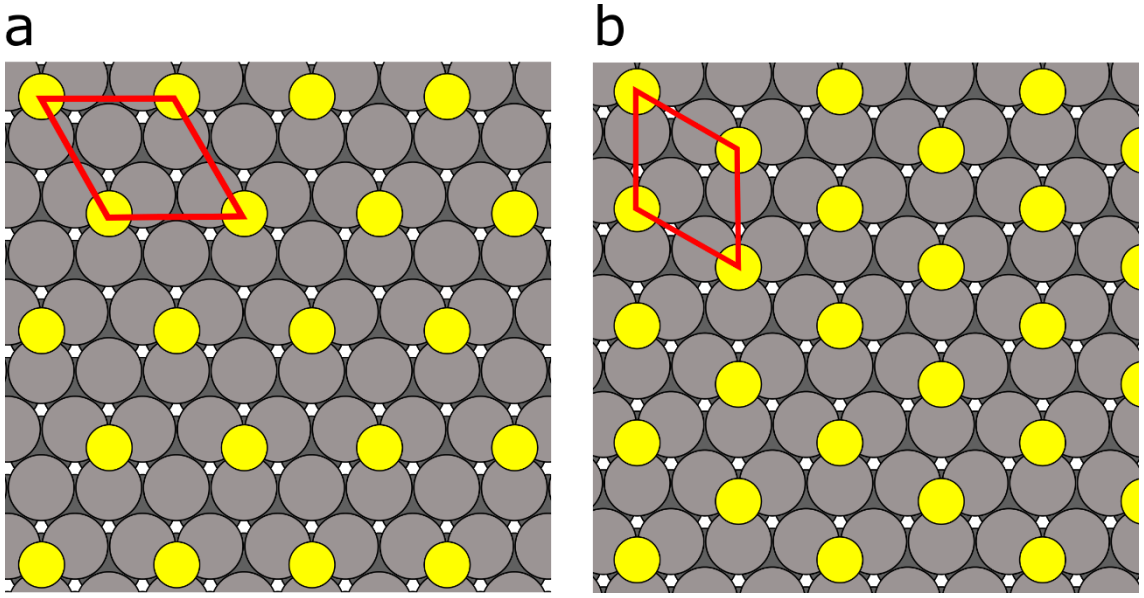

*Figure 3-3 –Hard-sphere models for the (2x2) (a) and (√3×√3)*R30° *(b) reconstructions, where the sulfur atoms (yellow) sit on the HCP adsorption sites. The first and second layers of the Ru(0001) substrate have been represented by light and dark gray circles, respectively. The sulfur unit cells for each reconstruction are represented by a red line.*

For low coverages ($0.1<\theta<0.22$), the sulfur is distributed on the surface forming small (2x2) islands. The island average size increases with coverage until the emergence of a (2x2) phase with disordered defects is formed at $\theta=0.22$ (Figure 3-4) [9]. This behavior is attributed in [2] to a repulsive interaction between the adsorbed sulfur atoms. A complete (2x2) ordered layer is obtained at $\theta=0.25$ [9].

For coverages below $\theta=0.25$ it is not possible to take good STM images at room temperature. The substrate steps are easily identified but there is no way to observe any kind of ordered structure. This is consistent with the phase diagram in [2], from which it is expected to find the adsorbed sulfur in a disordered phase at 300K. When lowering the temperature to 77K, the adsorbed layer is not disordered anymore and good STM images can be obtained. The appearance of the adlayer

is that of localized clusters of sulfur atoms (Figure 3-4) standing still in their preferential adsorption sites, that correspond to the HCP threefold-symmetry sites.

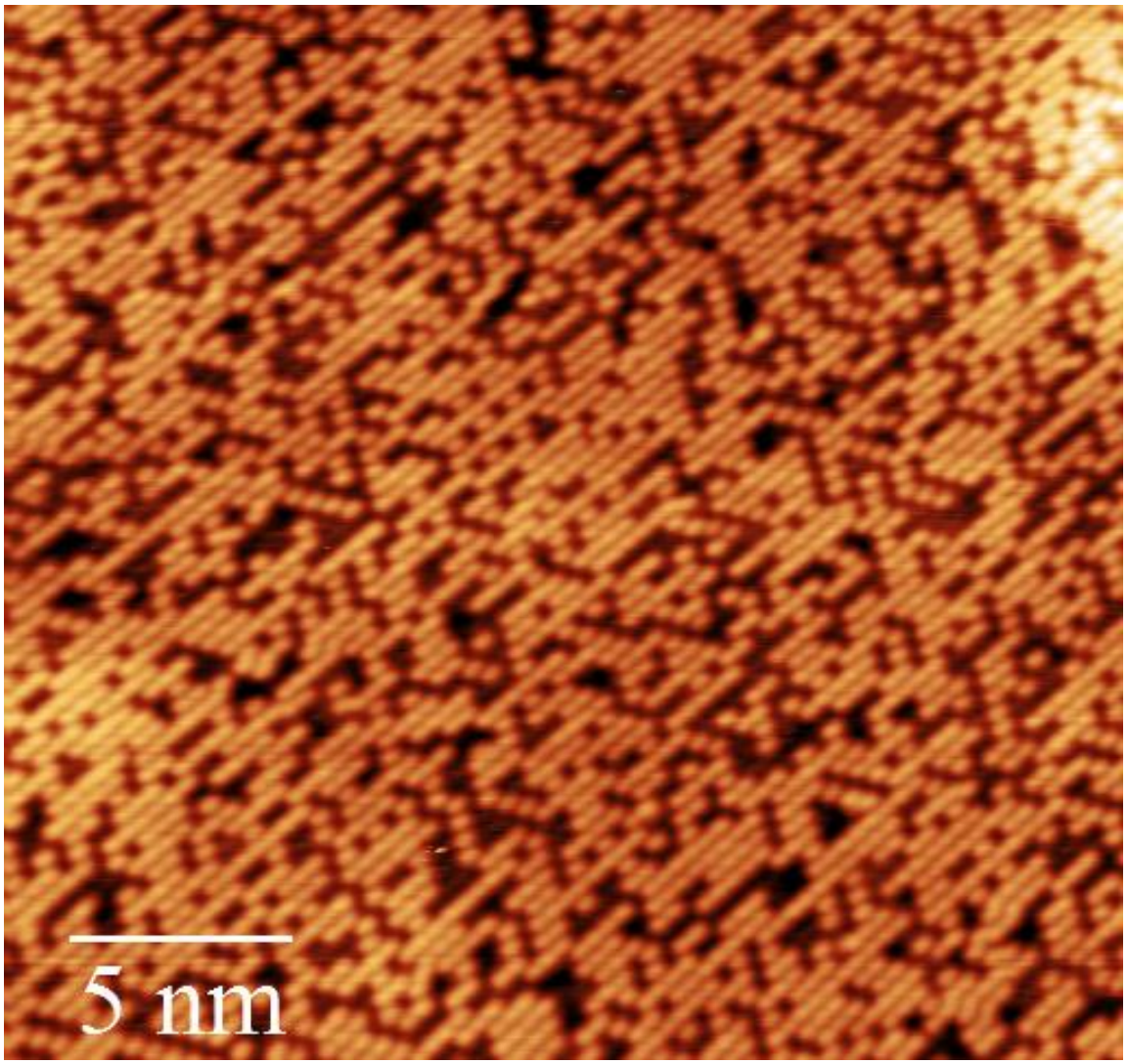

Figure 3-4 – STM topographic image of S/Ru(0001) at a coverage below that of a complete (2x2) layer (θ<0.25). The sulfur atoms form (2x2) clusters separated by sulfur-free regions. When measured at room-temperature, a S/Ru(0001) surface at the same coverage cannot be properly imaged due to the continuous movement of the sulfur atoms. T=77K, V_s=2V, I_t=50pA.

According to [8], the binding energy of the sulfur atoms at a coverage of θ=0.25 is -5.76eV for the atoms in the HCP adsorption sites, while it would be -5.65eV in the case of the FCC sites. The diffusion barrier in the HCP-bridge-FCC path is just 0,41eV, which explains the continuous wandering of the sulfur atoms at room temperature when we are in this coverage range.

Increasing the coverage above θ=0.25 leads to the formation of (√3×√3)R30° domains coexisting with the (2x2) phase. This domains grow in size with coverage until the roles are changed and we are left with (2x2) domains embedded in a (√3×√3)R30° background (Figure 3-5). A complete monolayer of the (√3×√3)R30° reconstruction is formed at θ=0.33. The preferred adsorption site is the HCP threefold-symmetry site, just as in the (2x2) reconstruction [6].

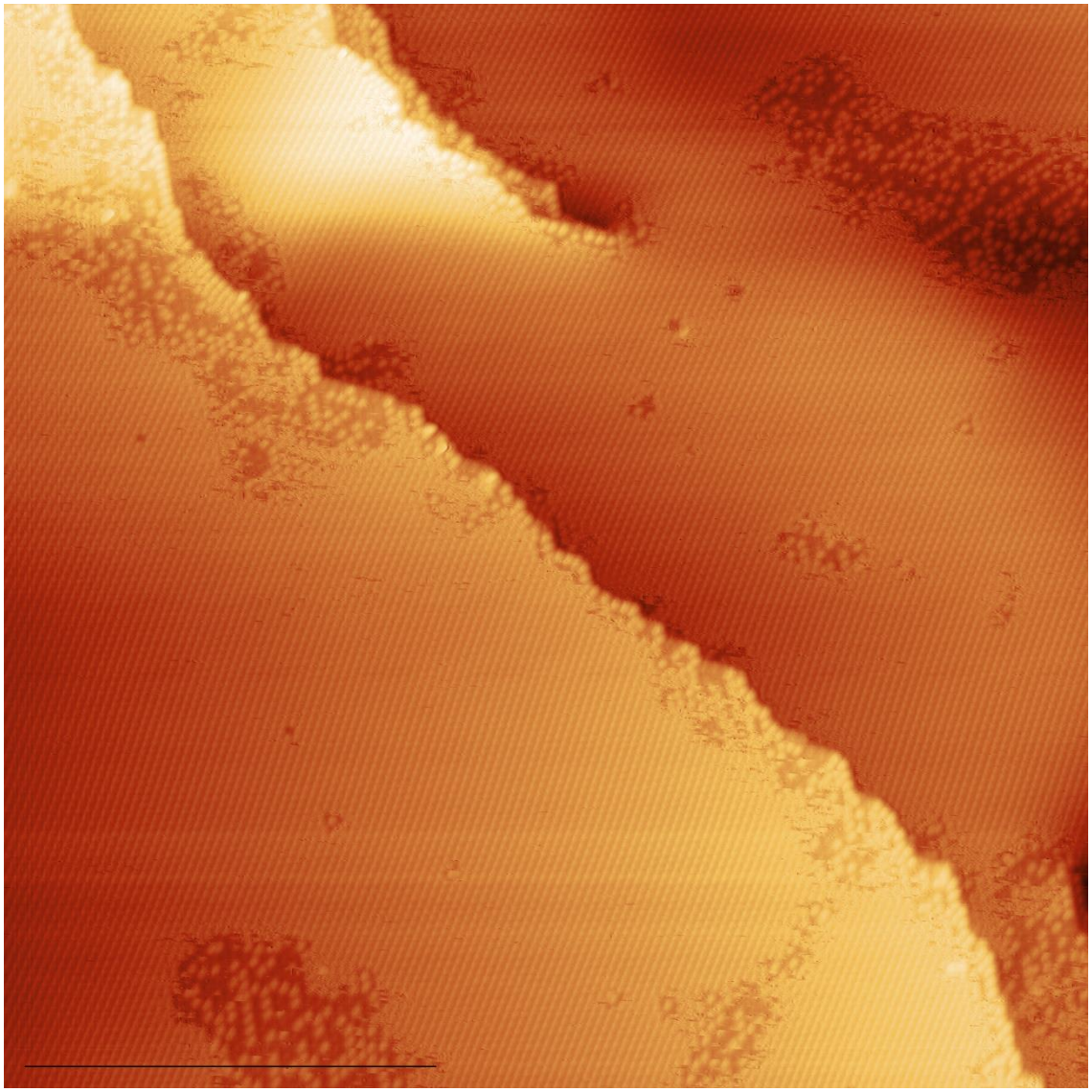

Figure 3-5 – STM topographic image of a S/Ru(0001) sample at a coverage slightly below θ=0.33. Most of the surface is covered by sulfur in the (√3x√3)R30° phase, but some (2x2) domains wander across. The step edges of the surface keep preferentially the (2x2) reconstruction. T=300K, V_s=-1V, I_t=30nA. Scale-bar: 20nm.

When approaching the nominal coverage at which the (√3x√3)R30º phase would completely cover the surface (θ=0.33), we observe that most of the sulfur atoms are distributed in that geometry with patches with lower density. This low density phase correspond to regions that keep the (2x2) geometry. At room temperature, the atoms inside this lower density regions are continuously moving and those close to domain interfaces swap positions between the (2x2) and the (√3x√3)R30º lattice in a dynamic equilibrium. Figure 3-6 shows a series of room temperature STM images taken at the same area at almost 0.2frames/s (1 frame every 4.8s) showing the evolution of the surface at this coverage range.

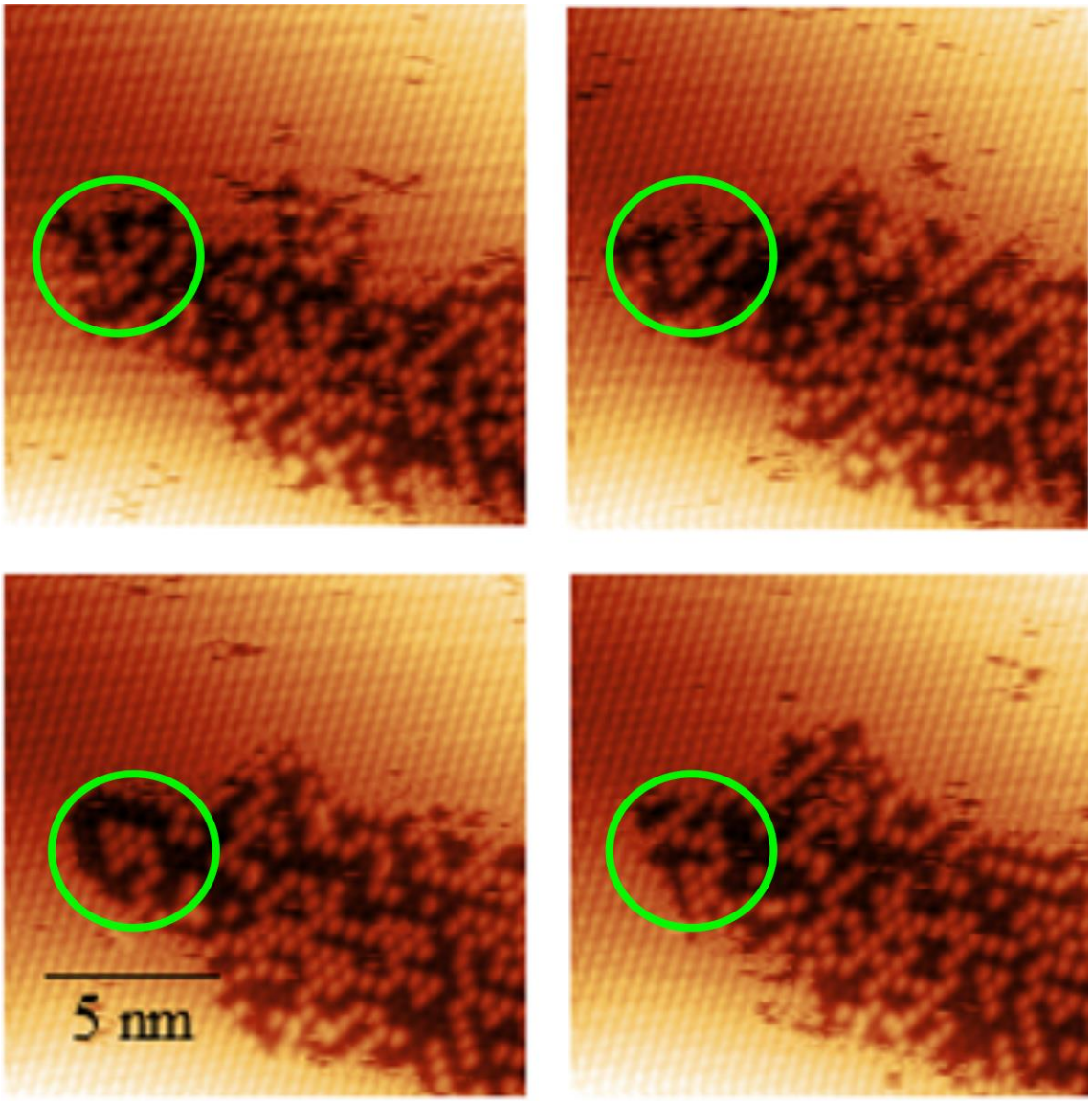

Figure 3-6 – STM topographic images showing the evolution of the (2x2) domains in a (√3x√3)R30º background. The figure shows four consecutive frames of a series of 100. Each frame took 4.8 seconds to complete. The green circle marks a region at which the evolution between the different images can be easily traced. T=300K, V_s=-1V, I_t=30nA.

When cooling to liquid nitrogen temperature, the movement of the less dense regions through the sample and of the atoms within them is inhibited, as shown in Figure 3-7. It is worth noting the appearance of dislocations among the (√3x√3)R30º region, separating different antiphase domains (Figure 3-7). Increasing coverage above θ=0.33 will result in the appearance of self-interstitial atoms in these dislocations, leading to the formation of the domain-wall phase described in the next section.

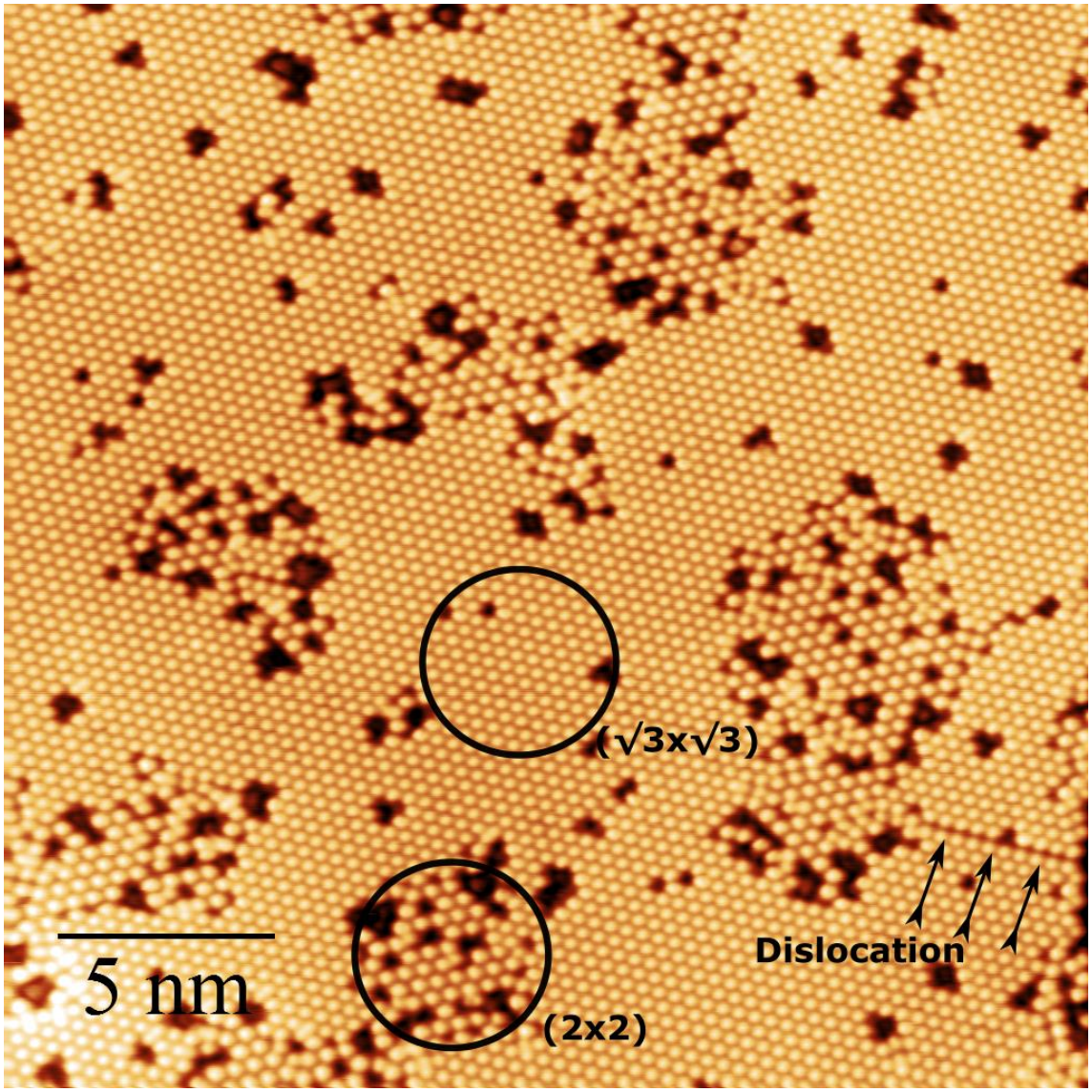

Figure 3-7 – STM topographic image showing the coexistence of the (2x2) and (√3x√3)R30° reconstructions and the formation of dislocations in the (√3x√3)R30° regions. T=77K, V_s=1V, I_t=200pA.

3.3 DOMAIN-WALL PHASE OF S/RU(0001)

Above θ=0.33, disordered linear dislocations start forming in the surface. Above θ=0.35 splitting of the √3 LEED diffraction spots indicates the formation of an ordered domain-wall (DW) phase [2]. This DW phase presents a twofold symmetry that breaks the hexagonal symmetry of the substrate. Three different rotational domains are present. The domain walls are formed by the addition of sulfur atoms as self-interstitials in the previously formed linear dislocations. The newly deposited atoms fit between two different translational domains of the (√3x√3)R30º phases, adsorbed in this case in FCC threefold symmetry sites [10]. The apparent corrugation of the domain walls along their main symmetry direction is 0.21±0.02Å measured through the HCP-adsorbed atoms and 0.17±0.02Å along the FCC chains, when measured with the LT-STM at LHe temperature with a sample voltage of 1V and a tunneling current of 500pA.

The DW regime covers from θ=0.33 to θ=0.42, with the density of domain walls increasing with coverage. When DW concentration is small, they wander through the sample at room temperature, making it impossible to image them with the STM. Lowering the temperature to 77K freezes the movement of the DWs and we can see their structure. At these temperature, the DWs can be seen

in two different configurations, depending on the step of their movement they are; Figure 3-8 shows a STM topographic image of a low-density DW surface, along with a schematic representation of the two configurations of the DWs.

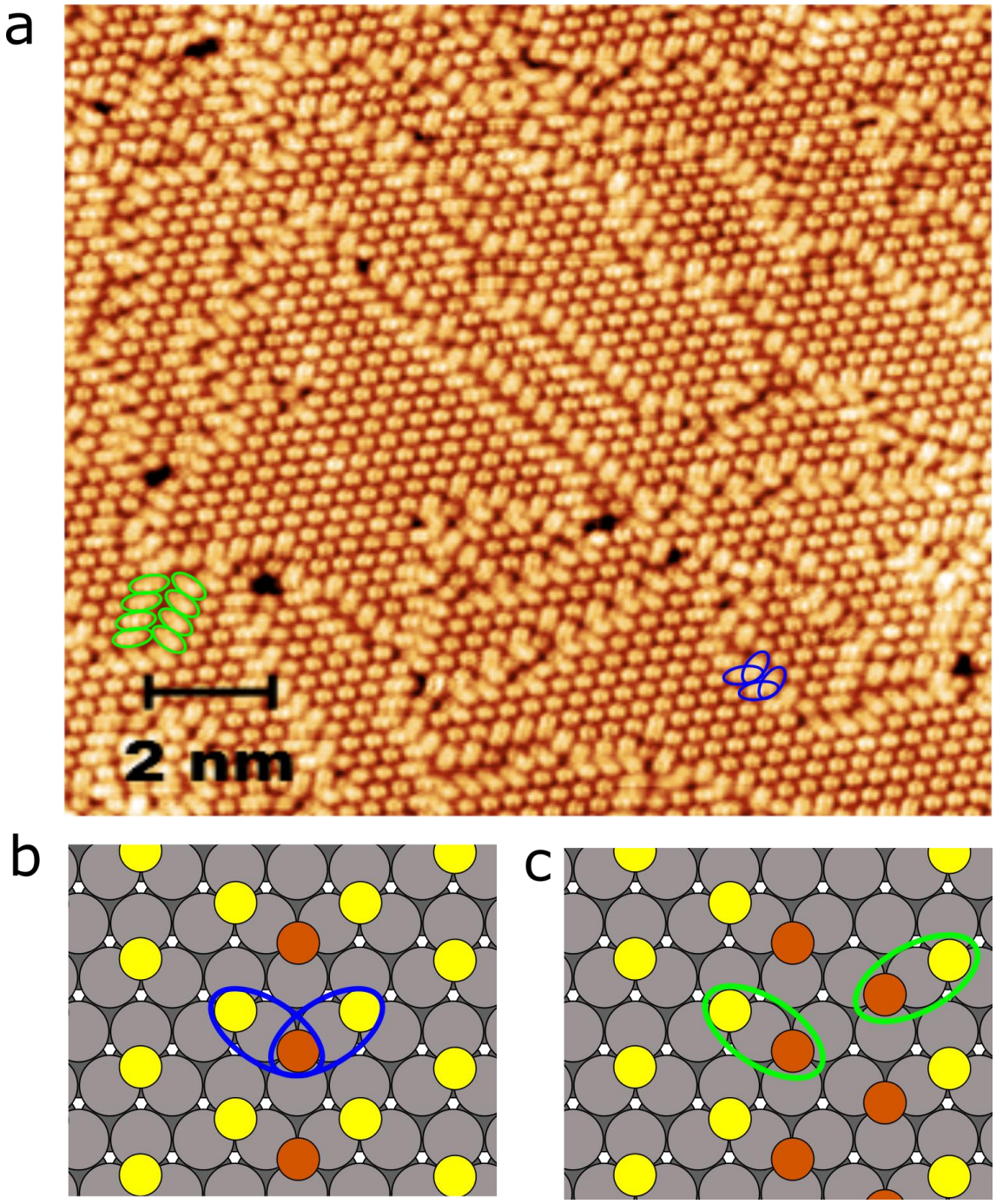

Figure 3-8 – (a) STM topographic image (T=77K, V_s=2V, I_t=100pA) of a S/Ru(0001) sample in the DW phase with a low density of DWs. The DWs can be seen in two different configurations: a dense one at which there is a line of self-interstitial FCC sulfur atoms ((b), marked in blue in (a)), and a less dense one, at which there are two consecutive lines of FCC sulfur atoms separated by a distance of √3 ((c), marked in green in (a)). Yellow circles represent the sulfur atoms in the (√3x√3)R30 domains, and brown circles are the sulfur atoms of the DWs in the FCC adsorption sites.

In [11], a description of the diffraction pattern of domain walls of the Xe/Pt(111) (√3x√3)R30º-incommensurate transition leads to a classification of the DWs between hexagonal domains of the same phase depending on the density of the walls and the interaction between them.

When starting from a hexagonal phase, as is our case for the (√3x√3)R30º reconstruction, domain walls can be described as superlight and light when the target phase is less dense than the original one, and heavy and superheavy when the resulting phase would be denser than the original one [11]. Also, the walls can be arranged in a honeycomb pattern or in striped arrays, depending if their crossing is favored or not. In the case of the S/Ru(0001) (√3x√3)R30º-c(2x4)-2S transition the system is evolving to a denser phase, so the domain walls should be of the heavy or superheavy type.

According to this classification and considering the experimental LEED [2] and STM [3] evidences, the structure of the surface reconstruction of sulfur on the (0001) plane of ruthenium at this coverage range corresponds to a striped array of super-heavy domain walls, what means that the domain-wall crossings are energetically unfavorable.

For this type of domain walls, the possible inter-wall distance l is determined by the number of unit cells, n, of the (√3×√3)R30° domains they are separating by $l = \left(\frac{3}{2}n - 1\right)a; n = 2,3,4\ldots$, being a the substrate lattice constant. This expression is related to coverage θ by $l = \frac{a}{3\theta - 1}$ [3]. At θ=0.42 (n=2), the inter-wall density reaches its minimum. Figure 3-9 shows a hard-sphere representation of a domain-wall phase for n=4 and Figure 3-11 for n=2.

These superheavy domain walls can be depicted as long dislocations with a line of self-interstitial defects. The atoms forming the wall will occupy the most favorable unoccupied site, which in this case is close to the FCC threefold symmetry site [10]. The (√3x√3)R30º domains at each side of one of these walls correspond to two of the three different translational domains that can form for the given geometry, as shown in Figure 3-9.

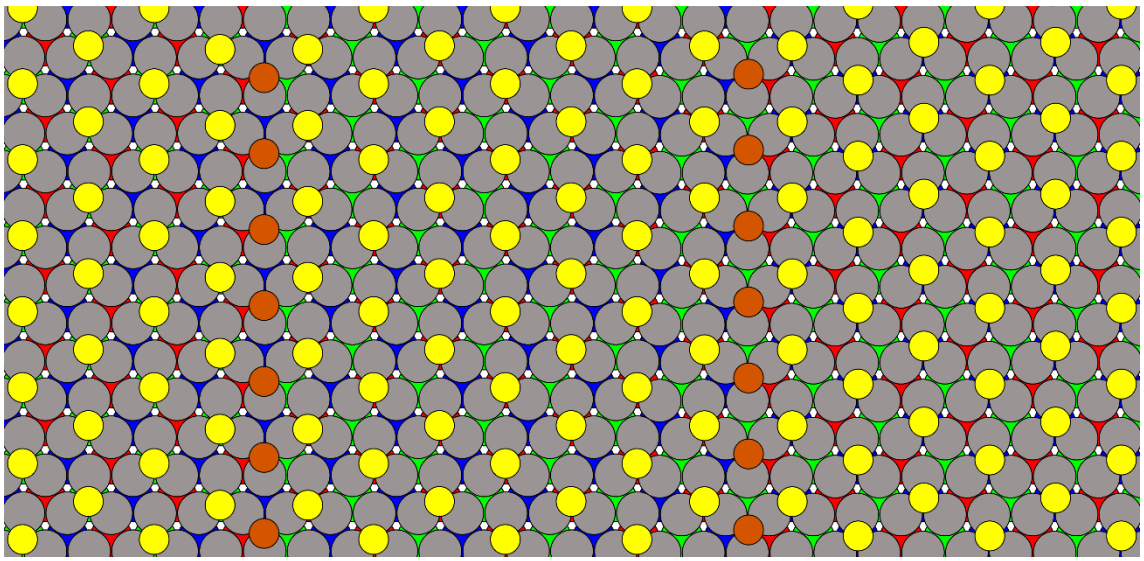

*Figure 3-9 – Hard-sphere representation of two superheavy DWs separating three (√3×√3)*R30° *domains. The red, green, and blue circles in the second substrate layer represent the three inequivalent HCP adsorption sites of the translational phases in a(√3×√3)*R30° *reconstruction . Yellow circles represent the sulfur atoms of the (√3x√3)R30º domains, placed on HCP sites, while the brown ones are the sulfur atoms of the DW, sitting on FCC sites.*

The maximum density of super-heavy domain walls is reached at a coverage of θ=0.42. At this regime the separation between walls is minimum (1.5a) and it can be considered a long-range commensurate (7x√3)-3S reconstruction (Figure 3-11). As happened with the low coverage hexagonal phases, this superheavy domain-wall phase also undergoes a continuous order-disorder phase transition when approaching the critical temperature [12]. Since at this coverage we can consider the sulfur layer as a compact array of DWs or as a new commensurate phase with a (7x√3)-3S unit cell, we will define them as dense domain walls (DDWs), in order to differentiate

them from the less dense regime. Figure 3-10 shows a STM image of the DDWs, and a schematic representation of its geometry is shown in Figure 3-11.

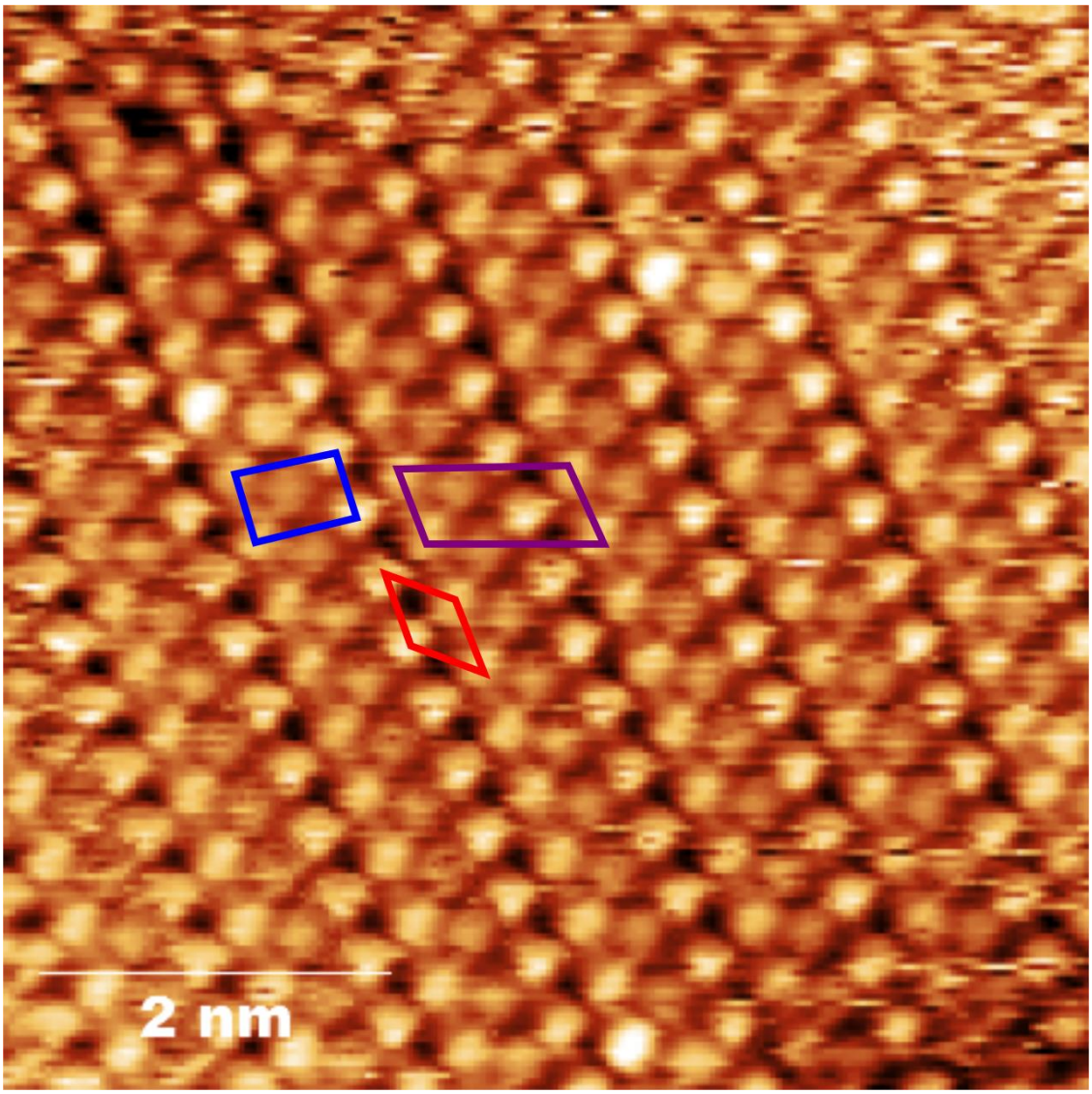

Figure 3-10 – STM topographic image taken at 300K of DDWs in S/Ru(0001) at a coverage of 0.42ML. The unit cells of the c(2x4) (blue line), (√3×√3)R30° (red line) and the DDW (purple line) lattices have been superimposed in order to compare with the schematic at Figure 3-11. V_s=50mV, I_t=17nA.

LEED diffraction experiments [11] can serve as a quick method to know if the sample has reached the domain-wall regime. A series of satellite spots forming an equilateral triangle appear centered around the point where the √3 spot used to be and their separation grows with increasing coverage. The intermixing of these three domains gives rise to the triangular spot arrangement around the point at which the √3 spot of the diffraction pattern should be (Figure 3-13). LEED experiments always show a combination of the three rotational domains, since the spot is bigger than each of the individual domains. FFT of single DDW domains (Figure 3-12) allow us to obtain the phase-space pattern of an individual domain, and makes it easier to understand the macroscopic diffraction pattern as the contribution of three rotational domains.

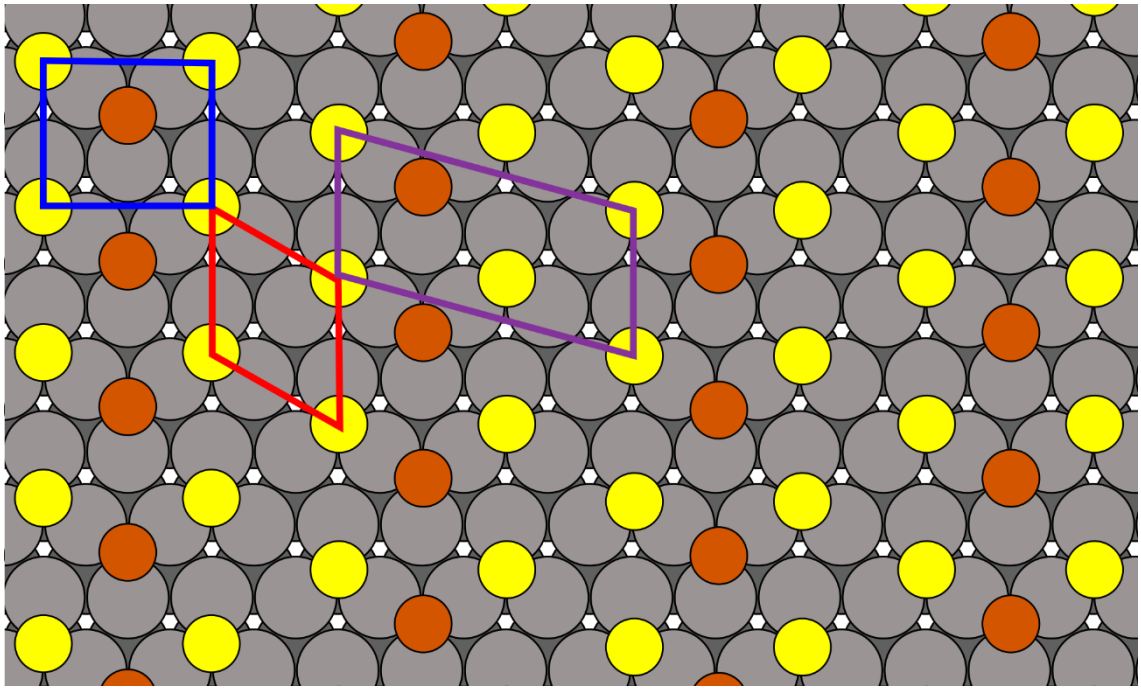

Figure 3-11 – Hard-sphere representation of the DDW phase in S/Ru(0001). The unit cells of the c(2x4) (blue line), (√3×√3)R30° (red line) and the DDW phase (purple line) lattices are superimposed. The sulfur atoms in HCP sites are represented in yellow, those in FCC sites in brown.

Domain walls are regions of the adsorbed layer at which the atoms are closer to each other than in the commensurate phase [13]. They can be considered as structural solitons that separate domains of the commensurate lattice [14] and introduce a phase shift between domains [15]. This phase shift can have different physical meanings, from a purely geometrical one, to spin orientation in magnetic layers [16].

The interaction of the atoms with the substrate will force them to stay in specific places related to the periodicity of the substrate and leading to a commensurate structure, but the interaction of each adsorbate with its neighbors will push the system to an incommensurate structure. It is the interplay between this two interactions that leads to the formation of domain wall phases at certain temperatures or chemical potentials [17].

The first theoretical approach to domain-wall formation in adsorbed monolayers was carried on by Frank and Van der Merwe considering one-dimensional dislocations in single crystal overlayers. They developed a simple model at which the substrate is considered a periodic potential and the interaction between adatoms is modelled by spring forces [18] [19]. This theory takes good account of the misfit of the lattices with one-dimensional incommesurabilities, but cannot be extended to two-dimensional systems with more than one equivalent directions.

The theory developed by Pokrovskii and Talanov tries to overcome this problem considering the two-dimensional problem. It predicts a continuous phase transition between the commensurate and incommensurate phases involving the formation of parallel domain walls that break the symmetry of the substrate. The domain walls would keep the structure of the substrate in one of its main symmetry directions but have different lattice vectors in the rest. At low temperatures this walls would cross the sample in perfect parallel lines and a finite temperature would favor the bending of the walls, but wall crossings are not expected to be energetically stable and are not considered [14].

The experimental evidence of the formation of domain wall systems with honeycomb symmetry [20] [21] [22] lead to Bak, Mukamel, Villain and Wentowska to consider the possibility of

domain-wall crossings in the commensurate-incommensurate transitions of two-dimensional systems. Their theory considers the formation of wall crossings in the case of attracting domain walls and predicts the formation of honeycomb lattices of domain walls undergoing first-order transitions [23]. Also, the presence of defects and impurities that alter the homogeneous potential of the substrate can lead to the formation of domain-wall crossings [24].

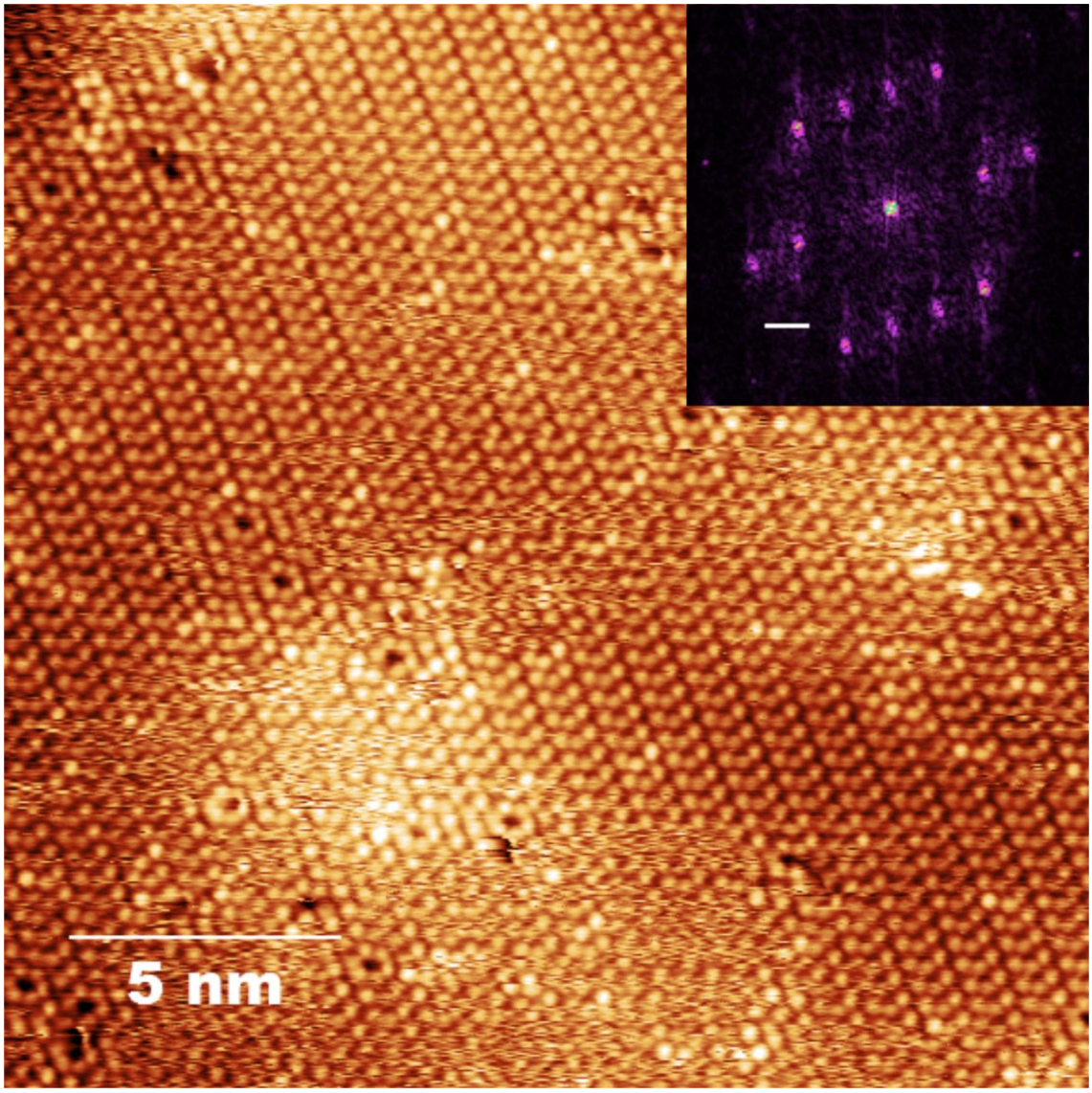

Figure 3-12 - STM topography image of the DDW phase (θ=0.42) of S/Ru(0001)presenting one of the rotational domains and some point defects. The inset is the FFT of the main figure, showing the characteristic phase-space arrangement of spots of a single domain of DDW. T=300K, V_s=0.1V, I_t=17nA.

Although the DDW phase, at θ=0.42, had already been described, the possibility of imaging the intermediate coverage (0.33<θ<0.42) regions at low temperature gives us an insight on the evolution of the system in the commensurate-incommensurate transition. Similar studies were carried on recently in [25] for a chemisorbed layer of chlorine on Ag(111). The evolution of Cl/Ag(111) has some similarities with S/Ru(0001), such as the formation of superheavy domain walls over θ=0.37, but there are also some differences in their evolution. Before the domain-walls start forming, star-like compression defects form in the chlorine layer. At coverage of 0.37, these defects merge into domain walls and their mutual interaction is repulsive. Increasing coverage leads to the reduction of the interwall distance and the increase in the wall length along with the formation of (3x3) islands. When coverage reaches 0.40, the commensurate (3x3) phase is completed and the domain walls are no longer present.

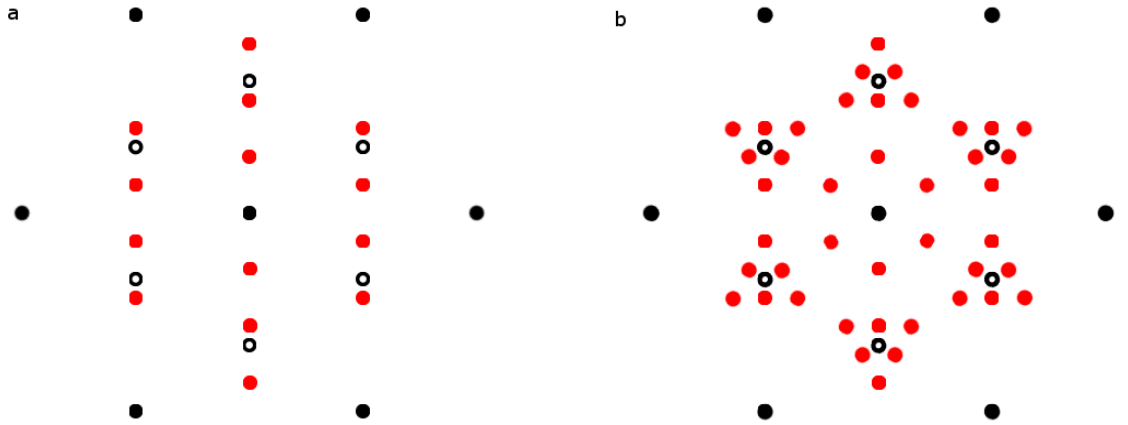

Figure 3-13 – Schematic diffraction pattern of the domain-wall phase of the S/Ru(0001). Black circles represent the first order diffraction spots of the substrate, empty circles indicate the place where the √3 would be and red circles are the diffraction spots of the domain walls. (a) Corresponds to the diffraction of a single domain and (b) shows the three rotational domains. The relative distances in this figure correspond to a coverage of θ=0.42.

When comparing the S/Ru(0001) and the Cl/Ag(111) systems, we can find some coincidences in the behavior of the domain-wall phase in the $0.37<\theta<0.40$ coverage range, when the domain walls are already formed. They grow in length and become closer to each other, leading to the shrinking of the domain size of the low-density commensurate phase. Nevertheless, in the $0.33<\theta<0.37$ region neither us nor the reported papers on S/Ru(0001) find any evidence on the formation of individual compression defects. In our case it seems that the mechanism for the formation of the domain walls involves the appearance of dislocations that already separate antiphase domains and look like the superheavy domain walls without the line of self-interstitials, being locally less dense than the (√3x√3)R30º reconstruction. As we have seen in the previous section, the coexistence of the (2x2) and (√3x√3)R30º reconstructions results in a system at which the different domains are continuously moving through the surface. This mobility can lead to the formation of this dislocations when two antiphase (√3x√3)R30º domains merge after crossing a (2x2) region. Further increase of the coverage will lead to the filling of the FCC sites among the dislocations with self-interstitial sulfur atoms. Also, the endpoint of the domain-wall phase in Cl/Ag(111) is reached at $\theta=0.40$, when the denser commensurate (3x3) phase is developed. In the case of S/Ru(0001), this evolution keeps going up to $\theta=0.50$, since there is no commensurate phase until the formation of the rectangular c(2x4)-2S reconstruction.

Past $\theta=0.42$, we cannot consider anymore that we are in the superheavy domain-wall phase, since two consecutive domain walls form the c(2x4) lattice.

3.4 C(2X4) RECONSTRUCTION OF S/RU(0001)

Increasing the coverage above $\theta=0.42$ leads to the merging of the domain walls into c(2x4) domains. The complete layer of this reconstruction is not reached until $\theta=0.5$. Below this coverage, in the $0.43<\theta<0.48$ range, domains of the DDW and c(2x4) phases cover the surface.

The c(2x4) phase presents a twofold symmetry, so there are three possible rotational domains on top of the hexagonal substrate. The sulfur atoms are arranged in centered rectangles, with the atoms of the vertex placed close to the HCP sites and the centered atoms sitting close to the FCC sites (or vice-versa). There is a small displacement of around 0.16Å in opposite directions with respect to the exact position of the threefold symmetry sites due to relaxation processes [26]. The

apparent corrugation of this reconstruction is 0.17±0.03Å measured by STM at LHe with a sample voltage of 1V and a tunneling current of 500pA.

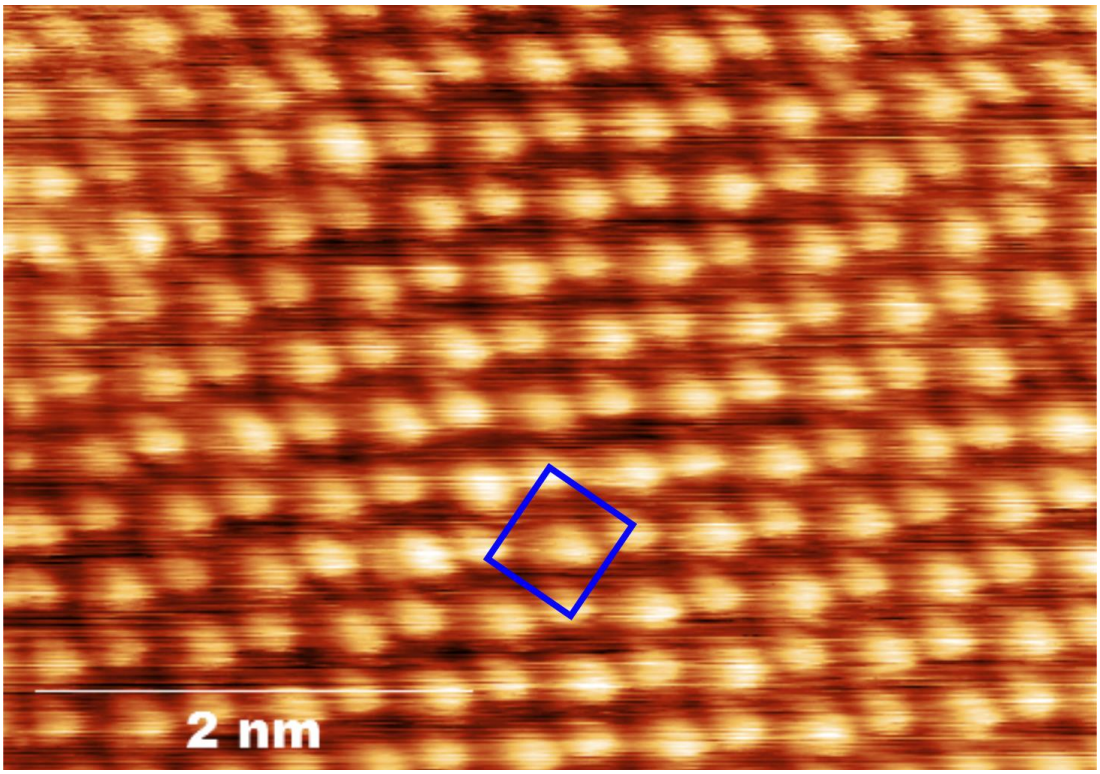

Figure 3-14 – STM topographic image of a c(2x4)-2S region of S/Ru(0001). The unit cell has been superimposed as a blue rectangle.T=300K, V_s=5mV, I_t=1nA.

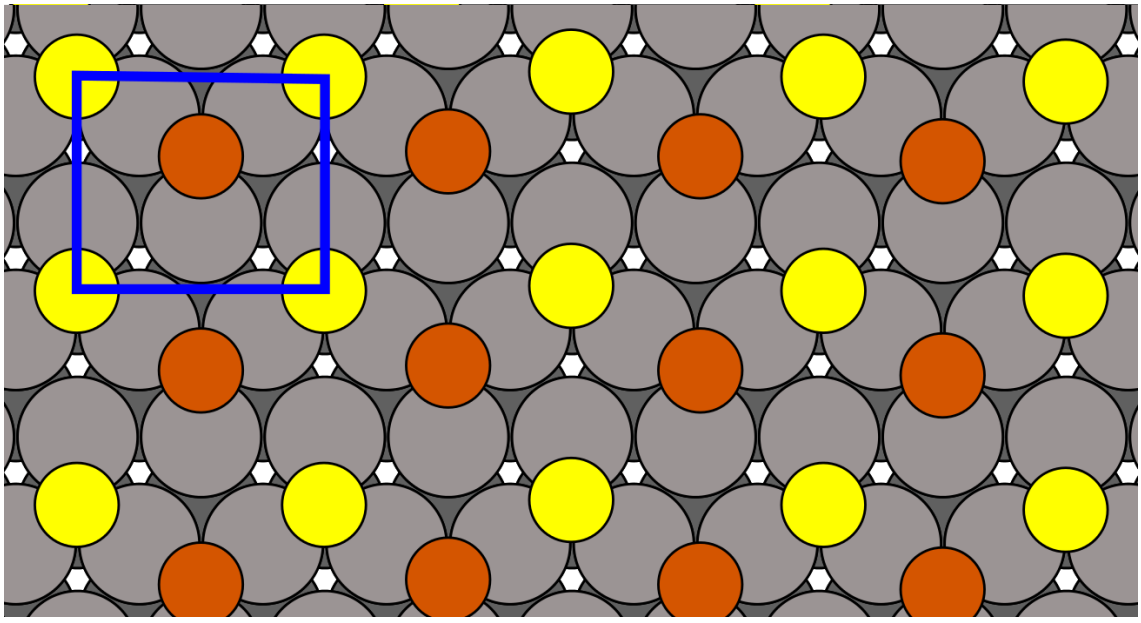

Figure 3-15 – Hard-sphere model of the c(2x4)-2S reconstruction. Substrate atoms are represented by the gray circles and sulfur atoms by yellow circles when in HCP sites and brown circles when in FFC sites. The blue rectangle shows the unit cell of the reconstructed surface.

The adsorption of sulfur in this geometry results in a significant bucking of the first Ru(0001) layer, which is highly attenuated in the second substrate layer [26]. The c(2x4) reconstruction also presents a first order phase transition to the disordered phase with a critical temperature of 745±0.5K [12].

The c(2x4)-2S phase still presents mobility of its atoms at RT. This can be extracted from the fact that the boundaries between rotational domains still move in the time scale of seconds [3].

Past the c(2x4)-2S phase, over the θ=0.5 limit, a (√7x√7)R19.1º reconstruction with four sulfur atoms per unit cell starts forming [27], followed by a series of long-range commensurate and incommensurate phases until a second sulfur layer starts building up at θ=0.62 [2]. For the sake of brevity and since our results regarding the intercalation of sulfur underneath graphene is limited to coverages up to θ=0.5, we will not enter in details on such high density phases. Figure 3-16 summarizes the exposure times and pressures used in this work in order to get the different reconstructions. In all cases, the exposure was performed at room temperature.

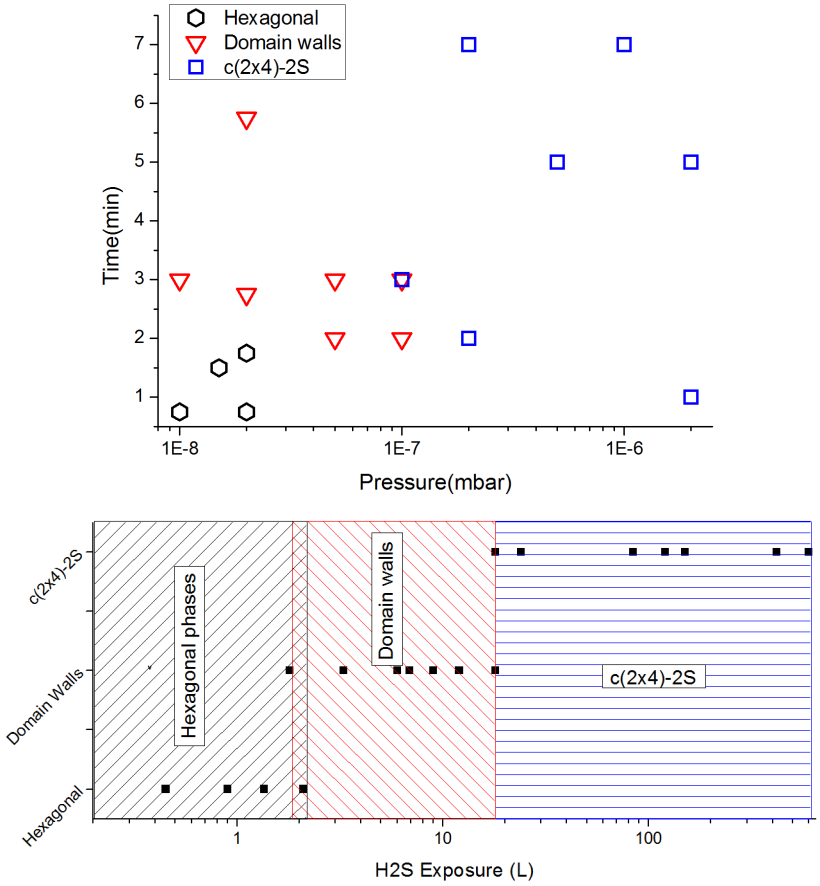

Figure 3-16 – Distribution of the different reconstructions of sulfur on ruthenium(0001) as a funcion of time and pressure (upper graph). Black hexagons represent the hexagonal phases, (2x2) and (√3x√3)R30º, both in their pure phases and mixed; red triangles represent the domain wall phase (coverages up to 0.42); and blue squares the c(2x4)-2S reconstruction. The lower graph translates these results into langmuirs (1L=10^{-6}torr·1s), with each colored area representing one of the phases. The black squares are the experimental data from the upper graph.

3.5 CONCLUSIONS

- A geometric characterization of the S/Ru(0001) surface was performed, taking in account the previous developments achieved for this system.

- S/Ru(0001) presents a complex phase diagram which comprises hexagonal reconstructions in the low coverage regime, but ends up breaking the substrate symmetry for the DW and c(2x4)-2S reconstructions.

- The interaction of sulfur with the basal plane of ruthenium is very strong and develops very localized bonds, adsorbing preferentially on the HCP threefold symmetry sites; the S-S interaction

is also intense. Competition of both interactions leads to the spontaneous appearance of domain-wall and high order commensurate phases.

- For all the coverage range under study, the different phases present a high mobility at RT for the adsorbed atoms, which decreases with increasing density. Only the DDW and c(2x4)-2S can be easily measured with STM at RT, in order to image the hexagonal and DW reconstructions lowering the temperature is required.

- The complex phase diagram of S/Ru(0001) makes sulfur a particularly interesting species to intercalate between graphene and ruthenium. In the low coverage regime it presents two hexagonal phases that preserve the symmetry of both graphene and Ru(0001), but at higher coverages it develops an incommensurate DW phase and a higher density commensurate, the c(2x4) reconstruction, that break the symmetry of both graphene and ruthenium. This different geometries can affect the properties of a graphene layer on top, since they drastically change its topological and electronic environment.

3.6 REFERENCES

[1] S. R. Kelemen and T. E. Fischer, "Interaction of H2S with the Ru(001) surface," *Surface Science,* vol. 87, no. 1, pp. 53-68, 1979.

[2] R. Dennert, M. Sokolowski and H. Pfnür, "Ordered phases and phase diagram of sulphur adsorbed on Ru(001)," *Surface Science,* vol. 271, no. 1-2, pp. 1-20, 1992.

[3] T. Müller, D. Heuer, H. Pfnür and U. Köhler, "Domain walls and adsorbate-step interactions: an STM study of sulphur layers on Ru(0001)," *Surface Science,* vol. 347, pp. 80-96, 1996.

[4] F. Calleja, Influencia de la estructura electrónica local en las propiedades de las superficies y su estudio mediante microscopía de efecto túnel, Madrid: PhD. Thesis, Universidad Autónoma de Madrid, 2007.

[5] D. Jürgens, G. Held and H. Pfnür, "Adsorbate induced relaxations of S/Ru(0001): p(2x2) and p(√3x√3)R30º structures," *Surface Science,* vol. 303, pp. 77-88, 1994.

[6] D. Heuer, T. Müller, H. Pfnür and U. Köhler, "Determination of the adsorption site of sulphur on Ru(0001) by STM," *Surface Science Letters,* vol. 297, pp. L61-L67, 1993.

[7] D. Alfonso, "First-principles studies of H_2S adsorption and dissociation on metal surfaces," *Surface Science,* vol. 602, pp. 2758-2768, 2008.

[8] J. Herron, S. Tonelli and M. Mavrikakis, "Atomic and molecular adsorption on Ru(0001)," *Surface Science,* vol. 614, pp. 64-74, 2013.

[9] M. Sokolowski and H. Pfnür, "Continuous order-disorder phase transitions of the p(2x2) and (√3x√3)R30º superstructures of sulfur on Ru(001): Effective critical exponents and finite size effects," *Physical Review B,* vol. 49, no. 11, pp. 7716-7728, 1994.

[10] D. Jürgens, C. Schwennicke and H. Pfnür, "Surface structure analysis of the domain-wall phase of S/Ru(0001) using an efficient parameter optimization method," *Surface Science,* vol. 381, pp. 174-189, 1997.

[11] P. Zeppenfeld, K. Kern, R. David and G. Comsa, "Diffraction from domain-wall systems," *Physical Review B,* vol. 38, no. 6, pp. 3918-3924, 1988.

[12] M. Sokolowski and H. Pfnür, "Phase transitions of the striped domain-wall phases of S on Ru(0001)," *Physical Review B,* vol. 51, no. 22, pp. 742-751, 1995.

[13] M. Gordon and F. Lançon, "The commensurate-incommensurate transition of Kr monolayers on graphite: II. Wall and wall crossing energies," *Journal of Physics C: Solid State Physics,* vol. 18, pp. 3929-3942, 1985.

[14] V. Pokrovskii and A. Talanov, "The theory of two-dimensional incommensurate crystals," *Zhurnal Eksperimental'noi i Teoreticheskoi Fiziki,* vol. 78, pp. 269-295, 1980.

[15] P. Bak, "Commensurate phases, incommensurate phases and the devil's staircase," *Reports on Progress in Physics,* vol. 45, pp. 587-629, 1982.

[16] J. Villain and P. Bak, "Two-dimensional ising model with competing interactions: floating phase, walls and dislocations," *Journal de Physique,* vol. 42, no. 5, pp. 657-668, 1981.

[17] J. Gottlieb and L. Bruch, "Uniaxial incommensurate rare-gas-monolayer solids. I. Structure and statistical mechanics," *Physical Review B,* vol. 44, no. 11, pp. 5750-5758, 1991.

[18] F. Frank and J. van der Merwe, "One-dimensional dislocations. II. Misfitting monolayers and oriented overgrow," *Proceedings of the Royal Society of London. Series A, Mathematical and Physical Sciences,* vol. 198, no. 1053, pp. 216-225, 1949.

[19] F. Frank and J. van der Merwe, "One-dimensional dislocations. III. Influence of the second harmonic term in the potential representation, on the properties of the model," *Proceedings of the Royal Society of London. Series A, Mathematical and Physical Sciences,* vol. 200, no. 1060, pp. 125-134, 1949.

[20] D. Moncton, J. Axe and F. DiSalvo, "Study of superlattice formation in 2H-$NbSe_2$ and 2H-$TaSe_2$ by neutron scattering," *Physical Review Letters,* vol. 34, no. 12, pp. 734-737, 1975.

[21] M. Chinn and S. Fain, "Structural phase transition in epitaxial solid krypton monolayers on graphite," *Physical Review Letters,* vol. 39, no. 3, pp. 146-149, 1977.

[22] M. Nielsen, J. McTague and W. Ellenson, "Adsorbed layers of D_2, H_2, O_2, and 3He on graphite studied by neutron scattering," *Journal de Physique Colloquies,* vol. 38, pp. C4-10-C4-18, 1977.

[23] P. Bak, D. Mukamel, J. Villain and K. Wentowska, "Commensurate-incommensurate transitions in rare-gas monolayers adsorbed on graphite and in layered charge-density-wave systems," *Physical Review B,* vol. 19, no. 3, pp. 1610-1613, 1979.

[24] J. Villain, "Effect of substrate defects on commmensurate-incommensurate transitions of adsorbed layers," *Journal de Physique Lettres,* vol. 41, pp. 267-270, 1980.

[25] B. Andryushechkin, V. Cherkez, B. Kierren, Y. Fagot-Revurat, D. Malterre and K. Eltsov, "Commensurate-incommensurate phase transition in chlorine monolayer chemisorbed on Ag(111): Direct observation of crowdion condensation into a domain-wall fluid," *Physical Review B,* vol. 84, p. 205422, 2011.

[26] C. Schwennicke, D. Jürgens, G. Held and H. Pfnür, "The structure of dense sulfur layers on Ru(0001). I. The c(2x4) structure," *Surface Science,* vol. 316, pp. 81-91, 1994.

[27] W. Sklarek, C. Schwennicke, D. Jürgens and H. Pfnür, "The structure of dense sulfur layers on Ru(0001). II. The (√7x√7)R19.1° structure," *Surface Science,* no. 330, pp. 11-19, 1995.

4 INTERCALATION OF SULFUR IN GRAPHENE/RU(0001)

In this chapter we explain the methods involved in the intercalation of sulfur underneath graphene grown on Ru(0001). In the first section we will introduce the preparation and properties of graphene/Ru(0001) and a revision of the intercalated graphene systems, taking special attention on those involving ruthenium as substrate. The last sections deal with the preparation and characterization of S/graphene/Ru(0001) in the different intercalation regimes.

4.1 INTRODUCTION

4.1.1 Graphene/Ru(0001)

Graphene has been deeply studied in the last years, both experimentally and theoretically, due to its interesting electronic properties and as a playground for a completely new field of science: that of the two-dimensional materials.

Graphene consists in a two-dimensional lattice of sp^2 hybridized carbon atoms arranged in honeycomb geometry [1]. A completely isolated sheet of graphene, that is, in vacuum and free of substrate interactions, is predicted to present a linear dispersion relation around the Fermi level [1] [2]. Its electronic bands intersecting at the Fermi level in the Dirac point, giving rise to a conical band structure around the K point. Furthermore, the honeycomb lattice consists in two inequivalent triangular lattices that break the symmetry between electrons and holes and a pseudospin that makes the carriers in graphene chiral [1].

The ideal graphene system is a theoretical model that is not easy to reproduce in laboratory conditions. The main reason is that it is not possible to have a completely isolated graphene layer. Although we can reach extremely low pressures in ultra-high vacuum chambers, graphene will always be placed in a substrate that will interact with it, doping it and modifying its ideal band structure.

Nevertheless, this is far from inconvenient: the interaction of graphene with different substrates gives rise to interesting behaviors. We can use the substrate influence on the graphene properties in our benefit, using these interactions to tailor its physical properties. A forbidden energy band gap can be open through the interaction of graphene with its substrate, turning it into a semiconductor material [3] [4]. The specific substrates or adsorbed molecules can also n- or p-dope graphene, shifting its band structure in order to tailor its properties for future devices and applications [5] [6] [7].

There are different techniques for growing graphene, many of them relying in CVD methods. Among these techniques, hydrocarbon decomposition on metallic single crystals is one of the best known techniques for growing high quality graphene layers. Before graphene itself attracted the attention it holds nowadays, the study of graphitic layers forming at transition metal surfaces was deeply studied. These ultra-thin carbon layers were explained to emerge from the segregation of carbon trapped in the single crystals, and they were forced to occur by exposing the metallic substrates to controlled flows of hydrocarbons at elevated temperatures [8, 9, 10, 11, 12, 13].

Today this method is used to grow epitaxial graphene layers in a controlled way. The specific parameters vary from metal to metal, but the mechanism involved is the same: the dehydrogenation of hydrocarbons on the surface of the catalytic metal leads to the formation of the sp^2-hybridized graphene honeycomb lattice.

Epitaxial growth of graphene has been accomplished in many transition metals and its properties have been studied by many different techniques such as X-Ray Diffraction (XRD) [14] [15], X-ray Photoelectron Spectroscopy (XPS) [16], LEED [17] and STM [18] [19] [20]. From the cited works one can extract that the interaction of graphene with metallic substrates modifies most of its intrinsic properties, and that this interaction varies in intensity from metal to metal. This interaction can be quantified by means of near-edge x-ray absorption spectroscopy (NEXAFS) as a function of the *d* orbital occupancy of the transition metal, which is related to their hybridation with the graphene π orbitals due to the charge transfer between them [16]. Photoelectron spectroscopy (PES) experiments also show a splitting in the C 1s peak in those metals in which the interaction is stronger [16].

Taking into account the intensity of the graphene-substrate interaction, we can classify the resulting graphene/metal systems as weakly or strongly coupled. In this framework, graphene/Ru(0001) would fall into the strongly-coupled class, while metals such as platinum or iridium are considered to interact weakly with graphene [21].

A structural characteristic of the weakly coupled systems, such as graphene/Ir(111), is the presence of multiple superstructures related to the orientation of the graphene honeycomb lattice with respect to the substrate [22, 23, 24]. These moirés present a smooth corrugation (~0.1Å) and the graphene overlayer is prone to the appearance of wrinkles. The electronic structure of this kind of systems still resembles that of free-standing graphene, presenting the characteristic Dirac cone in their band structures, but shifted 110meV above the Fermi energy [25], i.e., graphene/Ir(111) is p-doped.

In the case of graphene/Ru(0001), a strongly coupled system, we see a single moiré superstructure (Figure 4-1) that is much more corrugated than in the previous case (~1Å). This superstructure emerges from the lattice mismatch of graphene (0.246nm) and ruthenium (0.271nm), which are also rotated by 0.5º. The resulting moiré unit-cell corresponds roughly to 11(10) unit cells of C(Ru) [19].

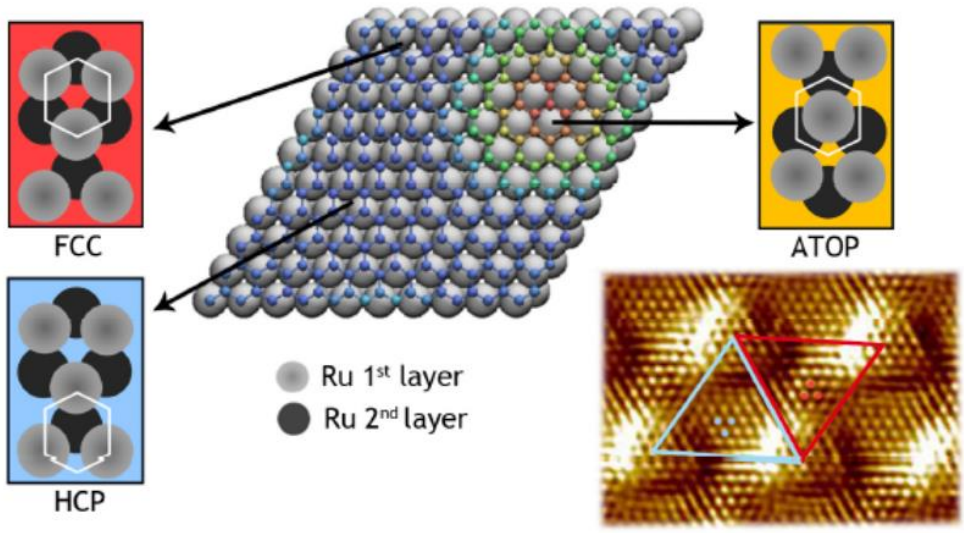

Figure 4-1 – Calculated ground-state geometry of graphene/Ru(0001) with a 11Cx11C/10Rux10Ru periodicity. The color of the C atoms is related to their relative height and the Ru substrate atoms are printed in gray. There are four different regions forming the moiré superstructure, namely atop, HCP, FCC and bridge (areas between HCP and FCC). A STM topographic image with atomic resolution showing the different parts of the moiré is shown (8x5nm^2, V_s=-1mV, I_t=1nA). Blue and red triangles indicate the HCP and FCC zones, and three nonbonding atoms of each region are depicted as dots of the same color. Figure extracted from [26].

The vertical corrugation of graphene depends on the registry of the graphene honeycomb rings with respect to the ruthenium atoms. The high parts of the moiré correspond to those areas where the carbon atoms are not directly on top of the ruthenium atoms, resulting in a lower chemical interaction (atop in Figure 4-1), while the low areas are those where the carbon atoms fall on top of the substrate atoms (HCP and FCC in Figure 4-1), thus interacting stronger. The intermediate zones between the HCP and the FCC zones are called bridge as most of the carbon atoms stand on bridge sites of the underlying ruthenium lattice. Since this naming convention might lead to confusion when compared to the top, FCC snd HCP sdsorption sites of S/Ru(0001) we will refer to them as "higher" and "lower" parts of the moiré.

This topographic periodicity emerging from a chemical interaction modulation between graphene and ruthenium also leads to an in-plane modulation of the electronic structure of the system. The experiments carried out in [19] show that the influence of the ruthenium substrate on the graphene results in a shift of the Fermi level by -0.3eV due to the doping; the appearance of a finite lifetime related to the hybridization of the graphene orbitals with the substrate bands; and a periodic potential with the periodicity of the moiré unit cell. A strong change in the local density of states (LDOS) can be identified when changing from the lower to the upper parts of the moiré unit cell, indicating a depletion of the valence band in the low areas and a depletion of the conduction band in the high areas.

4.1.2 Intercalation of elements in graphene/Ru(0001)

One of the goals in today's material science includes the development of a 2D-material technology, in which graphene plays a fundamental role. As we have seen in the previous section, graphene obtained by CVD methods on single-crystal catalytic surfaces presents a high quality in terms of long-range crystallinity, but the strong interaction with the underlying substrate destroys some of its intrinsic properties, such as the high carrier mobility, the quasiparticle chirality and the linear dispersion relation close to the Fermi level [1]. CVD growth of graphene on metallic, semiconductor and dielectric substrates has been achieved and wide graphene sheets are obtained, but the graphene obtained by this method is very polycrystalline, which also results in the modification of those graphene properties that would be interesting for technology [27].

One of the ways to overcome these limitations would be developing a method to detach the highly crystalline graphene obtained on catalytic metals by UHV techniques and transfer it to a less interacting substrate.

In the last years it has been discovered that graphene grown this way can be intercalated by different materials using variations of a method that consists in the deposition of the desired species on top of the graphene/metal system and a posterior annealing in order to favor its diffusion and intercalation.

The intercalation mechanism is not clear and it might vary for the different species, but most of the peer-review published work suggests that the adsorbed atoms penetrate the graphene layer through edges and point defects [28] or by an exchange mechanism between the adsorbed element and the graphene's carbon atoms [29]. It is generally accepted that those species that are able to interact strongly with graphene and activate the C-C bonds intercalate through the second mechanism and those who are mostly inert to graphene do it through the first one [30].

Since there is a long bibliography regarding the different substrates and intercalated species, we will focus here on the intercalation of atoms underneath graphene grown on the basal plane of ruthenium, which is the starting point of our own work. The results obtained for other substrates are qualitatively similar, being the main difference the strong interaction between graphene and Ru(0001).

Intercalation of a wide variety of elements between graphene and Ru(0001) has been achieved. The chemical and electronic properties of the intercalated species are also very different: intercalation has been demonstrated for metals such as gold [31], palladium [32], lead [33], nickel [30], platinum, cobalt, indium or the rare earth cerium [34]; semiconductors such as silicon [35]; and very electronegative non-metals such as oxygen [28].

Independently of the intercalated material, all this systems share a common aspect: all of them result in an effective decoupling of graphene from ruthenium to a greater or lesser extent. The difference in interaction depends on the interaction of the adsorbed layer with both graphene and substrate, the geometry of the intercalated layer and graphene-substrate distance effects induced by the intercalated layer. As so, it has been shown that those metal layers that adsorb pseudomorphically on the Ru(0001) plane, such as cobalt and palladium, keep a strong corrugation in the moiré superstructure induced by the substrate [32], while the intercalation of gold, indium or cerium, that adsorb in different sites with different geometries, results in a change in the moiré superstructure [34]. Intercalation of a single layer of silicon results in a strong attenuation of the moiré superstructure, indicating an effective screening of the C-Ru interaction, while adding a second layer of this material results in a completely flat graphene layer [35].

The decoupling of the graphene layer after intercalation has been demonstrated by means of angle-resolved photo-emission spectroscopy (ARPES) experiments that show the recovery of the Dirac cone in the electronic structure of graphene after silicon [36] and gold [31] were intercalated. In the case of gold, a small forbidden energy band-gap appears close to the Fermi level while the linear behavior is preserved. This gap is attributed to a symmetry breaking of the two carbon sublattices that result in a weak breaking of the chiral symmetry.

Another indication of the effective decoupling of graphene by intercalation of some elements is the appearance of an interference superstructure around point defects of silicon-intercalated graphene/Ru(0001) [35] which has usually been related to the inter-valley scattering of electrons behaving as chiral fermions [37]. This behavior is suppressed in graphene on metals [38] and only appears around point defects and extended edges in free-standing or decoupled graphene.

Intercalation of sulfur under graphene has not been investigated for graphene/Ru(0001) nor any other substrate and represents the main topic of this thesis. The high reactivity of sulfur and ruthenium and the wide variety of surface reconstructions that S/Ru(0001) presents (see Chapter 3) give this system different properties. These depend strongly on the amount of intercalated sulfur and the geometry it adopts under graphene. Its structural and electronic properties, along with the experimental procedure employed to obtain the intercalated system, are presented in the next sections.

4.2 GRAPHENE/S/RU(0001) SAMPLE PREPARATION

This section deals with the details in the preparation of graphene/S/Ru(0001) samples. First we explain the growth of graphene on ruthenium by means of catalytic decomposition of C_2H_4, as it is the starting point in order to get the intercalated system. Then we explain the intercalation process of sulfur when exposing a previously grown graphene/Ru(0001) sample to H_2S.

4.2.1 Graphene on Ruthenium(0001) sample preparation

In order to grow graphene on the basal plane of ruthenium we first need a single crystal of ruthenium cleaved in the (0001) plane and polished by mechanical methods. During this work we had to our disposal three different ruthenium single crystals which we used indistinctly obtaining the same results.

The Ru(0001) single crystal is placed in an UHV chamber with a base pressure of 10^{-10}mbar and cleaned by a series of cycles consisting in Ar^+ ion sputtering and subsequent annealing in an oxygen atmosphere. The ion sputtering was made by means of an argon ion gun with an acceleration voltage of $V_a = 1.47kV$ and an argon partial pressure of $1 \times 10^{-6}mbar$ for 5 minutes. The annealing was performed in an oxygen atmosphere of $1 \times 10^{-7}mbar$ during 3 minutes while annealing at 1150K by electron bombardment. The reason for performing the annealing in oxygen is to remove the carbon imputiries diffusing from the bulk, thus preventing the formation of an unwanted carbon overlayer. After the heating, the electron bombardments is switched of and the sample is cooled to room temperature with the oxygen leak valve still open, leading to the formation of an oxygen (2x2) superstructure that passivates the Ru(0001) surface [39]. After the pressure is recovered, a 30 seconds flash at 1400K removes the oxygen layer, resulting in a clean and atomically flat Ru(0001) facet.

After a few preparation cycles the sample is clean and flat and we proceed to the growth of the epitaxial graphene layer. To do so, we reduce the temperature from 1400K to 1150K after the last high-temperature flash and expose the sample to a partial pressure of $1 \times 10^{-7}mbar$ of ethylene (C_2H_4) during 7 minutes. The C_2H_4 molecules reaching the surface are dehydrogenated and the carbon atoms diffuse all over the sample forming large domains of graphene. The sample is then flashed for 30 seconds at 1400K in order to desorb any impurity or ethylene molecule that could be adsorbed on top of the graphene layer.

4.2.2 Intercalation of sulfur in graphene/Ru(0001)

In order to obtain an intercalated layer of sulfur underneath graphene we grow graphene/Ru(0001) using the previously described method and then expose the system to H_2S in order to intercalate sulfur.

By controlling the deposition parameters (H_2S pressure and exposure time) we are able to grow and identify different types of intercalated sulfur layers, closely related to the reconstructions described in the previous chapter for S/Ru(0001). Classification of the coverage regimes is not as straightforward as in the S/Ru(0001) case, at which we had regions of pure (√3x√3)R30º, domain-wall and c(2x4)-2S phases. In the intercalated system the different phases of sulfur coexist for most coverages as isolated domains.

The coverage and geometry of the intercalated sulfur layer play important roles on the properties of the graphene that lies on top of it. As we have seen in the previous sections, the different zones of moiré superstructure of graphene on ruthenium are related to the relative position of the carbon honeycomb lattice respect to the different threefold symmetry sites of the ruthenium substrate. The different reconstructions of sulfur on ruthenium adsorb in part of these sites with very local bonds, altering the interaction of graphene with the substrate. In this system, we are able to identify both the DW and the c(2x4)-2S phases after long exposures to H_2S, but we do not observe the formation of the hexagonal (2x2) and (√3x√3)R30º phases.

4.3 INTERCALATED SULFUR DOMAIN-WALLS IN GRAPHENE/RU(0001)

Short exposures to H_2S ($1 \cdot 10^{-8}$-$5 \cdot 10^{-8}$mbar up to 2min) do not seem to alter the graphene/Ru(0001) surface. After increasing the exposure to H_2S (10^{-7}mbar, 2-10min) we observe an overall change of appearance of the surface. Flat graphene islands of varying sizes start to appear in the corrugated moiré background, and their mean width increases with increasing sulfur coverage. These islands also present a moiré lattice with lateral dimensions similar to that of graphene/Ru(0001), but their corrugation is one order of magnitude lower. The regions outside these islands conserve the strongly corrugated moiré pattern of graphene/Ru(0001).

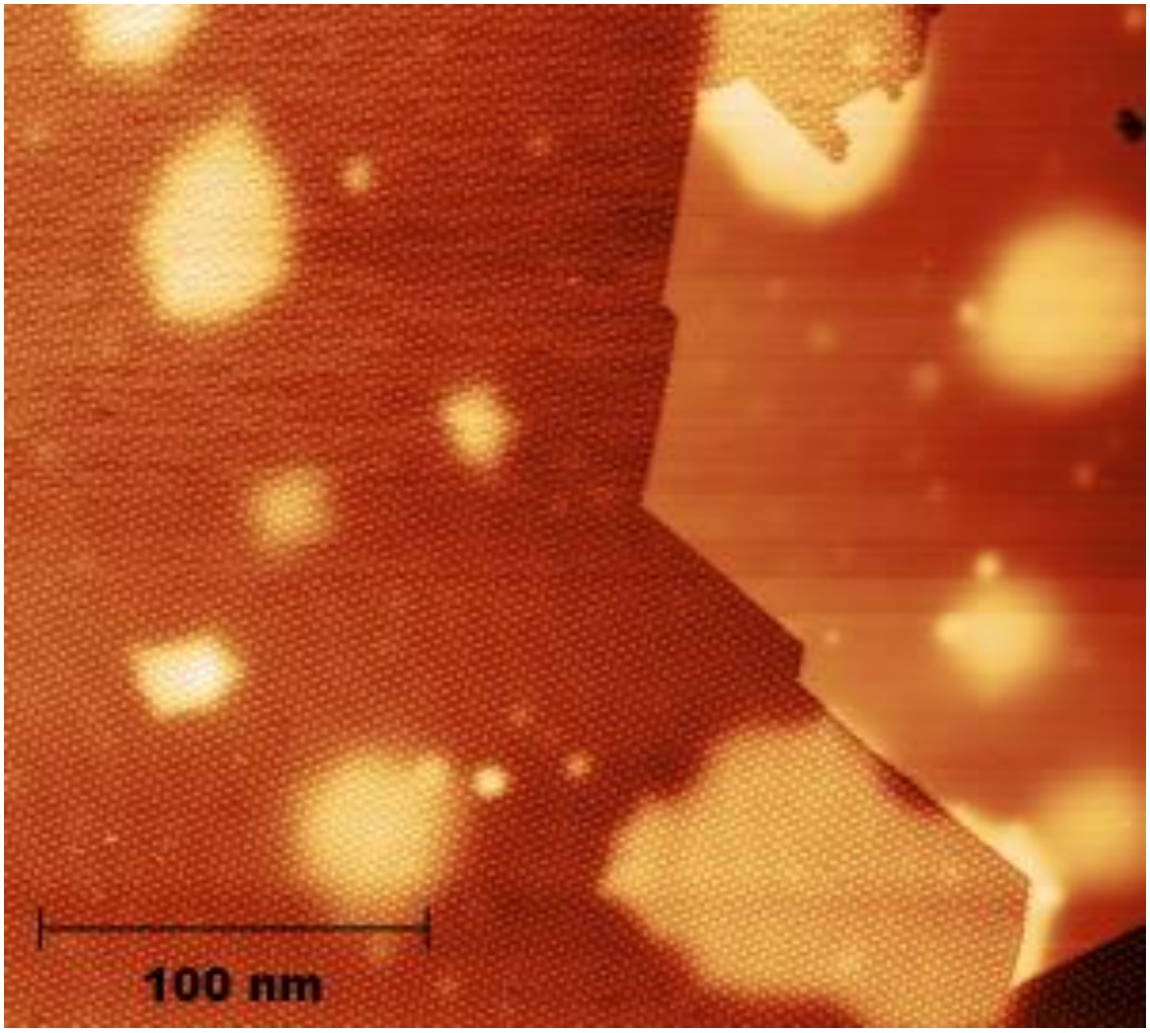

Figure 4-2 – Room-temperature STM topographic image of single substrate terrace in a region with a wide domain-wall island (right) surrounded by graphene/Ru(0001) (left). The moiré pattern of graphene/Ru(0001) can easily be identified in the left part of the image while the S-intercalated region seems completely flat. The edges of the graphene/S/Ru(0001) island follow the moiré superstructure. The brighter blobs are bubbles in the Ru substrate. V_s=2V, I_t=100pA.

The moiré superstructure we observe in the corrugated zones looks very similar to that in the non-intercalated case, and appears as a result of the interaction of the different regions of the substrate with the graphene layer. The lateral dimensions are exactly the same as in the non-intercalated case, with a unit cell of 11 C bonds (10 Ru bonds). The apparent corrugation height of this moiré is large compared to weak-interacting systems such as graphene/Ir(111), but for negative bias voltages is almost the same as in as-grown gr/Ru(0001). When taking images with $-4V<V_s<-1V$ we get an RMS corrugation around 1Å, that is, within experimental error, the same as in graphene/Ru(0001) [20].

When taking STM topographic images of as-grown graphene/Ru(0001), raising the sample voltage above -1V leads to a smoothing of the apparent corrugation of the moiré pattern until a contrast inversion takes place at around 2.7V (Figure 4-3), making the high parts to look deeper than the low parts (Figure 4-4). In the case of graphene/Ru(0001) after exposure to H_2S, this contrast inversion takes place at around 3.1V. The difference between these values is not enough to assume a different behavior between the two systems, since this kind of effects are subjected to changes in tip parameters that make them fall within experimental error.

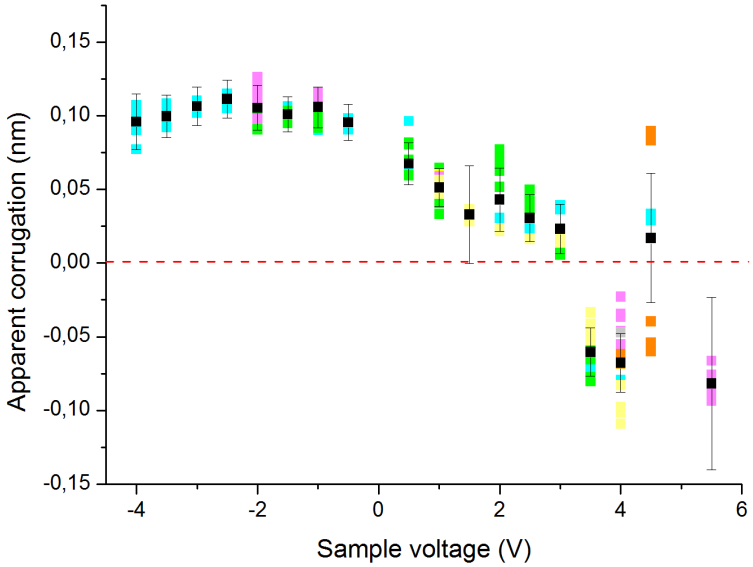

Figure 4-3 – Apparent corrugation of the graphene/Ru(0001) moiré after exposure to H_2S as seen by the STM tip at different biases. The data corresponds to different tips and samples, each different set of measurements is depicted by a different color. The black squares represent the mean value of the whole dataset, along with the statistical error. All the data used for this graph was measured at 4K.

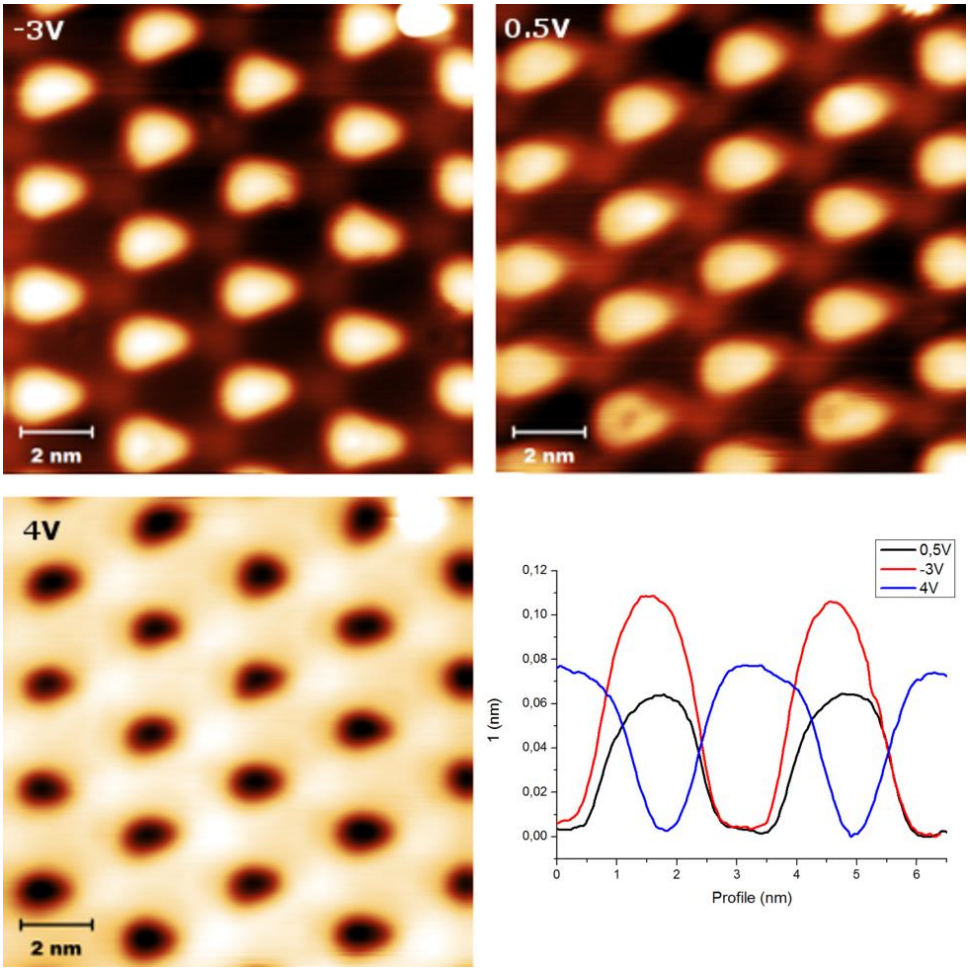

Figure 4-4 – Contrast inversion of graphene/S/Ru(0001) with tip bias voltage. The bias is indicated in each panel. The graph shows three profiles taken in the same zone for the three different voltages. In the occupied states at -3V the corrugation is ~1Å, at 0.5V it is ~0.6Å and at 4V the contrast is inverted and the apparent corrugation is ~0.8Å. All the images were taken at 4K with a tunneling current of 100pA. The graph represents a profile of each panel taken at the same line.

In as-grown graphene/Ru(0001) it has been demonstrated that this contrast inversion is related to the difference in energy of the image states of graphene at different distances of the substrate and was discussed in [20]. STS experiments in the field emission regime presented in take account of the contrast inversion in graphene/Ru(0001) after exposure to H_2S in a similar way (Figure 4-5).

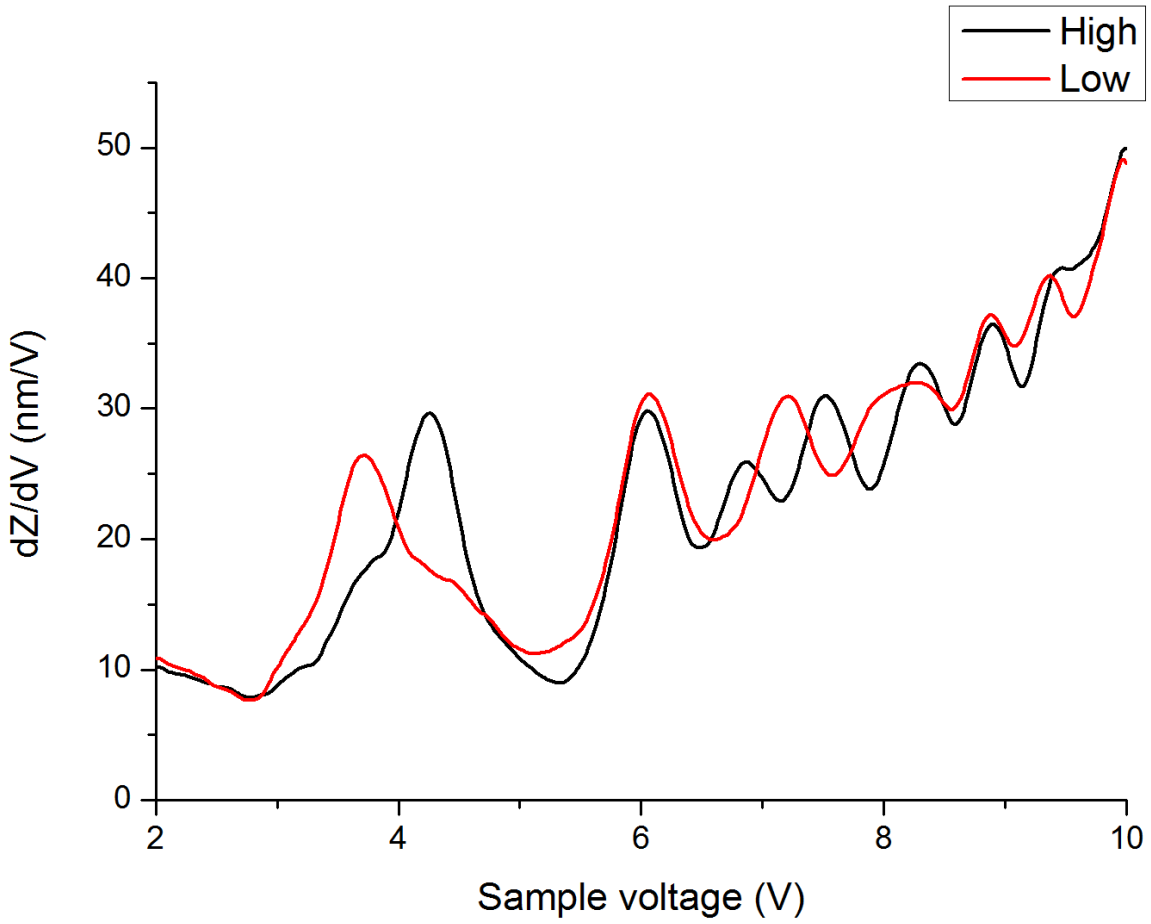

Figure 4-5 – STS spectra in the field emission regime of the low-coverage graphene/S/Ru(0001). The black line represents the FER spectrum of the high parts of the moiré and the red one that of the low parts. The difference in the first FER (between 3V and 5V) of the two zones results in the contrast inversion of the topographic images. The experimental curves are taken as Z-V spectra, the numerical dZ/dV curves are shown for clarity.T=77K.

STM experiments show that the flat graphene/S/Ru(0001) islands imaged with a tip bias voltage of 50mV and a tunneling current of 20nA show a corrugation of the moiré in the range of 0.1Å, i.e., is almost one order of magnitude below that of the moiré of graphene/Ru(0001). The orientation and lateral dimensions of the moiré appearing in these regions coincide with those of graphene/Ru(0001) within experimental error.

In atomically resolved images of the graphene/S/Ru(0001) islands one can identify an ordered array of brighter bumps embedded in the flat graphene lattice with a slightly longer periodicity (Figure 4-6). By taking 2D Fourier transforms the characteristic phase-space pattern of the DDW phase of S/Ru(0001) can easily be identified, along with the graphene lattice and the moiré superstructure (Figure 4-6 - inset).

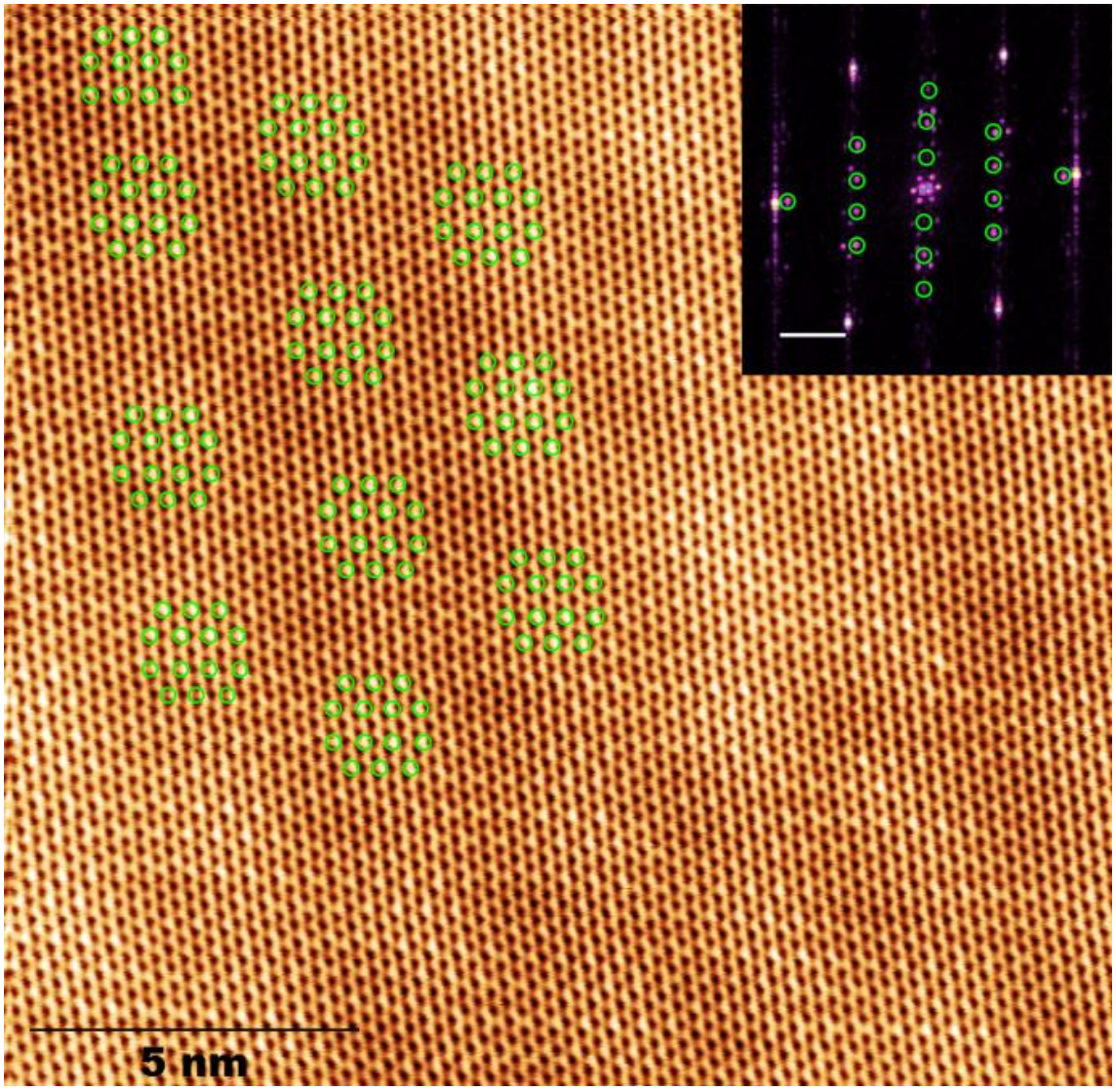

Figure 4-6 – STM topographic image of a graphene/S/Ru(0001) sample taken at T=300K with V_s=5mV and I_t=2.8nA.The intercalated sulfur domain walls are manifested as brighter bumps in the graphene honeycomb lattice A smooth moiré is still visible after intercalation. The DWs are easier to observe in the high parts of the moiré. The inset shows the central region of the 2D-FFT of the main figure with the dots corresponding to the sulfur DW lattice circled in green. It is worth noting that the DW structure is commensurate with Ru, but not with graphene, as left (right)-most spots do not match the first order spots of the graphene lattice. Inset scale-bar: 2nm^{-1}.

The Fourier transform of Figure 4-6 reveals some interesting information. First of all, it is evident that the sulfur below graphene is forming the domain-wall structure characteristic of S/Ru(0001), and that locally its coverage is close to the DDW coverage (θ=0.42). The lengths of the reciprocal vectors coincide with those of the system without graphene. This, together with the intensity of the satellite spot of ruthenium around the first order of the graphene pattern in the direction perpendicular to the domain walls indicate that sulfur is commensurate with the substrate and not with graphene. This implies that the interaction of sulfur with ruthenium is much stronger than with the graphene layer on top. We can also see a replica of the moiré spot structure around the DDW spots, which means that they somehow follow the graphene superstructure. In the real-space image, we can see how the bright bumps in the graphene lattice induced by the intercalated sulfur are clearly more visible in the high parts of the moiré.

When cooling down to 4K, the atomic resolution shows a particular effect depending on the tip-sample voltage: for positive bias voltages below ~500mV (Figure 4-7a), the graphene honeycomb lattice can be seen with almost no sign of the intercalated sulfur, but at higher voltages (Figure

4-7b) the graphene becomes invisible to the tip and we have access to the sulfur below. The images at these voltages give us direct access to the intercalated layer structure and show the positions of the intercalated sulfur atoms in the DW phase.

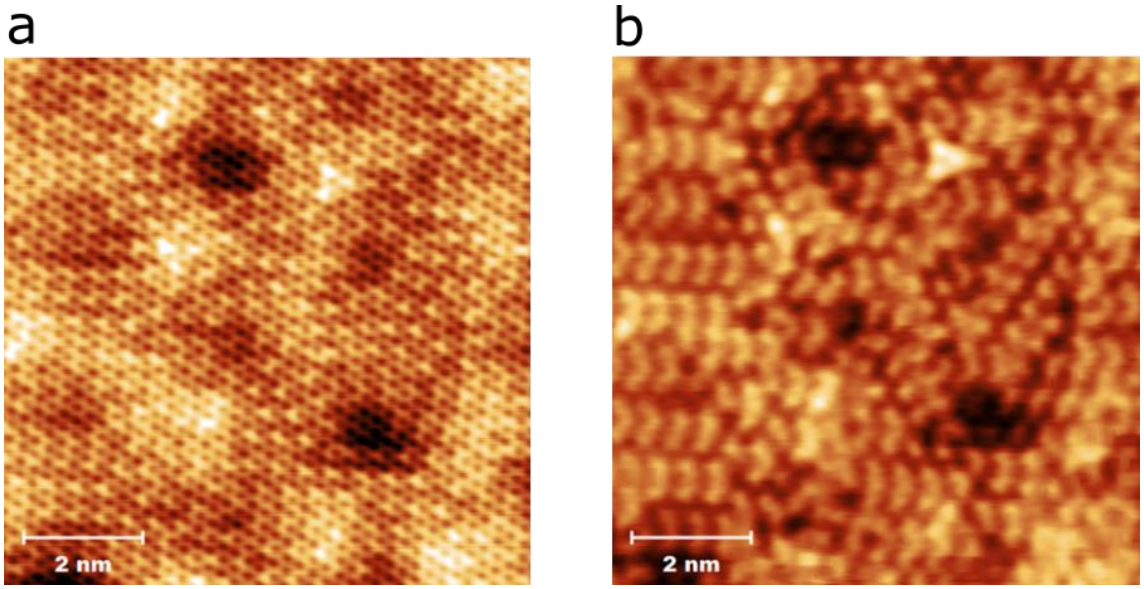

Figure 4-7 – Two STM topographic images of the same area of the domain-wall phase in graphene/S/Ru(0001) taken at different tip-sample voltage. (a) Shows the graphene lattice and the moiré periodicity (V_s=200mV) while (b) shows the underlying sulfur structuress (V_s=1V). In both cases the tunneling current is I_t=700pA and T=4K.

A similar effect has been observed for graphene on silicon carbide (SiC) [40] [41] [42] [43]. When graphene is standing on top of a Si-terminated SiC, the graphene lattice is always visible, when imaged at sufficiently low voltages. But when it lays on the C-terminated face of SiC, one can image the graphene layer on top or the underlying substrate surface depending on the voltage bias applied to the tip. This behavior is attributed to the electronic structure of the system [44], in particular STS experiments show that there is a small gap-like feature around the Fermi level that could be responsible for this effect [40].

4.3.1 Influence of the moiré superstructure in the DW structure of graphene/S/Ru(0001)

Tuning the sample voltage to the regime at which the sulfur is visible without interference of the graphene layer, we can get a deeper insight on the actual structure of the sulfur layer. While it keeps the characteristic geometry of the domain walls in S/Ru(0001), we can identify different regimes in the intercalated samples. The different regimes coexist in the DW-intercalated graphene/S/Ru(0001) but present a different local coverage.

For low local coverages we observe regions of short DWs pointing in the three main symmetry directions and with a high density of DW crossings (Figure 4-8). In this zones, the (√3x√3)R30 domains separated by the DWs are arranged in a periodic fashion below the low parts of the moiré, while the DWs concentrate below the high parts. In S/Ru(0001), DWs form wide domains of long parallel domain walls at which DW crossings are prevented, since their mutual interaction is repulsive.

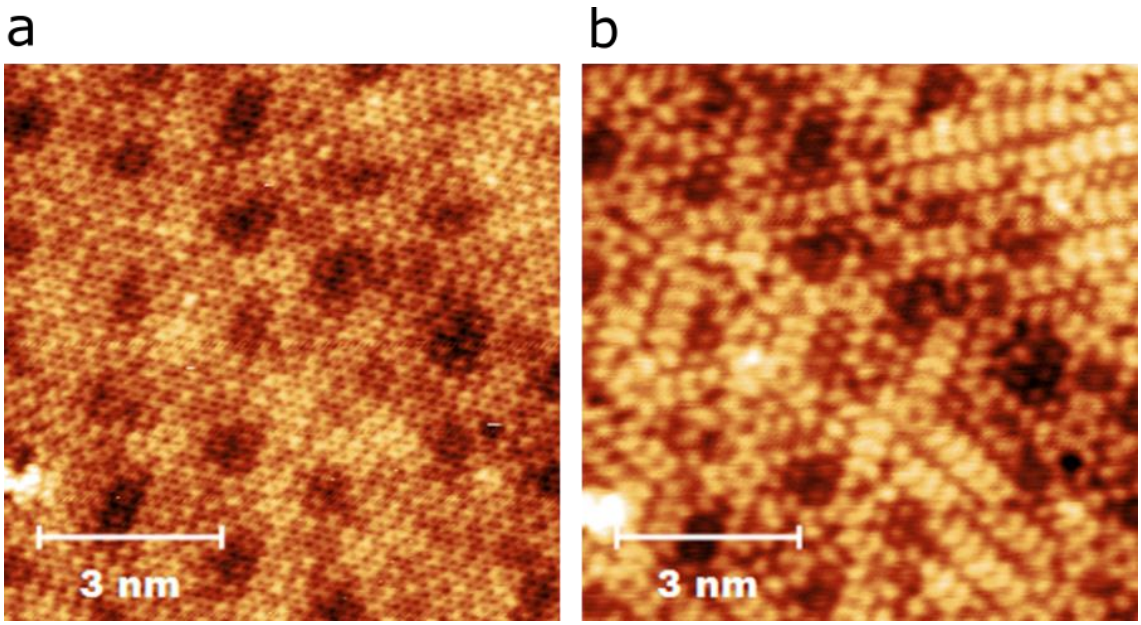

Figure 4-8 – STM topographic images taken at 77K of a high-coverage S-intercalated graphene/Ru(0001) sample. The domain-walls are less dense and now present a series of domain crossings that lead to the formation of small (√3x√3)R30° domains following the moiré periodicity. In (a) the bias is tuned to see atomic resolution in graphene (V_g=100mV, I_t=300pA), while the tip bias in (b) is tuned to see only the sulfur layer (V_g=1V, I_t=500pA).

At regions with a higher local coverage, the domain walls grow longer, but the stripes are shifted following the moiré superstructure, having a meandering appearance. There is still a higher concentration of the (√3x√3)R30º domains below the low parts of the moiré, and some DWs merge into small c(2x4) domains (Figure 4-9). In these regions, the local coverage is below 0.42ML, at which the (√3x7) DDW reconstruction is formed.

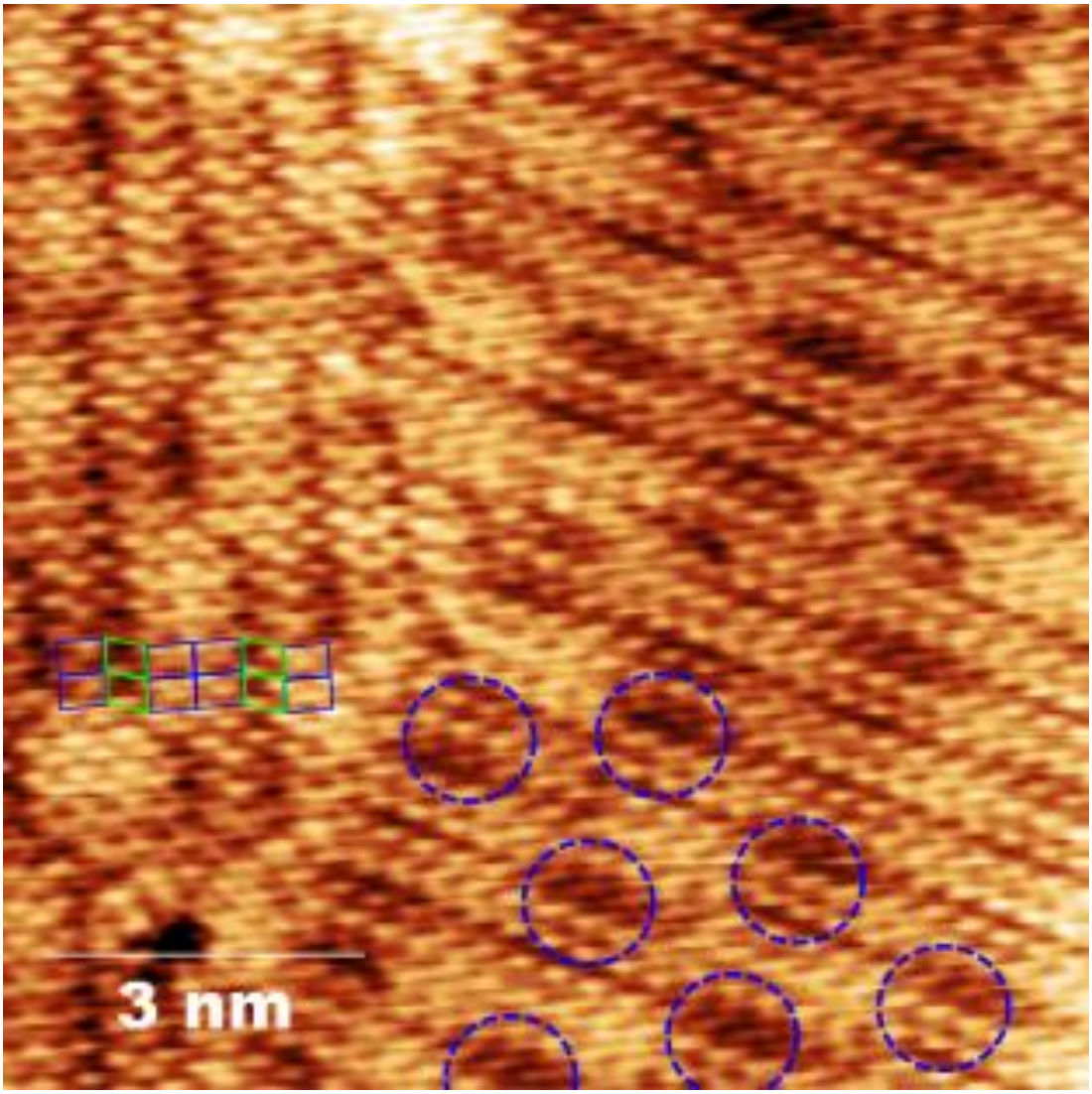

Figure 4-9 – STM topographic image of S-intercalated graphene/Ru(0001) taken at 77K showing the lateral displacement of intercalated sulfur striped domain walls. The domain walls have shifted their directions at certain zones, leading to their merging in some points into small c(2x4) domains, and to the widening of the (√3x√3) regions. We added some unit cells of the c(2x4) (blue) and (√3x√3) (green) lattices to show this effect. The moiré of graphene/Ru(0001) is still visible as darker zones in the sulfur layer, some of them are marked with dashed blue circles. V_s=100mV, I_t=100pA.

The (√3x√3)R30 and (√3x7) reconstructions are not commensurate with the moiré. If we use the building blocks of S/Ru(0001) reconstructions we find that there is a specific coverage at which a DW structure and the moiré of graphene/Ru(0001) are commensurate, namely θ=0.38ML (Figure 4-10). This corresponds to a coverage at which we have two DWs per moiré unit cell.

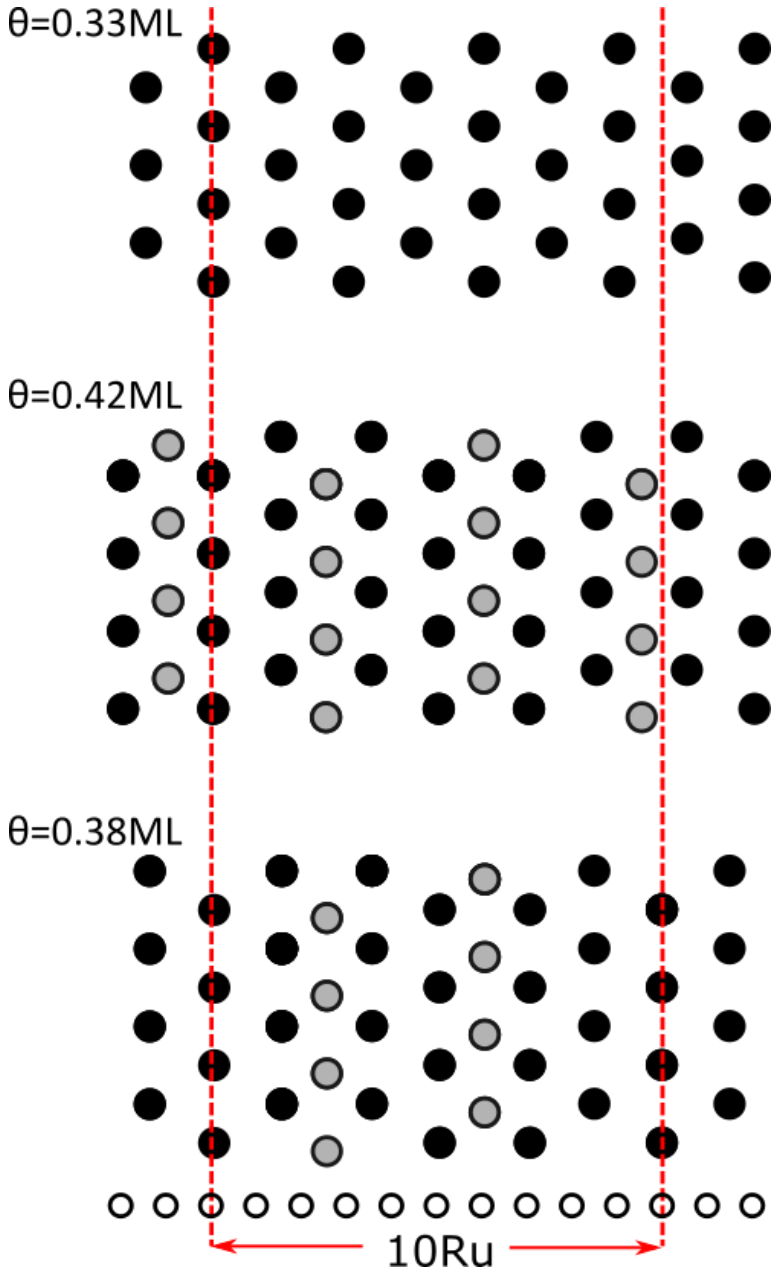

Figure 4-10 – Schematic diagram showing S/Ru(0001) reconstrucctions with coverages of 0.33, 0.42 and 0.38ML compared to the periodicity of the graphene/Ru(0001) moiré in the direction perpendicular to the DWs. The moiré periodicity is marked by red dashed lines, S atoms in HCP positions are depicted as black circles and those S atoms in FCC sites belonging to the DWs are represented as gray circles. Only the θ=0.38ML structure is commensurate with the graphene/Ru(0001) moiré.

In order to keep this commensurate structure all over the surface, the DWs will meander following the periodicity of the moiré. Figure 4-11a shows a schematic diagram of a layer of graphene/S/Ru(0001) at a coverage of 0.38ML and Figure 4-11b shows a room-temperature STM image of a graphene/S/Ru(0001) sample showing the meandering behavior of the domain walls.

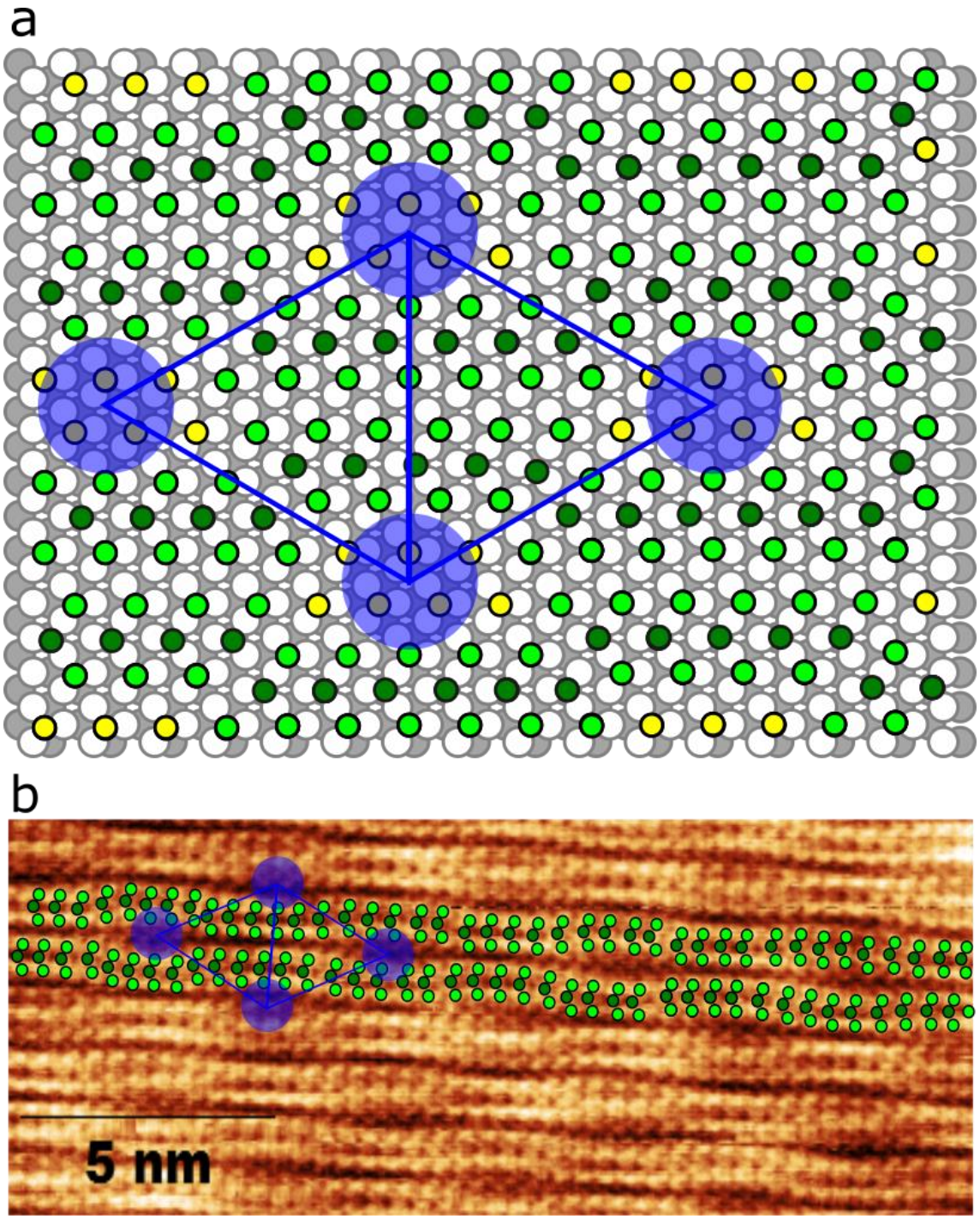

Figure 4-11 – (a) Schematic diagram showing the position of the sulfur atoms in a graphene/S/Ru(0001) sample at a coverage of 0.38ML. Those S atoms belonging to the DWs are shown in light (HCP) and dark (FCC) green, and those in the (√3x√3)R30 domains are yellow. The two first layers of the Ru(0001) substrate are represented by white and gray circles. The graphene lattice has not been represented for clarity, but the moiré unit cell is marked in blue. (b) STM topographic image of a graphene/S/Ru(0001) sample showing the sulfur DWs meandering with the moiré periodicity (T=300K, V_s=500mV, I_t=1nA). Two lines of DWs and the moiré unit cell have been superimposed using the color code of (a).

Finally, we can identify certain regions of the same samples at which the local coverage is 0.42ML and the DWs form the familiar (√3x7) DDW reconstruction of S/Ru(0001)(Figure 4-12). The main difference between the DDWs of S/Ru(0001) and those in graphene/S/Ru(0001) is the size of the domains. While in the former case the rotational domains are up to hundreds of nanometers wide, usually covering complete substrate terraces, in the intercalated samples the rotational

domains are just a few nanometers wide. Also, there is a higher density of dislocations between domains of the same orientation, and small (√3x√3)R30 patches are still present.

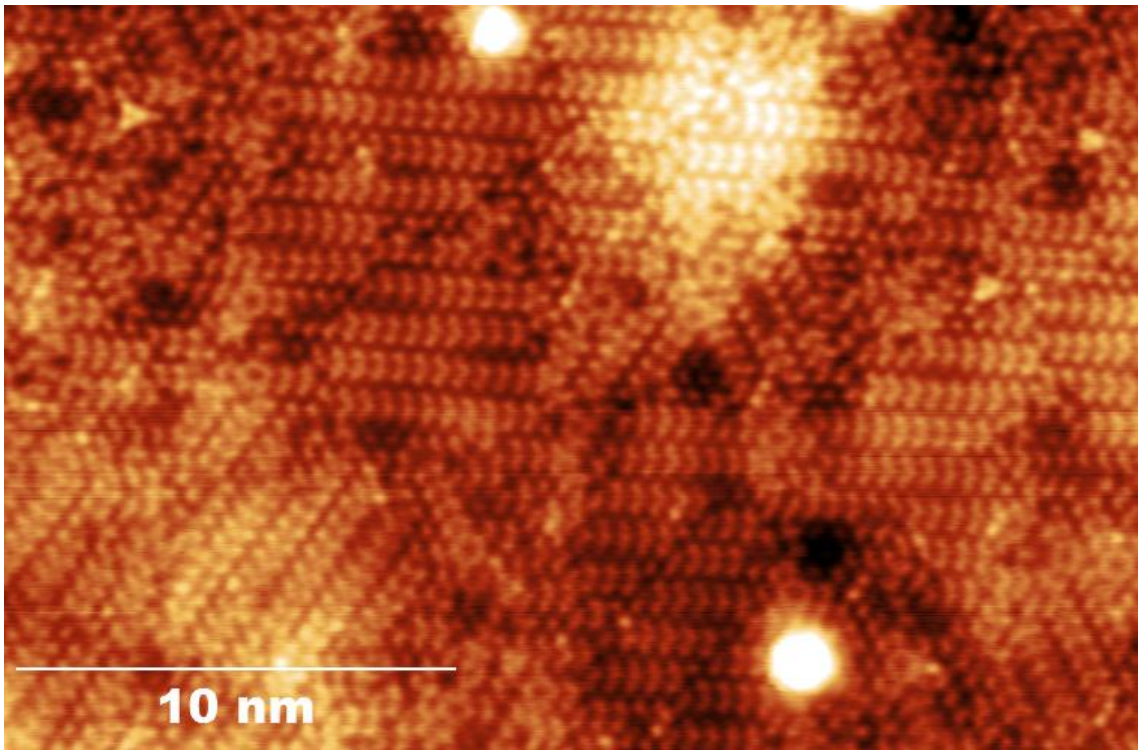

Figure 4-12 – STM topographic image of a graphene/S/Ru(0001) surface with a local coverage of θ≈0.42ML. The intercalated sulfur domains present the characteristic (√3x7) geometry of the DDW phase of S/Ru(0001), but their length is considerably smaller in this case. Some DW crossings can be observed at the interfaces and there are dislocations between DDW domains of the same orientation. The STM parameters are tuned to see the intercalated sulfur layer and not the graphene on top (V_s=1V, I_t=700pA, T=4K)

From this results we can conclude that sulfur intercalates in graphene/Ru(0001) in a DW phase similar to that in S/Ru(0001) (see Chapter 3), but there are important differences between the two systems. First of all, in the case of S/Ru(0001), the DWs appear after a commensurate-incommensurate transition when the atomic density of the surface exceeds that of the complete monolayer of the (√3x√3)R30 reconstruction, i.e. over 0.33ML. In the case of graphene/S/Ru(0001) the system doesn't seem to go through a (√3x√3)R30 phase, and the intercalated islands appearing for short H_2S exposures already present a DW structure. Intercalation of CO molecules between graphene and iridium gives similar results, with the intercalated phase presenting a dense reconstruction even when CO/Ir(111) can adsorb in less dense geometries [45] [46]. Having this into account, it is obvious that graphene is influencing the interaction between the intercalated species and the substrate.

In the case of graphene/S/Ru(0001), the influence of graphene on the geometry of the sulfur layer is directly related to the moiré superstructure. The low parts of the moiré interact strongly with the substrate, the energy of this interaction being comparable to a covalent bond between carbon and ruthenium [16]. On the other hand, the high parts of the moiré can be considered to be almost free-standing [16]. The sulfur atoms will have to overcome a higher energy barrier in order to adsorb below that parts of graphene that interact strongly with ruthenium.

In [47] an analytical study of the effect of defects on the domain-wall systems in adsorbed layers is performed. It shows that the presence of defects and impurities in this kind of systems creates random potentials that locally favor the formation of one of the three possible phase domains. In the case of systems forming parallel striped DWs, which is the case of S/Ru(0001) , the distortion

caused by defects can lead to the deviation of the walls from their preferential direction. Although S/Ru(0001) forms a repulsive striped DW phase at which crossings are prevented, in [48] DW-crossings are observed near nm-scale defects in S/Ru(0001) after annealing the sample and lowering the temperature back to 200K. The proposed mechanism for the formation of DW-crossings after annealing implies the transition into a honeycomb DW phase at high temperatures due to the breathing entropy argument [49] [50], and the recovery of the striped geometry after cooling, leaving the short DWs and their crossings pinned to the defects [47] [48].

One interesting aspect of the behavior of DWs in graphene/S/Ru(0001) is the existence of a transition between an irregular honeycomb network at which crossings are favored into an array of striped DWs. It has been suggested that in uniaxial systems that undergo commensurate-incommensurate transitions, there exists an intermediate honeycomb phase between the commensurate phase and the incommensurate striped DW phase [51]. The appearance of a narrow honeycomb phase comes from the competition between the breathing and meandering entropies, which have a different temperature dependence [51]. Considering our results it is possible that we are observing that kind of transition in the graphene/S/Ru(0001) system.

Our hypothesis is that the moiré of graphene/Ru(0001) is acting as a periodic array of defects, effectively guiding the DWs and forcing them to adapt to the long-range superstructure. There is a competition between the C-Ru bond in the low parts of the moiré, and the repulsive interaction between DWs that prevents sulfur from adopting the striped geometry. For low coverages the DWs are arranged in a disordered honeycomb-like structure around the low parts of the moiré because it is energetically more favorable for the DWs to form crossings than to break the C-Ru bonds. Increasing the coverage and thus the density of DWs, there is no way to keep the graphene and the Ru(0001) substrate bonded and the DWs recover their striped geometry, but they still meander to dodge the higher potential areas. Once the coverage reaches 0.42, the most energetically favorable geometry is that of a striped array of parallel DWs rather than the formation of a denser structure (i.e. the c(2x4) phase) in the higher potential regions. Further increase in the coverage leads to the formation of dense c(2x4) domains which are explained in the next section.

4.4 INTERCALATED C(2X4) SULFUR DOMAINS

After long exposures to H_2S (up to 10min at 10^{-6}mbar), most of the surface of graphene/S/Ru(0001) shows the flat graphene appearance characteristic of the sulfur-intercalated DW phase. When tuning the voltage in order to obtain atomic resolution for the sulfur layer to the voltage window at which the graphene is invisible to STM, we can perfectly see the DW structure. These DW zones present the three rotational domains and cover areas of hundreds of nanometers and up to a micron.

These wide domain-wall areas are separated by elongated regions of sulfur c(2x4) domains, with lengths of the order microns and widths in the 3-15nm range. Due to their meandering behavior we will refer to this zones as “c(2x4) rivers”. Long range images show that disperse patches of graphene/Ru(0001) showing its characteristic moiré pattern are still present. Longer exposures do not seem to end up forming a complete layer of the c(2x4) reconstruction.

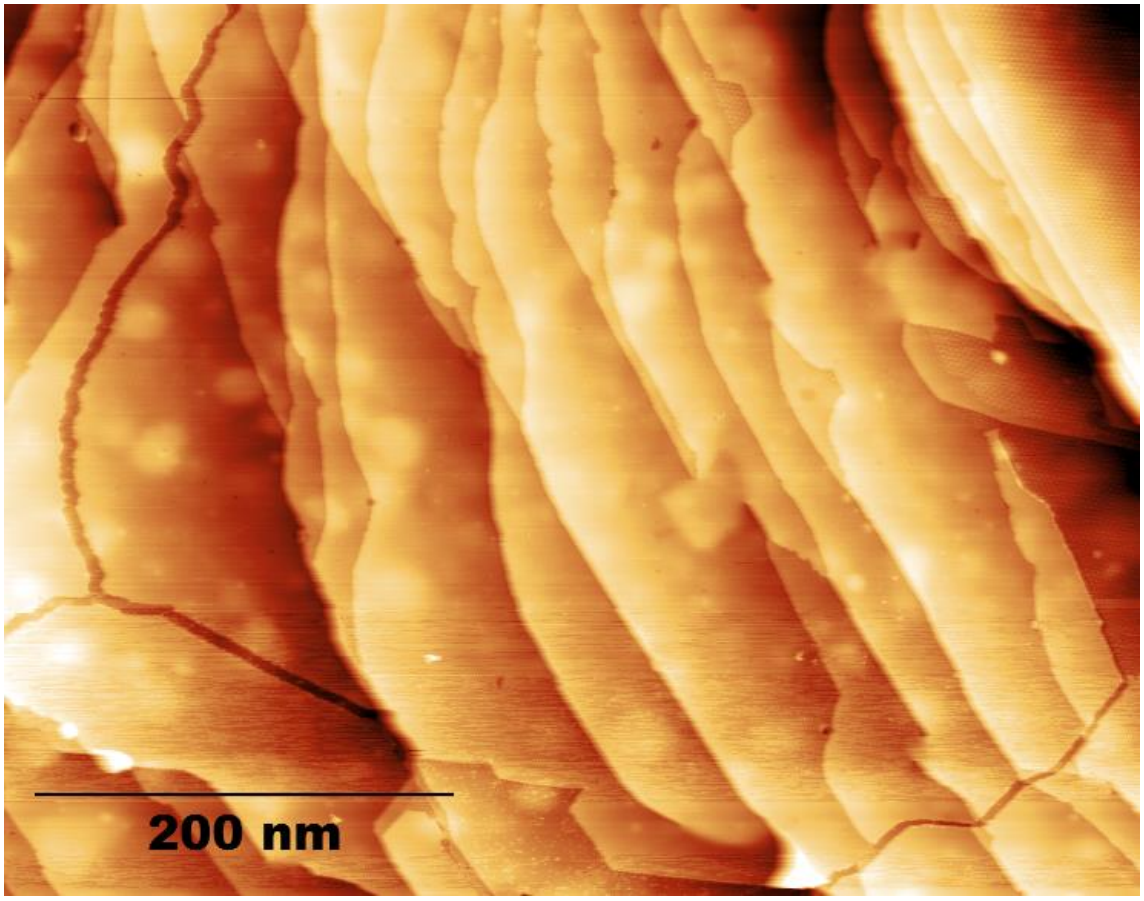

Figure 4-13 – Wide STM topographic image taken at 300K showing the appearance of river-looking domains of c(2x4) intercalated sulfur (long dark regions separating the majority DW phase). In this image an intersection of two of this domains can be seen, one of them being more than 600nm long V_s=1V, I_t=1nA.

In the room temperature STM we can see that these c(2x4) "rivers" do not have a specific behavior regarding the step edges of the surface, being parallel to or crossing them indistinctly. They do follow the three high symmetry directions of the substrate, indicating us a correlation between the three rotational domains of the c(2x4) lattice and the underlying ruthenium. These zones usually end up intersecting with another river, delimiting the boundaries of the DW-intercalated domains (Figure 4-13).

The c(2x4) regions look deeper than the DW-intercalated graphene/S/Ru(0001) domains with an apparent height difference of 2.4±0.3Å when measured at a sample voltage of 50mV with the VT-STM at 300K. This apparent height is comparable to an atomic step of Ru(0001) (2.141 Å).

When cooling down to liquid helium temperature we observe the presence of graphene on top of the c(2x4) sulfur domains. It is the same effect as in the intercalated-DW case, but for this reconstruction the voltage window at which the graphene can be detected is much narrower, i.e. up to only 100mV versus the 500mV of the DW-intercalated regions. When we have access to the graphene lattice with the STM in the c(2x4) intercalated regions, we can see again the characteristic moiré pattern of graphene/Ru(0001) (Figure 4-15 and Figure 4-16).

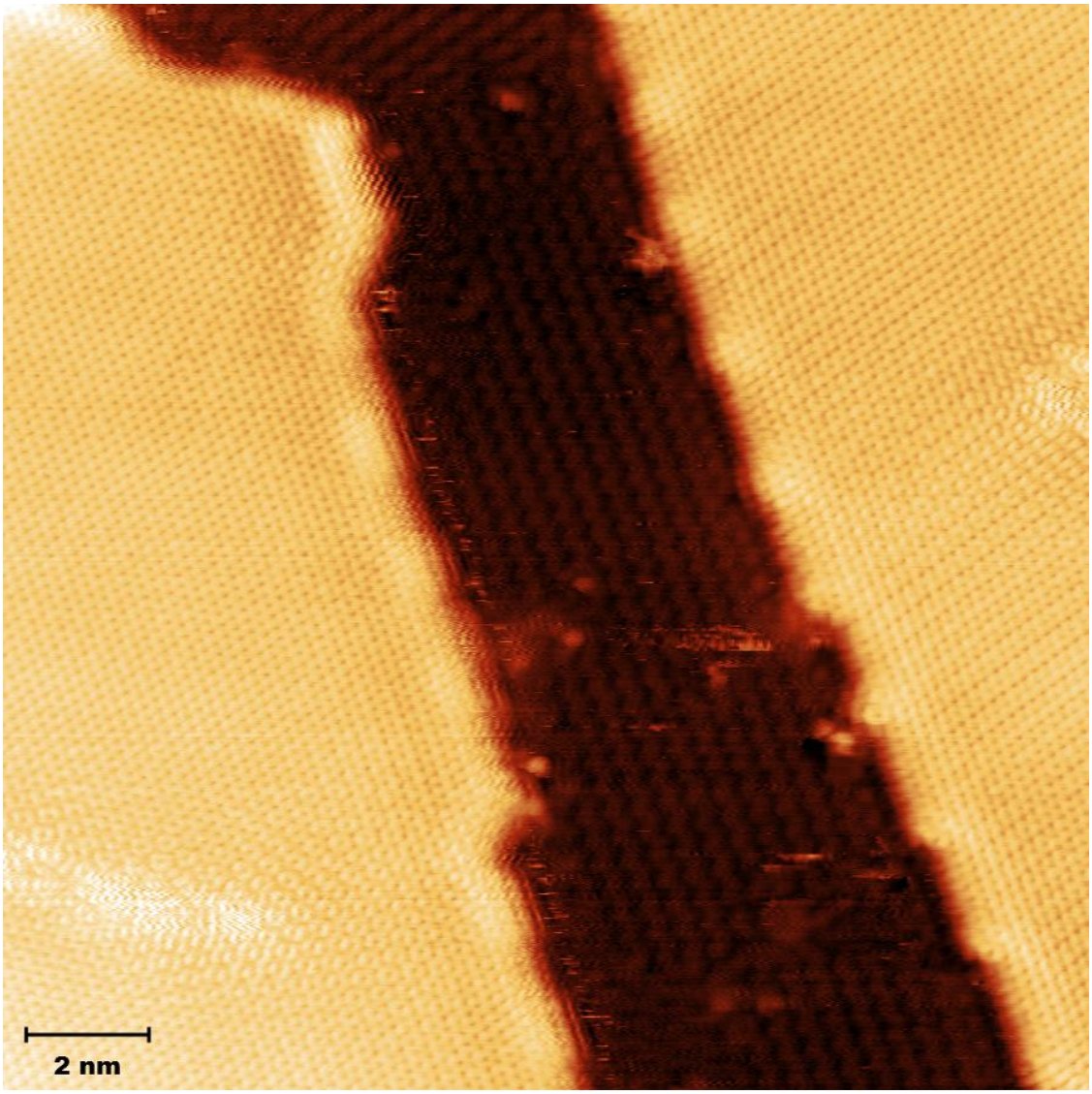

Figure 4-14 – 300K STM topographic image of a c(2x4)"river"(dark) crossing a sulfur domain-wall intercalated graphene region (bright). In the top part of the "river" we can see a change in the rotational domain of the c(2x4) lattice. The (√3x√3)R30° interference pattern associated to electron backscattering can be observed around defects in the DW-intercalated regions and close to the DW-c(2x4) interface. V_s=50mV, I_t=2nA.

When measured at 4K, the apparent step-height of the DW-c(2x4) interface of graphene/S/Ru(0001) depends on whether we are imaging the honeycomb lattice of graphene or the sulfur atoms. In the case we observe graphene in both the DW-intercalated and c(2x4)-intercalated domains, the apparent height is around 1.4±0.2Å. When we see the sulfur lattices in both the DW domains and the sulfur lattice in the c(2x4) domains this height is 2.4±0.3Å. If we tune the voltage in such way that we get access to the sulfur layer in the c(2x4) domains but we still see the graphene lattice in the DW-intercalated regions, this step-height goes up to 3.0±0.4Å.

In the previous subsection we saw how the moiré somehow influenced the structure of the domain-wall reconstruction of sulfur, forcing the (√3x√3)R30º sulfur to stay in the low parts of the moiré while the lines formed by the c(2x4) unit cells of the domain walls followed meandering paths under the higher parts of the moiré. In the case of c(2x4)-intercalated graphene/S/Ru(0001) we do not see any correlation between the rectangular sulfur lattice and the still present moiré superstructure.

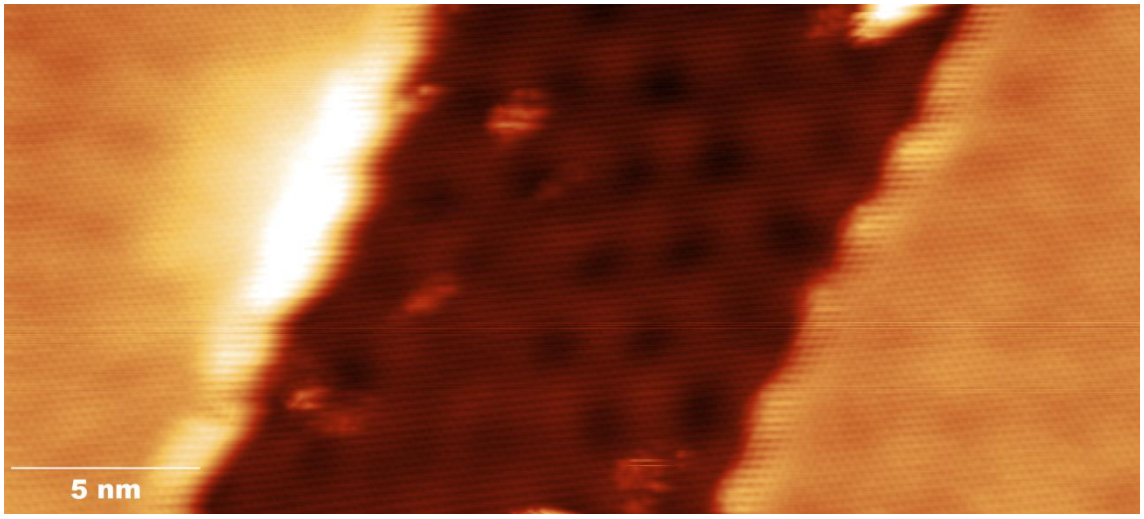

Figure 4-15 – STM topographic image of graphene/S/Ru(0001) sample showing a 15nm wide stripe of c(2x4) sulfur intercalated graphene (dark zone) surrounded by sulfur-DW intercalated graphene (bright zones). Both types of zones show the graphene honeycomb lattice and a dim moiré pattern. T=4K, V_s=100mV, I_t=700pA.

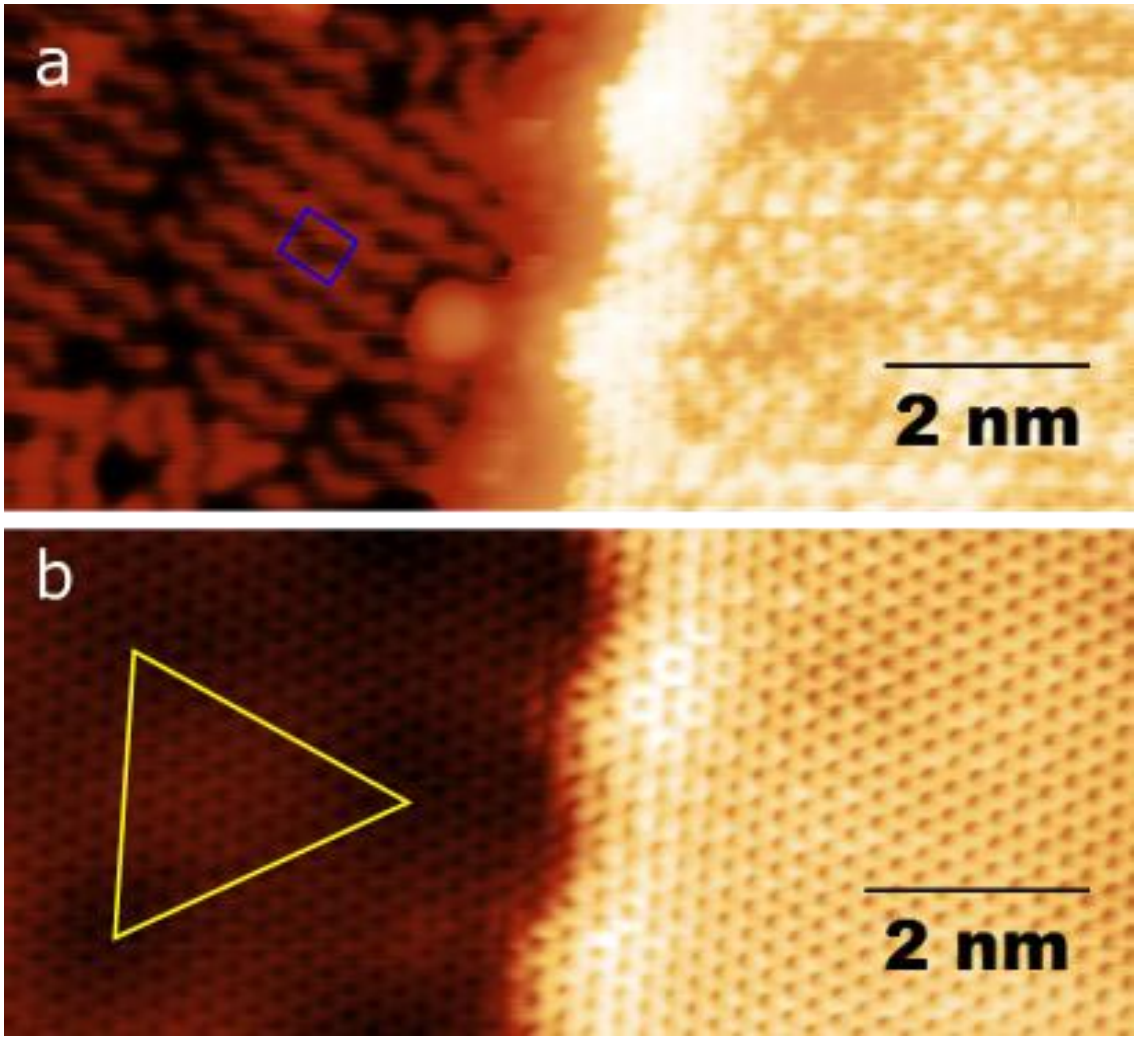

Figure 4-16 – Two STM topographic images taken at 4K showing the effect of the sample voltage in the resolution of the STM. In (a) a sample voltage of 500mV and a tunneling current of 100pA, while in (b) the voltage was 100mV and the current 700pA. (a) shows atomic resolution in DW-intercalated graphene, but not in the c(2x4)-intercalated region. The c(2x4) unit cell is marked in blue. In (b), we have atomic resolution of both regions, showing the continuity of the graphene lattice and the persistence of the moiré in the c(2x4) region. Half a unit-cel of the moiré has been marked in yellow.

4.5 TOPOLOGICAL DEFECTS IN DW-INTERCALATED GRAPHENE/S/RU(0001)

After exposure to H_2S of a graphene/Ru(0001) sample we observe the formation of different defects. Specifically there is a relatively high amount of the so-called flower defects [52] in the intercalated graphene/S/Ru(0001) areas (Figure 4-19) and also in the graphene/Ru(0001) zones (Figure 4-18). These structures usually appear in graphene systems in which the graphene-substrate interaction is weak, and have never been observed in monolayer graphene/Ru(0001) in our own experiments nor in the literature. They are attributed to the presence of atomic-scale defects, mainly loop grain boundaries (GBs) consisting in a closed line of alternating positive and negative disclinations [52] [53] [54]. These disclinations appear in the form of pentagons (heptagons) in the honeycomb lattice of graphene and introduce a rotation of 60º (-60º) between the graphene domains at each side of the disclination [55]. The combination of a positive and a negative disclination forms dislocations. Dislocations induce a relative angle between domains dictated by the distance between them. Grain boundaries are defined as linear arrangements of dislocations and they are usually found in graphene at the interfaces between rotational or translational domains as a way to relax the strain induced by the lattice mismatch [56]. The closed loop boundaries such as the flower defects are a particular case at which the interconnected dislocations form closed lines.

The formation energy of these kind of defects is rather low [52], and both the H_2S dissociation process [57] and de S-Ru bond formation [58] are exothermic. This suggests that loop grain boundaries spontaneously form during the intercalation process. In this picture, intercalation of S atoms underneath graphene will happen at random places of the surface and lead to the formation of localized defects. Diffusion of the intercalated atoms across the Ru(0001)-graphene interface will explain the presence of these defects in the non-intercalated graphene/Ru(0001) zones.

The bright contrast of topological defects in graphene is related to two different effects. The first of them is a purely topographic effect, since the graphene regions around these defects are slightly buckled in order to minimize the formation energy of dislocations [55]. There is also an electronic effect, since the presence of these topological defects induces changes in the LDOS of graphene, enhancing the DOS at low energies [59]. This results in the increase of the apparent height of graphene around defects when observed with STM.

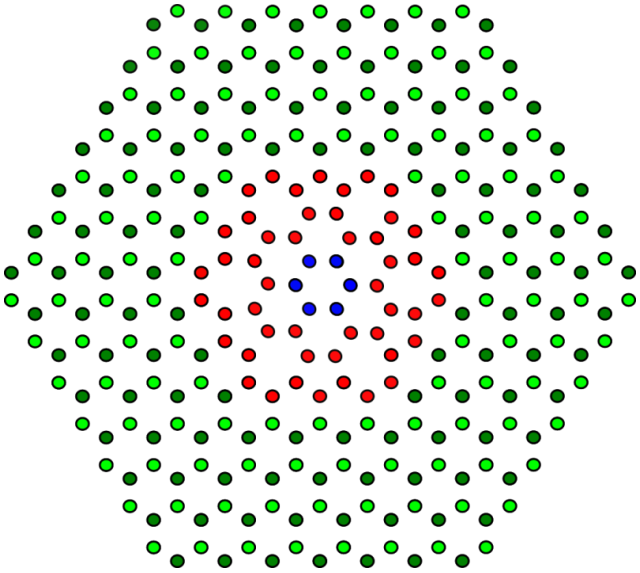

Figure 4-17 – Schematic representation of a flower defect in the graphene honeycomb lattice. The two inequivalent triangular lattices of C atoms are colored in two different shades of green. The atoms that form part of the grain boundary loop, i.e., of the alternating pentagons and heptagons, are colored in red. The blue hexagon in the center of the structure and those surrounding it are rotated 30º respect to those outside the grain boundary. The introduction of pentagons and heptagons in the honeycomb lattice breaks the symmetry of the inequivalent lattices. The electrons in one lattice can interact with those of the other lattice via the topological defect.

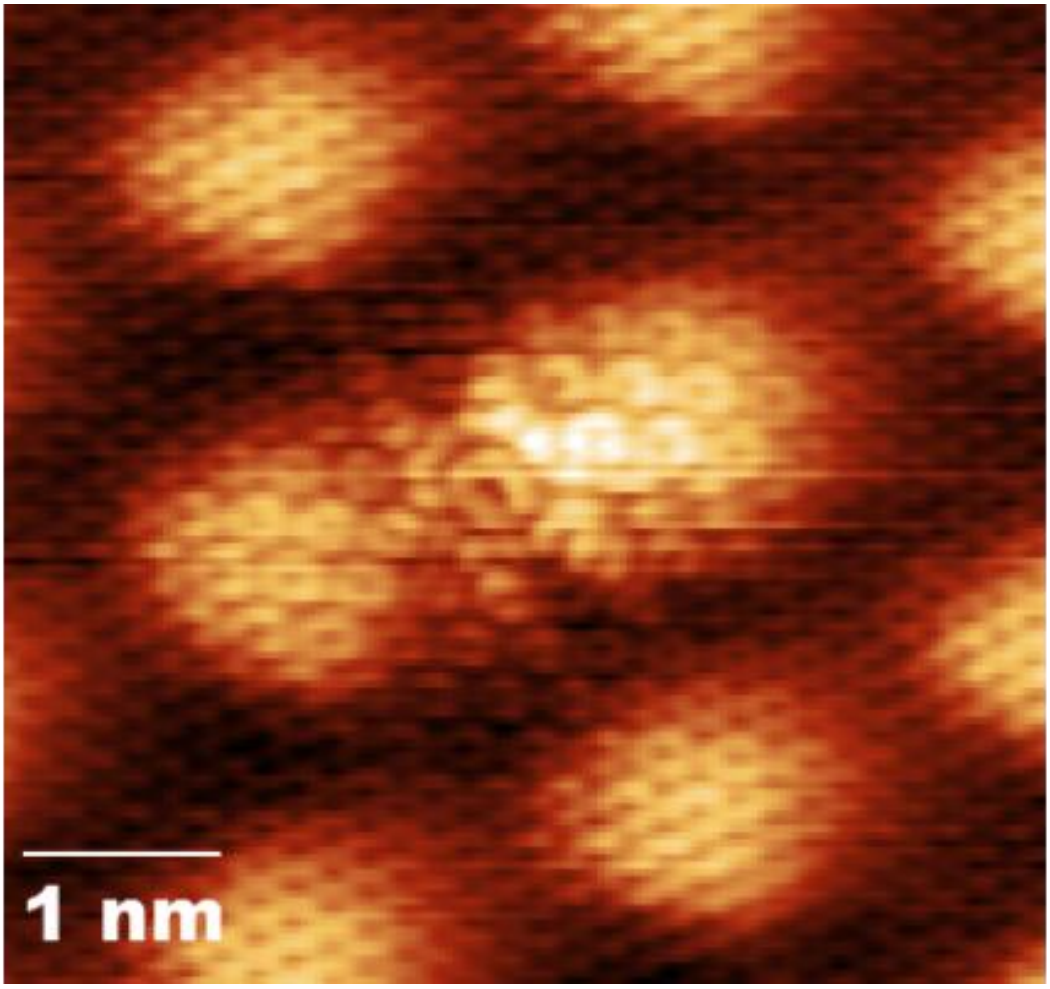

Figure 4-18 – STM topographic image of a flower defect in the graphene/Ru(0001) moiré after exposure to H_2S. The flower defect has formed in the bridge site between two hillocks, increasing the apparent height of the zone. T=4K, Vs=100mV, It=800pA.

The atomic-scale defects act as scattering centers for the electrons travelling through the two inequivalent lattices of graphene [60] [61]. In pristine graphene, backscattering of electrons is suppressed because they behave as quasiparticles with both pseudospin and chirality. On the contrary, pseudospin-flip and chirality-reversal processes can take place at zig-zag edges and atomic-scale defects, allowing backscattering processes [60]. The characteristic flower-like appearance in the STM topographic images is the consequence of a (√3x√3)R30º interference pattern appearing around them due to intervalley backscattering processes resulting from atomic defects breaking the A-B symmetry of the graphene honeycomb lattice [60]. This (√3x√3)R30º interference patterns are also observed at impurities and graphene edges and interfaces, at which the symmetry is also broken, leading to similar inter- and intravalley scattering effects [62] [63].

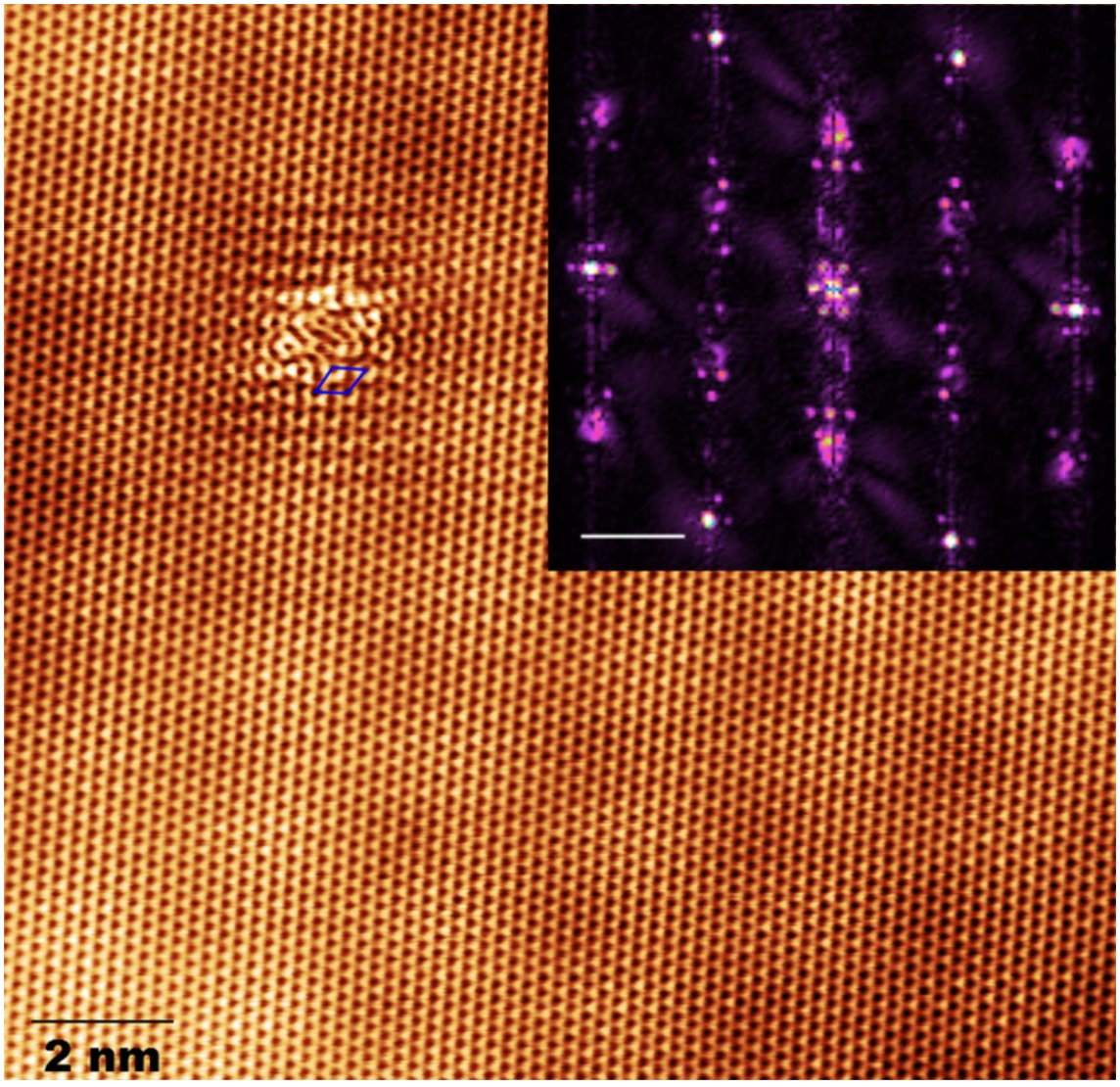

Figure 4-19 – STM topographic image taken at T=300K of sulfur-intercalated DW phase in graphene on Ru(0001). The moiré of graphene/Ru(0001) still appears at this coverage. The sulfur domain walls are manifested in the graphene honeycomb lattice as slightly brighter triangles. Around the defect it can clearly be seen a long-range ring-shaped √3 interference pattern, which is reflected in the FFT (inset) as a moon-shaped feature around the √3 spot. Inset scale-bar: 2nm^{-1}. V_s=50mV, I_t=30nA.

In the DW sulfur-intercalated graphene/S/Ru(0001) we observe the presence of flower defects and other atomic-scale features, as we do in the graphene/Ru(0001) zones after exposure to H_2S, but in this case the density of this kind of defects is higher. When imaging regions close to these topological defects, we can see the (√3x√3)R30º interference pattern attributed to intervalley scattering extending radially for many lattice vectors, even when imaging at room temperature

(Figure 4-19). 2D-FFT of regions containing one or several of this defects clearly shows the characteristic half-ring structures around the √3 spots of graphene among the graphene, sulfur, and graphene/Ru(0001)moiré spots (Figure 4-19 - inset).

STM topographic images of large areas around single point defects and their FFTs allow us to observe the characteristic signatures of intervalley scattering processes; they appear as anisotropic rings around the K_p and K_p' points in the reciprocal space. Intravalley scattering processes should appear as rings around the (0,0) spot in bilayer graphene, but this effect is suppressed in monolayer graphene due to the cancelling of the pseudospins of the two inequivalent graphene lattices [37]. Nevertheless, the replica rings of intravalley scattering around the first-order spots of graphene's lattice should appear [37]. In our experiments, we observe a faint circular feature in the FFTs of STM topographic images of wide graphene/S/Ru(0001) regions with a large concentration of point defects that we attribute to the cited replica rings of intravalley scattering processes (Figure 4-20).

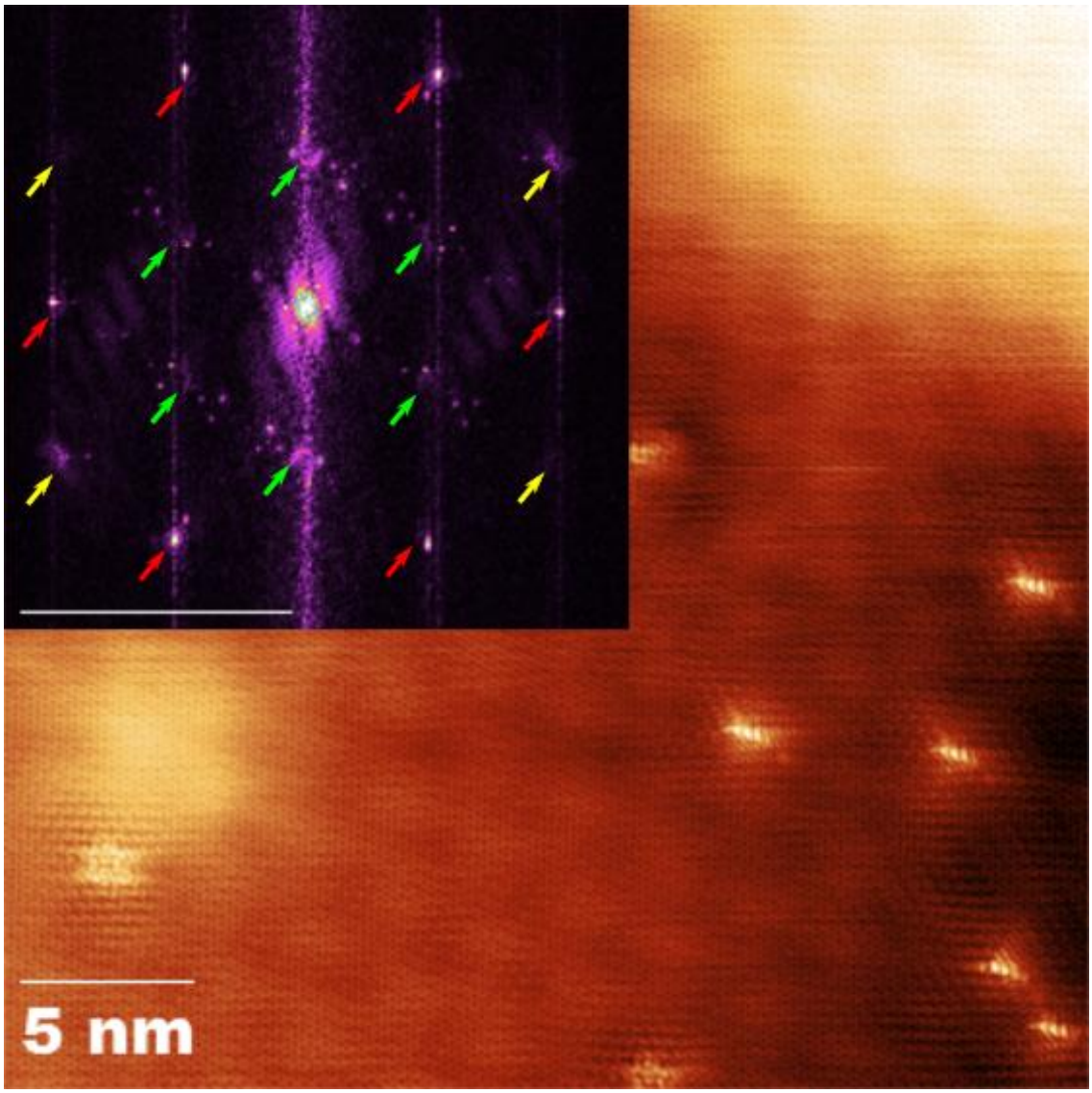

Figure 4-20 – 30x30nm^2 STM topographic image of a graphene/S/Ru(0001) with many point defects. The inset shows the central part of its FFT. The characteristic pattern of a single domain of superheavy sulfur DWs can be observed. The intravallley scattering processes show up as faint circular structures around the first-order spots of graphene (red arrows). Intervalley scattering processes appear as anisotropic rings around the K_p and K_p' points (green arrows). The yellow arrows mark the second order replicas of the intervalley rings. The diameter of both intervalley and intravalley rings in this figure is 0.5±0.1nm^{-1}. T=300K, V_s=5mV, I_t=1nA. Inset scale-bar: 5nm^{-1}.

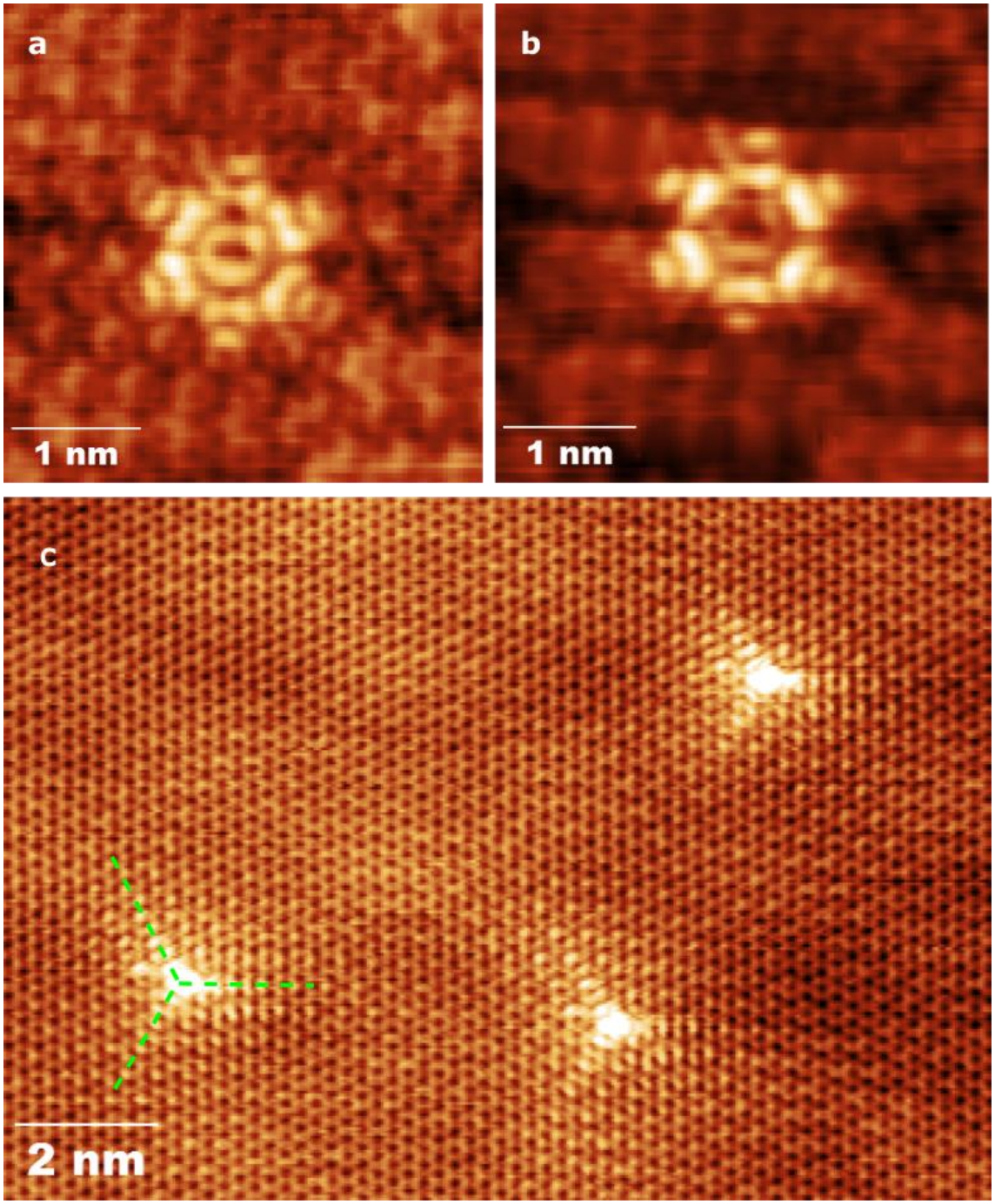

Figure 4-21 – STM topographic images of topological defects in DW-sulfur-intercalated graphene/S/Ru(0001) surface. (a) Shows a flower defect embedded in the honeycomb lattice of graphene, while (b) shows the underlying domain-wall structure of sulfur. (c)) Shows three C_3-symmetry defects with the same relative orientation. The symmetry axes of the defects are superimposed as green dashed lines and follow the moiré honeycomb lattice. (a) T=4K, V_s=1V, I_t=100pA; (b) T=4K, V_s=1.5V, I_t=100pA, (c) T=300K, V_s=-5mV, I_t=1nA.

The intensity of intervalley and intravalley scattering processes in graphene/S/Ru(0001) gives us an idea of how large the decoupling of graphene from the substrate is. In [37] they need to cool down to 4-5K in graphene/SiC in order to be able to measure this effect with a high-resolution STM, while a room temperature experiment in graphene/S/Ru(0001) can show it right away. Imaging at LHe temperature allows us to see these structures with a better resolution of the intercalated sulfur layer. The topological defects observed in DW-intercalated graphene/S/Ru(0001) are not restricted to C_6 symmetry defects, but we can also observe defect-

like structures with C_3 symmetry (Figure 4-21), and wider structures showing the alternating pentagon-heptagon structure typical of loop-gran boundaries (Figure 4-22).

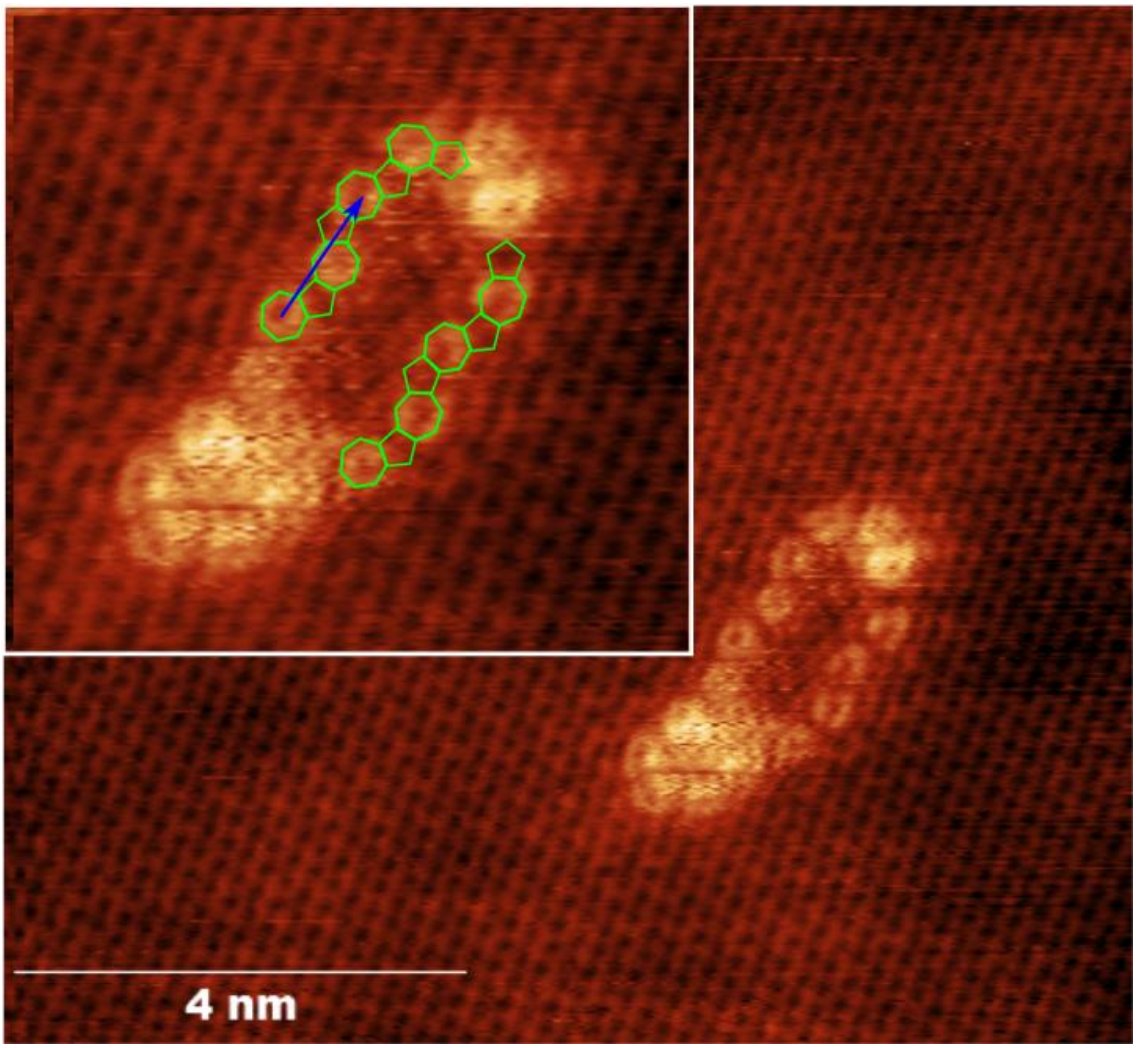

Figure 4-22 – STM topographic image of a DW-intercalated graphene/S/Ru(0001) surface showing a ~4nm long topological defect.The inset shows a zoom in on the defect showing the combination of heptagonal and pentagonal dislocations that result in the loop grain boundary. The distance between equivalent dislocations (blue arrow) is ~8.5Å, and it forms an angle of 15° with the main symmetry direction of graphene's honeycomb. T=300K, V_s=2V, I_t=8nA.

Long defects as the one shown in (Figure 4-22) show a zig-zag structure at its edges that can be attributed to a loop grain-boundary consisting on alternating carbon pentagons and heptagons. They resemble the type II large-angle grain boundaries (LAGB II) described in [55], and the measured angles and distances between dislocations (8.5Å) coincide with theory (8.8Å) within experimental error.

4.6 CONDUCTANCE RESONANCES IN GRAPHENE/S/RU(0001) AND GRAPHENE/RU(0001) AFTER EXPOSURE TO H_2S

In order to complete the description of graphene/S/Ru(0001) we performed STS experiments of the different intercalation regimes we observe, namely graphene/Ru(0001), DW-intercalated graphene/Ru(0001) and c(2x4)-intercalated graphene/Ru(0001). These experiments give us the conductance at different points of the surface which, as we explained in Chapter 2, is proportional to its LDOS.

The spectrum of as-grown graphene/Ru(0001) was studied in [18] and is characterized by the large n-doping of graphene by ruthenium, which downshifts the Fermi energy by 1eV to 2eV. In the case of graphene/S/Ru(0001), since graphene seems less coupled to the substrate, we would expect a behavior similar to that of weakly-coupled systems such as graphene/Ir(111) or graphene/SiC, i.e. a less-doped graphene at which the Dirac cone is recovered.

In the STS experiments carried on in graphene/S/Ru(0001) and graphene/Ru(0001) after exposure to H_2S we observe the appearance of a series of sharp resonances with a constant energy separation in the range of -2eV to 2eV around the Fermi level. These sharp peaks appear in both intercalation regimes in graphene/S/Ru(0001) and also in the non-intercalated graphene/Ru(0001) regions.

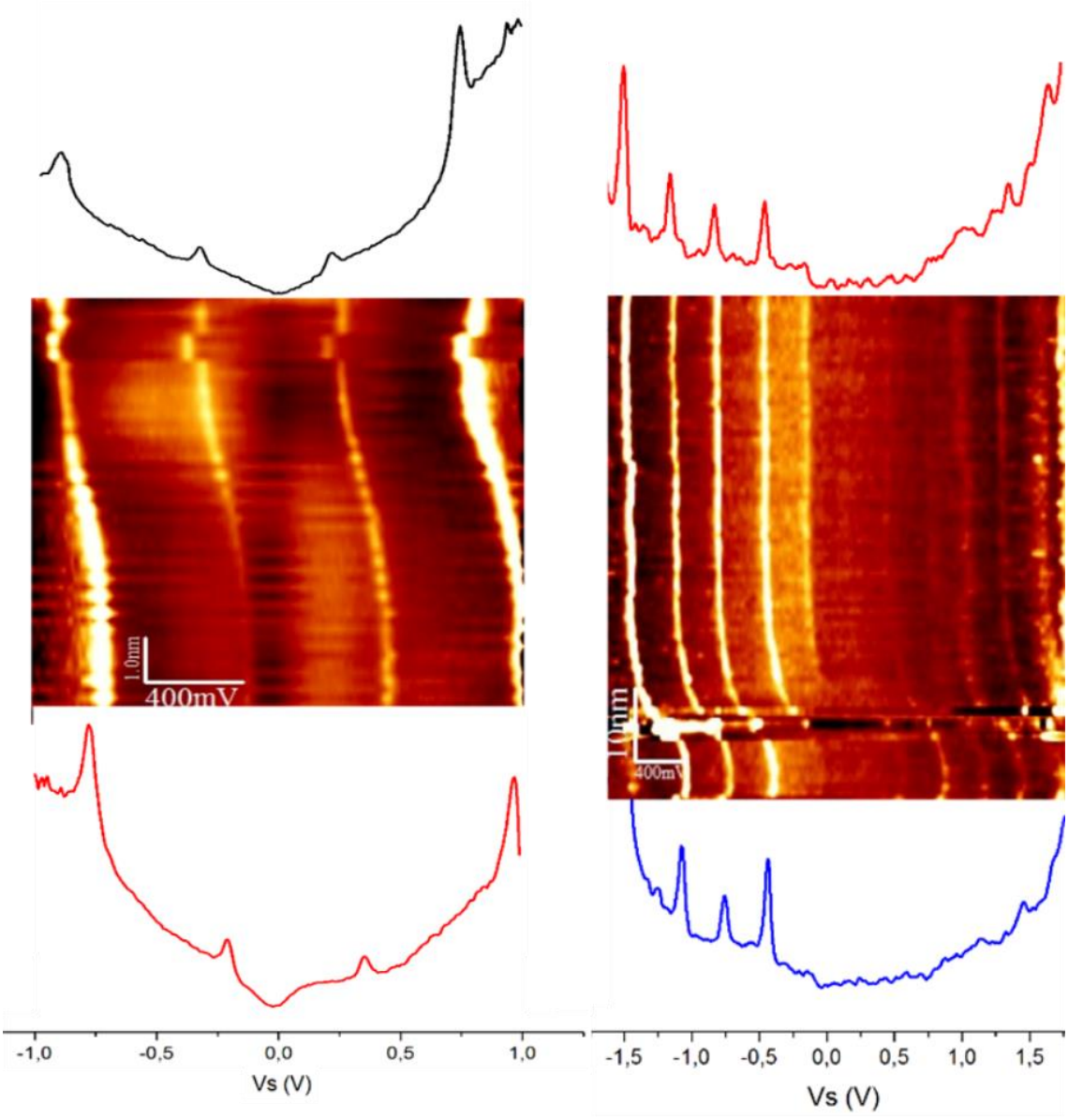

Figure 4-23 – (a) Evolution of the peak energy in graphene/S/Ru(0001) when moving from a graphene/Ru(0001) region (up, black line) to a DW-intercalated graphene/S/Ru(0001) region (down, red line). T=4K. (b) Evolution of each of the peaks at the interface of a DW-intercalated (up, red line) and a c(2x4)-intercalated area (down, blue line) in graphene/S/Ru(0001). Both panels clearly show the continuous shift in energy, while the energy difference between peaks is kept constant. All the spectra used to make this figure were taken at T=4K.

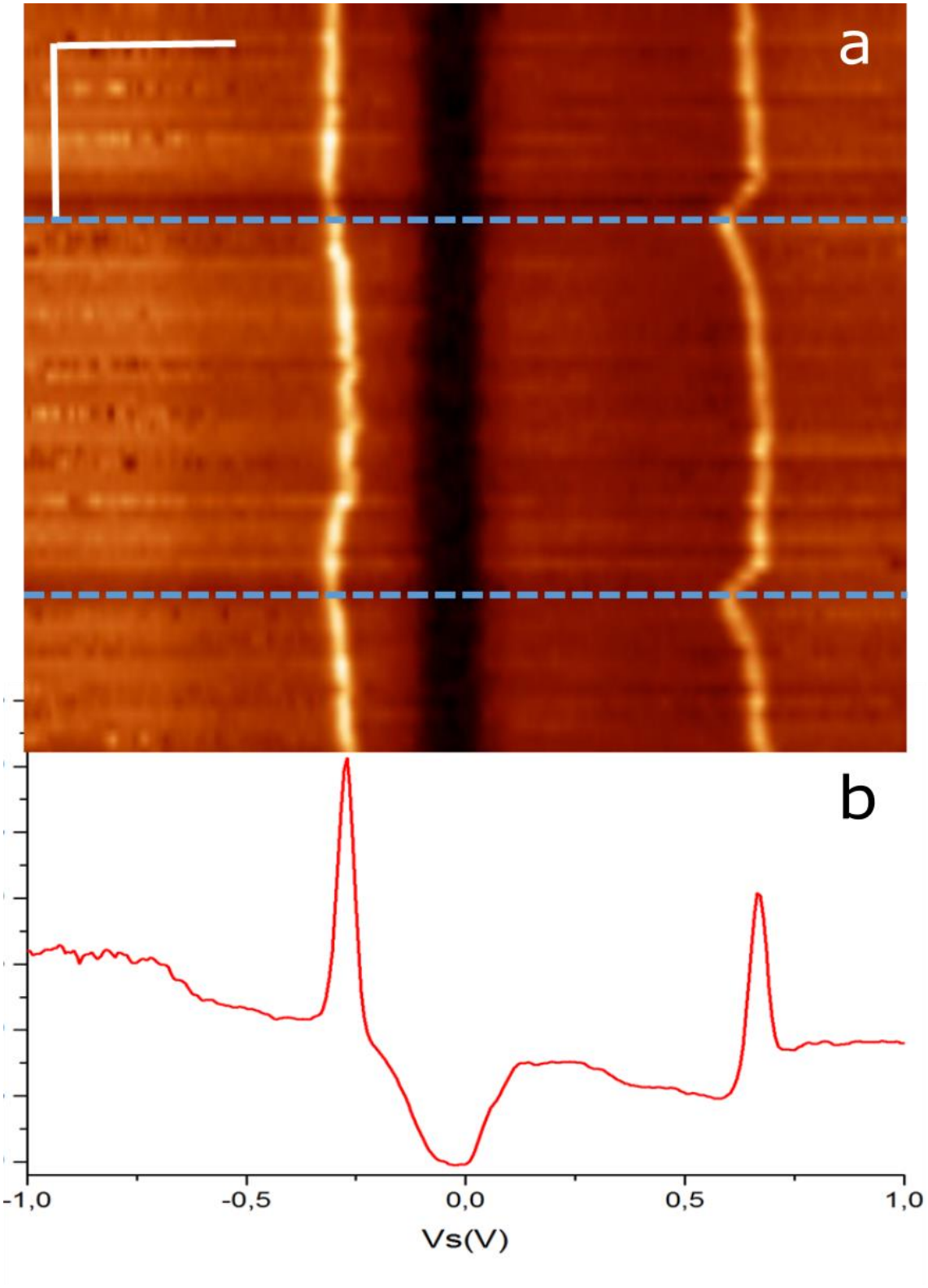

Figure 4-24 – (a) Stack of dI/dV spectra extracted from a CITS experiment. The vertical axis represents distance (scale bar: 2.7nm) and the horizontal sample voltage (scale bar 400mV; the color reflects the intensity of dI/dI, brighter meaning more intense). The tip crosses two steps (blue dashed lines) of three different DW-intercalated terraces. The resonances show a bright contrast and are only slightly perturbed at the step edges, while the gap appears as a dark band crossing the whole profile. (b) dI/dV spectrum extracted from the last line of (a). The two sharp resonances and a gap (~150mV at FWHM) can be observed.

The STS experiments showing sharp peaks are usually accompanied by the emergence of a symmetric gap-like feature of ~150meV around the Fermi level (Figure 4-23a, Figure 4-24),

which has been observed many times in different graphene systems and it is usually attributed in literature to inelastic scattering processes, most likely out of plane phonons at the K/K' points of graphene [64] [65] [66], but it has also been suggested to be related to the coulomb gap characteristic of two dimensional systems [67].

The energy difference between peaks changes from experiment to experiment from 200meV to almost 1eV. CITS maps shows that this energy difference remains constant when changing zones, but all the peaks are shifted to higher energies with increasing sulfur coverage. We attribute this effect to the change in charge density at each region, from a strongly n-doped graphene in graphene/Ru(0001) areas to slightly n-doped graphene in c(2x4) intercalated areas. Our experiments show that the overall energy shift when moving from a graphene/Ru(0001) area to a c(2x4)-intercalated graphene/S/Ru(0001) area is close to 1.25eV Figure 4-25. The Fermi level of graphene/Ru(0001) compared to graphite is shifted down in energy by 1.8eV [19], so we can estimate that c(2x4) graphene/S/Ru(0001) is n-doped and the bands are shifted at most by 0.55eV when compared to graphite.

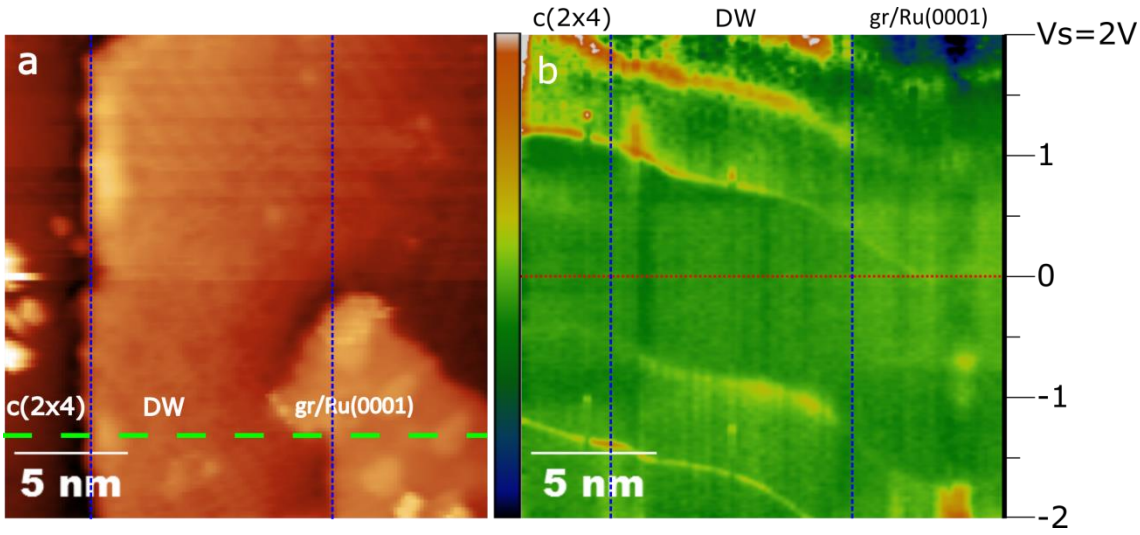

Figure 4-25 – (a) STM topography image of a graphene/S/Ru(0001) surface showing c(2x4)- and DW-intercalated graphene/S/Ru(0001), and a non-intercalated graphene/Ru(0001) island. T=4K, V_s=2V, I_t=100pA. In this zone we took a CITS map, a profile of which across the green-dashed line is shown in (b). (b) Profile of the CITS covering the three different zones. The horizontal axis represents the position in the sample and the vertical axis the sample voltage for each spectrum of the CITS experiment. The red-dotted line shows the position of the Fermi energy, and the two vertical lines represent the interface between the different domains. The pseudo-Landau-levels decrease in energy when moving to less-intercalated areas, but maintain the peak-to-peak distance of ~690meV. The shift is larger when moving from DW to graphene/Ru(0001) than when moving from c(2x4) to DW.

Different experimental and theoretical works observe or predict a quantized structure of the LDOS of graphene close to the Fermi energy in different graphitic systems. Some of these works relate the sharp peaks to pseudo-Landau levels appearing due to pseudo-magnetic fields of different possible origins. Evidences of pseudo-magnetic fields as big as 300T showing the pseudo-Landau levels around the Fermi level have been reported in many different systems such as strained graphene on platinum [68], near the intercalation edges in potassium-intecalated graphite [69], graphene ridges on highly-oriented pyrolytic graphite (HOPG) [70], graphene ripples on rhodium [71], twisted graphene bilayers [72], periodic graphene ripples on SiO_2/Si [73], graphene nano-bubbles in oxygen-intercalated graphene on ruthenium [74], and lead-intercalated graphene on iridium [75].

These works reporting sharp features in their tunneling spectroscopy experiments have many differences in their overall appearance, but their behavior is very similar. The substrates are different for all the cited papers. Some of them require intercalation while others rely on external mechanical strain. While most consider graphene monolayers, some observe this effect on rotated graphene bilayers and even on intercalated HOPG. But all of them share a sharp peak family around the Fermi energy, with the energy separation between peaks within the same range of values (few hundreds of meV). In most cases, the peaks appear in specific region which are mechanically strained or curved, as in the case of nanobubbles, wrinkles and ridges. Some are located near the interfaces between rotational or stacking domains, which are extended defects in the graphene lattice. In the case of the intercalated systems (K-intercalated HOPG and Pb/Ir(111)), similar peaks appear both in the intercalated islands and in the non-intercalated regions, experiencing a continuous energy shift in the interface region, just as in our case [69] [75].

Since graphene's band structure presents a linear behavior close to the Fermi energy, the electrons should behave as massless Dirac fermions and their distribution in energy when subjected to a large magnetic field should be proportional to $\sqrt{n}$, following the equation $E_n = E_D + sgn(n)v_F\sqrt{2e\hbar B_S|n|}$, with $n = 0, \pm1, \pm2, ...$ the Landau index, v_F the Fermi velocity and B_S the effective magnetic field. Our data does not follow that relation and fits pretty well to a linear distribution (Figure 4-26). In our case the spectroscopic data shows resonances are separated by a constant energy difference, i.e. $E_n \propto n$.

An almost linear behavior is expected for massive chiral fermions, and it has been observed in bilayer graphene in [72] and explained in terms of strain and curvature. According to a tight-binding model, applying strain to the graphene lattice should move the Dirac points of both sublattices away from K and K^0. When inserting curvature into the calculations, a band gap is opened in the graphene band structure and, combined with the strain effect, can lead to the merging of the Dirac points in K and K^0 into a single one, what corresponds to the dispersion relation of the massive chiral fermions in Bernal stacked graphene bilayer. These considerations, along with the pseudo-magnetic field generated by a non-uniform distortion of the graphene lattice explain the appearance of Landau-like levels.

The dispersion relation of massive chiral fermions, e.g. in a graphene bilayer, has the form $E_N = \pm\hbar\omega_c(n(n-1))^{1/2} + E_g/2$, which is nearly linear and fits well our experimental data (Figure 4-26). The most strained regions in our sample have a strain of 0.08% at most, which is moderate but it is in the range considered in the cited work (0-0.12%). The curvature of graphene in our system are far too small compared to the expected values in order to open a band gap wide enough to observe this effect. In our case the most curved region is the moiré in graphene/Ru(0001) and we can consider it almost flat, since the difference between the high and the low areas is 1Å, while in the calculations an experimental value of 1.4nm is used, and the observed gap is of 0.36eV. Nevertheless in some of our STS experiments we observe a gap-like feature around the Fermi level of ~120meV (Figure 4-24 – (a) Stack of dI/dV spectra extracted from a CITS experiment. The vertical axis represents distance (scale bar: 2.7nm) and the horizontal sample voltage (scale bar 400mV; the color reflects the intensity of dI/dI, brighter meaning more intense). The tip crosses two steps (blue dashed lines) of three different DW-intercalated terraces. The resonances show a bright contrast and are only slightly perturbed at the step edges, while the gap appears as a dark band crossing the whole profile. (b) dI/dV spectrum extracted from the last line of (a). The two sharp resonances and a gap (~150mV at FWHM) can be observed. The existence of such a gap, regardless of its origin, together with the displacement of the Dirac points induced by the strain, could explain the pseudo-Landau level structure in our spectra.

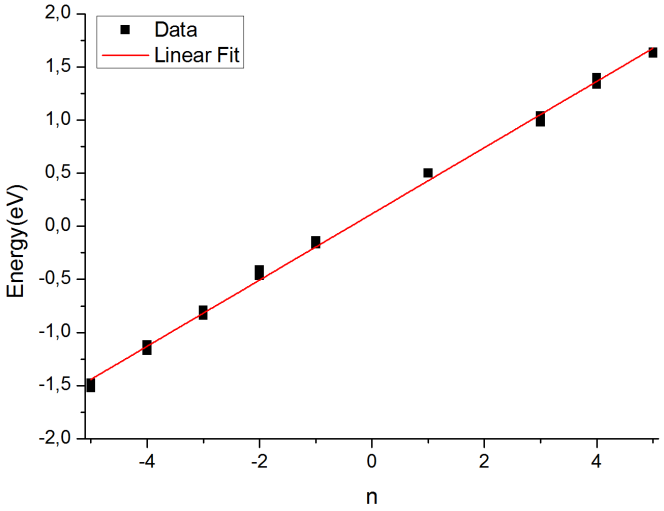

Figure 4-26 – Linear fit of the peak energies of the Landau-like levels as a function of the Landau index. The data was taken from eight different spectra in the domain-wall intercalated region. The fit has a Pearson's R of 0.999.

A similar distribution of peaks, i.e., following the dispersion relation of massive chiral fermions, is found again in bilayer graphene on SiO_2/Si. In [76] it is suggested that the band gap, which is determined by the local potential difference between the two graphene layers, is not determined by the external applied field as suggested in [77] and [78], but it is related to the disorder potential, which in this case is dictated by the surface roughness of the SiO_2 substrate. The substrate imperfections lead to the formation of electron- and hole-rich zones, leading to an irregular charge distribution in the graphene plane. Both the size of the gap and the position of the peaks evolve depending on the lateral position of the STM tip, shifting from lower to higher energies when the tip changes from "electron puddles" to "hole puddles".

Periodic potentials can also give rise to sharp resonances in the conductance spectra. In [79], one-dimensional electric potentials applied to a graphene single-layer results in the emergence of sharp resonances in the LDOS of graphene. The energy distribution of these resonances should follow a J0 Bessel function, which is almost equispaced for all n-(n+1) pairs except around zero, with the distance between n=-1 and n=1 being larger than the rest. The sulfur intercalated phases in graphene/S/Ru(0001) both break the hexagonal symmetry of graphene, and they can be modelled as periodic potentials with one preferential direction, what could explain the appearance of the STS resonances. Nevertheless, we also observe them in graphene/Ru(0001) after exposure to H_2S, which does not present a one-dimensional modulation of the electric potential.

Another possible explanation for an evenly spaced peak structure could be the existence of quantum confinement in certain regions of the graphene layer. Quantum dots in graphene should result in sharp resonances in the LDOS of graphene [80] [81] that can be observed in transport and STS experiments. Carriers in graphene are not easily confined, since they can tunnel through potential barriers due to the Klein paradox [82]. Nevertheless, we observe the characteristic interference pattern of inter- and intravalley backscattering processes close to two different features of our samples: around loop-grain boundaries (see Section 4.5) and near the edges of zones with different intercalated S coverage (e.g. Figure 4-14, Figure 4-16). It is possible that these scattering centers can produce zones where electrons can be confined. The river-like c(2x4) domains have well-defined widths determined by the moiré unit cell that usually span from 3nm to 15nm, sizes comparable to the quantum dots measured in [80]. On the other hand, we observe loop grain boundaries, like the flower defects and larger structures, with lateral dimensions of a few nanometers, which could behave like quantum corrals [83] or quantum dots [84] with a non-vanishing transmission coefficient. This kind of structures could also result in quasi-bound states directly observable by STS as conductance resonances [85].

With our present experimental data, we cannot assert the exact origin of the resonances we observe in the LDOS of graphene/S/Ru(0001) and graphene/Ru(0001), and we are limited to a phenomenological description of our data. It shows a family of evenly spaced resonances with energy differences ranging from 200meV to 700meV that keep their energy difference when moving from and to regions with different sulfur coverage, and shift their energies to higher energies when moving to zones with a higher sulfur density. The linear relation of the energy levels inclines us to discard a magnetic or pseudo-magnetic origin for these resonances. The DW and c(2x4) sulfur reconstructions should induce a periodic electrostatic potential that could give rise to these peaks, but if this was the case we would expect a different energy separation when moving from one reconstruction to the other, which is not the case. The quantum confinement argument can take account of the resonances we observe if we assume that the confinement potential is semi-transparent for the electrons so we can observe the resonances outside the confinement regions.

4.7 CONCLUSIONS

- Exposure to H2S of graphene/S/Ru(0001) leads to sulfur intercalation between graphene and ruthenium, and the intercalated layer organizes in the domain-wall phase and the c(2x4) phase. There is no evidence of the formation of the low-coverage hexagonal phases observed in S/Ru(0001). The boundaries between graphene/Ru(0001) and DW-intercalated graphene/S/Ru(0001) are long and follow the high symmetry directions of the moiré lattice, resulting in wide graphene/S/Ru(0001) areas; c(2x4)-intercalated graphene/S/Ru(0001) forms in elongated domains up to 15nm wide and hundreds of nanometers long.

- Graphene/S/Ru(0001) still shows a moiré pattern resulting from the interaction of graphene with the ruthenium substrate, even with the intercalated sulfur layer between them. This moiré has the same lateral dimensions as the one appearing in graphene/Ru(0001), but its apparent height is one order of magnitude smaller.

- Formation of atomic-scale defects and the observation of long-range backscattering of electrons indicates that dislocations and grain boundaries can be formed in the graphene lattice, and that graphene is fairly decoupled from the substrate after sulfur intercalation.

- Scanning tunneling spectroscopy shows the emergence of a series of equispaced sharp peaks in all the studied regions, that shift to higher energies with increasing sulfur density.

4.8 REFERENCES

[1] A. Castro Neto, F. Guinea, N. Peres, K. Novoselov and A. Geim, "The electronic properties of graphene," *Review of Modern Physics,* vol. 81, pp. 109-161, 2009.

[2] K. Novoselov, A. Geim, S. Morozov, D. Jiang, M. Katsnelson, I. Grrigorieva, S. Dubonos and A. Firsov, "Two-dimensional gas of massless Dirac fermions in graphene," *Nature,* vol. 438, pp. 197-200, 2005.

[3] G. Giovannetti, P. Khomyakov, G. V¡Brocks, P. Kelly and J. van den Brink, "Substrate-induced band gap in graphene on hexagonal boron nitride: Ab initio density functional calculations," *Physical Review B,* vol. 2007, p. 073103, 2007.

[4] S. Zhou, G.-H. Gweon, A. Fedorov, P. First, W. de Heer, D.-H. Lee, F. Guinea, A. Castro Neto and A. Lanzara, "Substrate-induced bandgap opening in epitaxial graphene," *Nature Materials*, vol. 6, pp. 770-775, 2007.

[5] Y. Shi, X. Dong, P. Chen, J. Wang and L.-J. Li, "Effective doping of single-layer graphene from underliying SiO2 substrates," *Physical Review B*, vol. 79, p. 115402, 2009.

[6] X. Dong, D. Fu, W. Fang, Y. Shi, P. Chen and L.-J. Li, "Doping single-layer graphene with aromatic molecules," *Small*, vol. 5, pp. 1422-1426, 2009.

[7] T. Mueller, F. Xia and P. Avouris, "Graphene photodetectors for high-speed optical communications," *Nature Photonics*, vol. 4, pp. 297-301, 2010.

[8] F. Himpsel, K. Christmann, P. Heimann, E. D.E. and P. Feibelman, "Adsorbate band dispersions for C on Ru(0001)," *Surface Science Letters*, vol. 115, no. 59, pp. L159-L164, 1982.

[9] T. Land, T. Michely, R. Behm, J. Hemminger and G. Comsa, "Direct observation of surface reactions by scanning tunneling microscopy: Ethylene - ethylidyne - carbon particles - graphite on Pt (111)," *Journal of Chemical Physics*, vol. 97, pp. 6774-6783, 1992.

[10] C. Oshima and A. Nagashima, "Ultra-thin epitaxial films of graphite and hexagonal boron nitride on solid surfaces," *Journal of Physics: Condensed Matter*, vol. 9, pp. 1-20, 1997.

[11] S. Hagstrom, H. Lyon and G. Somorjai, "Surface structures on the clean platinum (100) surface," *Physical Review Letters*, vol. 15, no. 11, pp. 491-493, 1965.

[12] J. Grant and T. Haas, "A study of Ru(0001) and Rh(111) surfaces using LEED and Auger electron spectroscopy," *Surface Science*, vol. 21, no. 1, pp. 76-85, 1970.

[13] A. Karu and M. Beer, "Pyrolytic formation of highly crystalline graphite films," *Journal of Applied Physics*, vol. 37, pp. 2179-2181, 1966.

[14] D. Martoccia, P. Willmott, T. Brugger, M. Björck, S. Günther, C. Shelpütz, A. Cervellino, S. Pauli, B. Patterson, S. Marchini, J. Wintterlin, W. Moritz and T. Greber, "Graphene on Ru(0001): A 25x25 supercell," *Physical Review Letters*, vol. 101, p. 126102, 2008.

[15] D. Martoccia, M. Björck, M. Schlepütz, T. Brugger, S. Pauli, B. Patterson, T. Greber and P. Willmott, "Graphene on Ru(0001): a corrugated and chiral structure," *New Journal of Physics*, vol. 12, p. 043028, 2010.

[16] A. Preobrajenski, M. L. Ng, A. Vinogradov and N. Mårtensson, "Controlling graphene corrugation on lattice-mismatched substrates," *Physical Review B*, vol. 78, p. 073401, 2008.

[17] W. Moritz, B. Wang, M.-L. Bocquet, T. Brugger, T. Greber, J. Wintterlin and S. Günther, "Structural determination of the coincidence phase of graphene on Ru(0001)," *Physical Review Letters,* vol. 104, p. 136102, 2010.

[18] S. Marchini, S. Günther and J. Wintterlin, "Scanning tunneling microscopy of graphene on Ru(0001)," *Physical Review B,* vol. 76, p. 075429, 2007.

[19] A. Vázquez de Parga, F. Calleja, B. Borca, M. Passeggi Jr., J. Hinarejos, F. Guinea and R. Miranda, "Periodically rippled graphene: Growth and spatially resolved electronic structure," *Physical Review Letters,* vol. 100, p. 056807, 2008.

[20] B. Borca, S. Barja, M. Garnica, D. Sánchez-Portal, V. Silkin, E. Chulkov, F. Hermanns, J. Hinarejos, A. Vázquez de Parga, A. Arnau, P. Echenique and R. Miranda, "Potential energy landscape for hot electrons in periodically nanostructured graphene," *Physical Review Letters,* vol. 105, p. 036804, 2010.

[21] S. Barja, Grafeno epitaxial en metales de transición: Estudio mediante microscopía y espectroscopia de efecto túnel, Madrid: PhD Thesis, Universidad Autónoma de Madrid, 2012.

[22] A. N'Diaye, J. Coraux, T. Plasa, C. Busse and M. T., "Structure of epitaxial graphene on Ir(111)," *New Journal of Physics,* vol. 10, p. 043033, 2008.

[23] J. Coraux, A. N'Diaye, C. Busse and T. Michely, "Structural coherency of graphene on Ir(111)," *Nano Letters,* vol. 8, p. 565, 2008.

[24] E. Loginova, S. Nie, K. Thürmer, N. Bartelt and K. McCarty, "Defects of graphene on Ir(111): Rotational domains and ridges," *Physical Review B,* vol. 80, p. 085430, 2009.

[25] I. Pletikosic, M. Kralj, P. Pervan, R. Brako, J. Coraux, A. N'Diaye, C. Busse and T. Michely, "Dirac Cones and Minigaps for Graphene on Ir(111)," *Physical Review Letters,* vol. 102, p. 056808, 2009.

[26] M. Garnica Alonso, Electon acceptor molecules deposited on epitaxial graphene studied by means of low temmperature scanning tunneling microscopy/spectroscopy, Madrid: PhD Thesis, Universidad Autónoma de Madrid, 2013.

[27] A. Tsen, L. Brown, M. Levendorf, F. Ghahari, P. Huang, R. Havener, C. Ruiz-Vargas, D. Muller, P. Kim and J. Park, "Tailoring electrical transport across grain boundaries in polycrystalline graphene," *Science,* vol. 336, no. 6085, pp. 1143-1146, 2012.

[28] P. Sutter, J. Sadowski and E. Sutter, "Chemistry under cover: Tuning metal-graphene interaction by reactive intercalation," *Journal of the American Chemical Society,* vol. 132, pp. 8175-8179, 2010.

[29] Y. Cui, J. Gao, L. Jin, J. Zhao, D. Tan, Q. Fu and X. Bao, "An exchange intercalation mechanism for the formation of a two-dimensional Si structure underneath graphene," *Nano Research,* vol. 5, no. 5, pp. 352-350, 2012.

[30] L. Jin, Q. Fu, Y. Yang and X. Bao, "A comparative study of intercalation mechanism at graphene/Ru(0001) interface," *Surface Science,* vol. 617, pp. 81-86, 2013.

[31] C. Enderlein, Y. Kim, A. Bostwick, E. Rotenberg and K. Horn, "The formation of an energy gap in graphene on ruthenium by controlling the interface," *New Journal of Physics,* vol. 12, p. 033014, 2010.

[32] Z. Zhou, B. Habenicht, Q. Guo, Z. Yan, Y. Xu, L. Liu and D. Goodman, "Graphene moiré structure grown on a pseudomorphic metal overlayer supported on Ru(0001)," *Surface Science,* vol. 611, pp. 67-73, 2013.

[33] L. Jin, Q. Fu, R. Mu, D. Tan and X. Bao, "Pb intercalation underneath a graphene layer on Ru(0001) and its effect on graphene oxidation," *Physical Chemistry Chemical Physics,* vol. 13, pp. 16655-16660, 2011.

[34] L. Huang, Y. Pan, L. Pan, M. Gao, W. Xu, Y. Que, H. Zhou, Y. Wang, S. Du and H.-J. Gao, "Intercalation of metal islands and films at the interface of epitaxialy grown graphene and Ru(0001) surfaces," *Applied Physics Letters,* vol. 99, p. 163107, 2011.

[35] J. Mao, L. Huang, Y. Pan, M. Gao, J. He, H. Zhou, H. Guo, Y. Tian, Q. Zou, L. Zhang, H. Zhang, Y. Wang, S. Du, X. Zhou, A. Castro Neto and H.-J. Gao, "Silicon layer intercalation of centimeter-scale, epitaxially grown monolayer graphene on Ru(0001)," *Applied Physics Letters,* vol. 100, p. 093101, 2012.

[36] L. Huang, W.-Y. Xu, Y.-D.-. Que, J.-H. Mao, L. Meng, L.-D. Pan, G. Li, Y.-L. Wang, S.-X. Du, Y.-Q. Liu and H.-Y. Gao, "Intercalation of metals and silicon at the interface of epitaxial graphene and its substrates," *Chinese Physics B,* vol. 2, no. 9, p. 096803, 2013.

[37] P. Mallet, I. Brihuega, S. Bose, M. Ugeda, J. Gómez-Rodríguez, K. Kern and J. Veullien, "Role of pseudospin in quasiparticle interferences in epitaxial graphene, probed by high resolution tunneling microscopy," *Physical Review B,* vol. 86, p. 045444, 2012.

[38] M. Ugeda, D. Fernández-Torre, I. Brihuega, P. Pou, A. Martínez-Galera, R. Pérez and J. Gómez-Rodríguez, "Point defects on graphene on metals," *Physical Review Letters,* vol. 107, p. 116803, 2011.

[39] F. Calleja, Influencia de la estructura electrónica local en las propiedades de las superficies y su estudio mediante microscopía de efecto túnel, Madrid: PhD. Thesis, Universidad Autónoma de Madrid, 2007.

[40] V. Brar, Y. Zhang, Y. Yayon, T. Ohta, J. McChesney, A. Bostwick, E. Rotenberg, K. Horn and M. Crommie, "Scanning tunneling spectroscopy of inhomogeneus electronic structures in monolayer and bilayer graphene on SiC," *Applied Physics Letters,* vol. 91, p. 122102, 2007.

[41] G. Rutter, N. Guisinguer, J. Crain, E. Jarvis, M. Stiles, T. Li, P. First and J. Stroscio, "Imaging the interface of epitaxial graphene with silicon carbide via scanning tunneling microsccopy," *Physical Review B,* vol. 76, p. 235416, 2007.

[42] C. Riedl, U. Starke, J. Bernhardt, M. Franke and K. Heinz, "Structural properties of the graphene-SiC(0001) interface as a key for the preparation of homogeneous large-terrace graphene surfaces," *Physical Review B,* vol. 76, p. 245406, 2007.

[43] F. Hiebel, P. Mallet, F. Varchon, L. Magaud and J.-Y. Veuillen, "Graphene-substrate interaction on 6H-SiC(0001): A scanning tunneling microscopy study," *Physical Review B,* vol. 78, p. 153412, 2008.

[44] F. Hiebel, P. Mallet, L. Magaud and J.-Y. Veuillen, "Atomic and electronic structure of monolayer graphene on 6H-SiC(0001)(3x3): A scanning tunneling microscopy study," *Physical Review B,* vol. 80, p. 235429, 2009.

[45] E. Grånäs, M. Andersen, M. A. Arman, T. Gerber, B. Hammer, J. Schnadt, J. N. Andersen, T. Michely and J. Knudsen, "CO intercalation of graphene on Ir(111) in the millibar regime," *The Journal of Physical Chemistry C,* vol. 117, pp. 16438-16447, 2013.

[46] M. Andersen, L. Hornekær and B. Hammer, "Understanding intercalation structures formed under graphene on Ir(111)," *Physical Review B,* vol. 90, no. 15, p. 15428(9), 2014.

[47] J. Villain, "Effect of substrate defects on commmensurate-incommensurate transitions of adsorbed layers," *Journal de Physique Lettres,* vol. 41, pp. 267-270, 1980.

[48] T. Müller, D. Heuer, H. Pfnur and U. Khöler, "Domain walls and adsorbate-step interactions: an STM study of sulfur layers on Ru(0001)," *Surface Science,* no. 347, pp. 80-96, 1995.

[49] J. Villain, "Theories of commensurate-incommensurate transitions on surfaces," in *Ordering in two dimensions,* S. K. Sinha, Ed., New York, North Holland, 1980, pp. 123-129.

[50] S. Coppersmith, D. Fisher, B. Halperin, P. Lee and W. Brinkman, "Dislocations and the commensurate-incommensurate transition in two dimensions," *Physical Review B,* vol. 25, no. 1, pp. 349-363, 1982.

[51] H. Park, E. Riedel and M. den Nujs, "Anisotropic honeycomb domain wall networks in uniaxial systems," *Annals of Physics,* vol. 172, pp. 419-450, 1986.

[52] E. Cockayne, G. Rutter, N. Guisinger, J. Crain, P. First and J. Stroscio, "Grain boundary loops in graphene," *Physical Review B,* vol. 83, p. 195425, 2011.

[53] S. Kurasch, J. Kotaloski, O. Lehtinen, V. Skálaková, J. Smet, C. Krill, A. Krasheninnikov and U. Kaiser, "Atom-by-atom observation of grain boundary migration in graphene," *Nano Letters,* vol. 12, pp. 3168-3173, 2012.

[54] I. Ovid'ko, "Review on grain boundaries in graphene: curved poly- and nanocrystalline graphene structures as new carbon allotropes," *Reviews on Advanced Material Science,* vol. 30, pp. 201-224, 2012.

[55] O. Yazyev and S. Louie, "Topological defects in graphene: Dislocations and grain boundaries," *Physical Review B,* vol. 81, p. 195420, 2010.

[56] T.-H. Liu, G. Gajewski, C.-W. Pao and C.-C. Chiang, "Structure, energy, and structural transformations of graphene grain boundaries from atomistic simulations," *Carbon,* vol. 49, pp. 2306-2317, 2011.

[57] D. Alfonso, "First-principles studies of H_2S adsorption and dissociation on metal surfaces," *Surface Science,* vol. 602, pp. 2758-2768, 2008.

[58] D. Alfonso, "Computational studies of experimentally observed structures of sulfur on metal surfaces," *The Journal of Physical Chemistry C,* vol. 115, pp. 17077-17091, 2011.

[59] N. Peres, F. Guinea and A. Castro Neto, "Electronic properties of disordered two-dimensional carbon," *Physical Review B,* vol. 73, p. 125411, 2006.

[60] G. Rutter, J. Crain, N. Guisinguer, T. Li, P. First and J. Stroscio, "Scattering and interference in epitaxial graphene," *Science,* vol. 317, pp. 219-222, 2007.

[61] H. Yan, C.-C. Liu, K.-K. Bai, X. Wang, M. Liu, W. Yan, L. Meng, Y. Zhang, Z. Liu, R.-f. Dou, J.-C. Nie, Y. Yao and L. He, "Electronic structures of graphene layers on a metal foil: The effect of atomic-scale defects," *Applied Physics Letters,* vol. 103, p. 143120, 2013.

[62] I. Brihuega, P. Mallet, C. Bena, S. Bose, C. Michaelis, L. Vitali, F. Varchon, L. Magaud, K. Kern and J. Veuillen, "Quasiparticle chirality in epitaxial graphene probed at the nanometer scale," *Physical Review Letters,* vol. 101, p. 206802, 2008.

[63] H. Yang, A. Mayne, M. Boucherit, G. Comtet, G. Dujardin and Y. Kuk, "Quantum interference channeling at graphene edges," *Nano Letters,* vol. 10, pp. 943-947, 2010.

[64] T. Wehling, I. Grigorenko, A. Lichtenstein and A. Balatsky, "Phonon-mediated tunneling into graphene," *Physical Review Letters,* vol. 101, p. 216803(4), 2008.

[65] Y. Zhang, V. Brar, F. Wang, C. Girit, Y. Yayon, M. Panlasigui, A. Zettl and M. Crommie, "Giant phonon-induced conductance in scanning tunneling spectroscopy of gate-tunable graphene," *Nature Physics,* vol. 4, pp. 627-630, 2008.

[66] R. Decker, Y. Wang, V. Brar, W. Regan, H.-Z. Tsai, Q. Wu, W. Gannett, A. Zettl and M. Crommie, "Local electronic properties of graphene on a BN substrate via scanning tunneling microscopy," *Nanoletters,* vol. 11, pp. 2291-2295, 2011.

[67] A. Efros and B. Shklovskii, "Coulomb gap and low temperature conductivity of disordered systems," *Journal of Physics C: Solid State Physics,* vol. 8, pp. L49-L51, 1975.

[68] N. Levy, S. Burke, K. Meaker, M. Panlasigui, A. Zetttl, F. Guinea, A. Castro Neto and M. Crommie, "Strain-induced pseudo-magnetic fields greater than 300 Tesla in graphene nanobubbles," *Science,* vol. 329, pp. 544-547, 2010.

[69] D. Guo, T. Kondo, T. Machida, K. Iwatake, S. Okada and J. Nakamura, "Observation of Landau levels in potassium-intercalated graphite under a zero magnetic field," *Nature Communications,* vol. 3, p. 1068, 2012.

[70] H. Yan, Y. Sun, L. He, J.-C. Nie and M. Chan, "Observation of Landau-level-like quantization at 77K along a strained-induced graphene ridge," *Physical Review B,* vol. 85, p. 035422, 2012.

[71] L. Meng, W.-Y. He, H. Zheng, M. Liu, H. Yan, W. Yan, Z.-D. Chu, K. Bai, R.-F. Dou, Y. Zhang, Z. Liu, J.-C. Nie and L. He, "Strain induced one-dimensional Landau-level quantization in corrugated graphene," *Physical Review B,* vol. 87, p. 205405, 2013.

[72] W. Yan, W.-Y. He, Z.-D. Chu, M. Liu, L. Meng, R.-F. Dou, Y. Zhang, Z. Liu, J.-C. Nie and L. He, "Strain and curvature induced evolution of electronic band structures in twisted graphene bilayer," *Nature Communications,* vol. 4, p. 2159, 2013.

[73] K.-K. Bai, Y. Zhou, H. Zheng, L. Meng, H. Peng, Z. Liu, J. Nie and L. He, "Creating one-dimensional periodic ripples in a continuos mosaic graphene monolayer," *Physical Review Letters,* vol. 113, p. 086102, 2014.

[74] J. Lu, A. Castro Neto and K. Loh, "Transforming moiré blisters into graphene nano-bubbles," *Nature Communications,* vol. 3, no. 823, pp. 1-6, 2012.

[75] F. Calleja, H. Ochoa, M. Garnica, S. Barja, J. Navarro, A. Black, M. Otrokov, E. Chulkov, A. Arnau, A. Vázquez de Parga, F. Guinea and R. Miranda, "Spatial variation of a giant spin-orbit effect induces electron confinement in graphene on Pb islands," *Nature Physics,* vol. 11, pp. 43-47, 2015.

[76] G. Rutter, S. Jung, N. Klimov, D. Newell, N. Zhitenev and J. Stroscio, "Microscopic polarization in bilayer graphene," *Nature Physics,* vol. 7, pp. 649-655, 2011.

[77] E. McCann, "Asymmetry gap in the electronic band structure of bilayer graphene," *Physiscs Review B,* vol. 73, p. 161403, 2006.

[78] E. Castro, S. Novoselov, S. Morozov, N. Peres, J. Lopes dos Santos, J. Nilsson, F. Guinea, A. Geim and A. Castro-Neto, "Biased bilayer graphene: Semiconductor with a gap tunable by the electric field effect," *Physical Review Letters,* vol. 99, p. 216802, 2007.

[79] L. Brey and H. Fertig, "Emerging zero modes for graphene in a periodic potential," *Physical Review Letters,* vol. 103, no. 046809, pp. 1-4, 2009.

[80] L. Ponomarenko, F. Schedin, M. Katsnelson, R. Yang, E. Hill, K. Novoselov and A. Geim, "Chaotic Dirac billiard in graphene quantum dots," *Science,* vol. 320, no. 356-358, 2008.

[81] F. Libisch, C. Stampfer, Burgdöfer and J., "Graphene quantum dots: Beyond a Dirac billiard," *Physical Review B,* vol. 79, no. 115423, pp. 1-5, 2009.

[82] M. Katnelson, K. Novoselov and A. Geim, "Chiral tunnelling and the Klein paradox in graphene," *Nature Physics*, vol. 2, pp. 620-625, 2006.

[83] M. Crommie, C. Lutz, D. Eigler and E. Heller, "Quantum corrals," *Physica D: Nonlinear Phenomena*, vol. 83, no. 1-3, pp. 98-108, 1995.

[84] Z. Huang, J. Qu, X. Peng, W. Liu, K. Zhang, X. Wei and J. Zhong, "Quantum confinement in graphene quantum dots," *Physica Status Solidi Rapid Research Letters*, vol. 8, no. 5, pp. 436-440, 2014.

[85] A. Matulis and F. Peeters, "Quasibound states of quantum dots in single and bilayer graphene," *Physical Review B*, vol. 77, no. 115423, pp. 1-7, 2008.

5 STRIPED GRAIN BOUNDARIES IN SULFUR-INTERCALATED GRAPHENE: FORMATION AND MANIPULATION

This chapter deals with the formation of striped structures that act as grain boundaries (GBs) between domains after annealing the S/graphene/Ru(0001) system at high temperatures. The first section of this chapter explains the formation of stripes after the annealing process and the last section deals with the modification of the system with the STM tip, which allows the creation and controlled movement of the striped graphene GBs in both graphene/Ru(0001) and graphene/S/Ru(0001) regions.

5.1 STRIPED GRAIN BOUNDARIES SPONTANEOUS FORMATION IN GRAPHENE/S/RU(0001)

In the S/Ru(0001) system, increasing the temperature above 1000K leads to partial desorption of sulfur and a gradual decrease in the surface coverage [1]. This has been used in order to control the surface reconstruction of sulfur for its study as described in Chapter 3. When annealing graphene/S/Ru(0001) samples up to 1200K, sulfur desorption leads to the recovery of "non-intercalated" graphene/Ru(0001) at different points of the surface (Figure 5-1). This behavior is similar to that of graphene/O/Ru(0001), where annealing the sample up to 800K leads to the desorption of oxygen and the recovery of the original graphene/Ru(0001) surface [2].

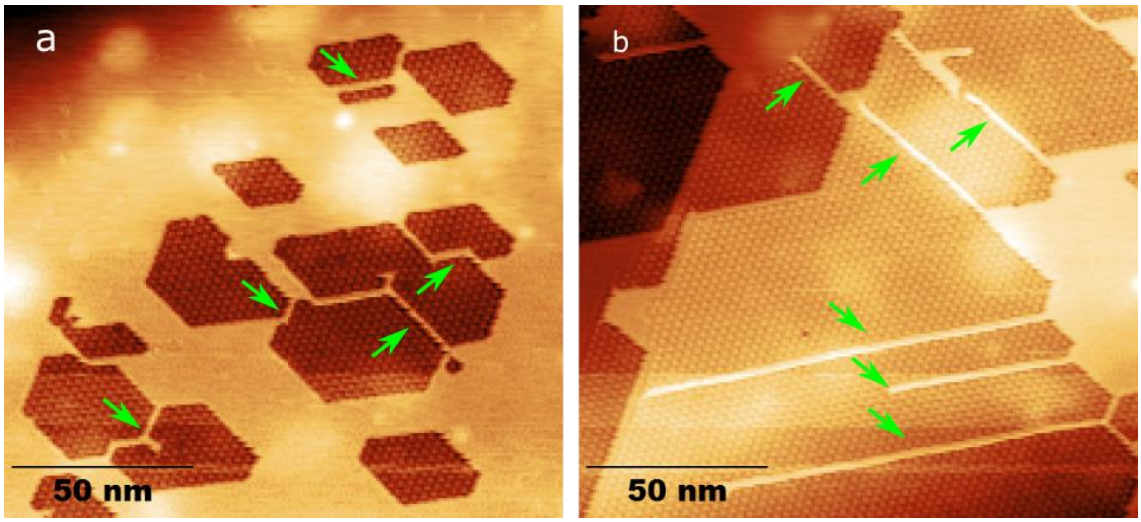

Figure 5-1 – Two STM topographic images of graphene/S/Ru(0001) after annealing at 1400K for 2min. (a) shows different graphene/Ru(0001) domains that form during the annealing process in a wide substrate terrace. Some of them have merged and are separated by GBs. (b) shows wider graphene/Ru(0001) domains near a step edge with GBs longer than 100nm. The grain boundaries are indicated by green arrows. The dark regions show the moiré pattern characteristic of graphene/Ru(0001) while the bright ones correspond to flat graphene/S/Ru(0001) regions. T=300K, V_s=100mV, I_t=20nA.

The recovered graphene/Ru(0001) domains appear after the annealing as a consequence of desorbing the intercalated sulfur, what makes graphene and ruthenium interact strongly again. The newly-formed graphene/Ru(0001) domains appear as islands with straight edges forming angles of 60º and 120º with each other, resulting in irregular hexagons and rhomboids. Interestingly, the length of the sides are always an integer multiple of the graphene/Ru(0001)

moiré lattice constant. Annealing for longer times results in a graphene/Ru(0001) background with graphene/S/Ru(0001) islands with the same shape characteristics.

Along with these islands, straight features with a width of one moiré unit cell (~3nm) appear (Figure 5-1). They appear as **bright** graphene/S/Ru(0001) stripes in a graphene/Ru(0001) background or the other way around. The moirés at the two different sides of these stripes do not match each other, i.e., we cannot connect the equivalent threefold-symmetry sites of one of them with those of the other with a straight line following their high symmetry directions (Figure 5-2). The relative displacement between moiré lattices at different sides of one of these stripes corresponds to 1/3 of the moiré unit cell. This implies that the graphene/Ru(0001) grains obtained after sulfur desorption can form three different translational domains. Likewise, the **dark** stripes crossing the graphene/S/Ru(0001) regions separate different translational domains of the graphene/S/Ru(0001) DW phase (see Figure 5-4). Since the stripes always separate two grains of different translational domains, we refer to them as striped grain boundaries.

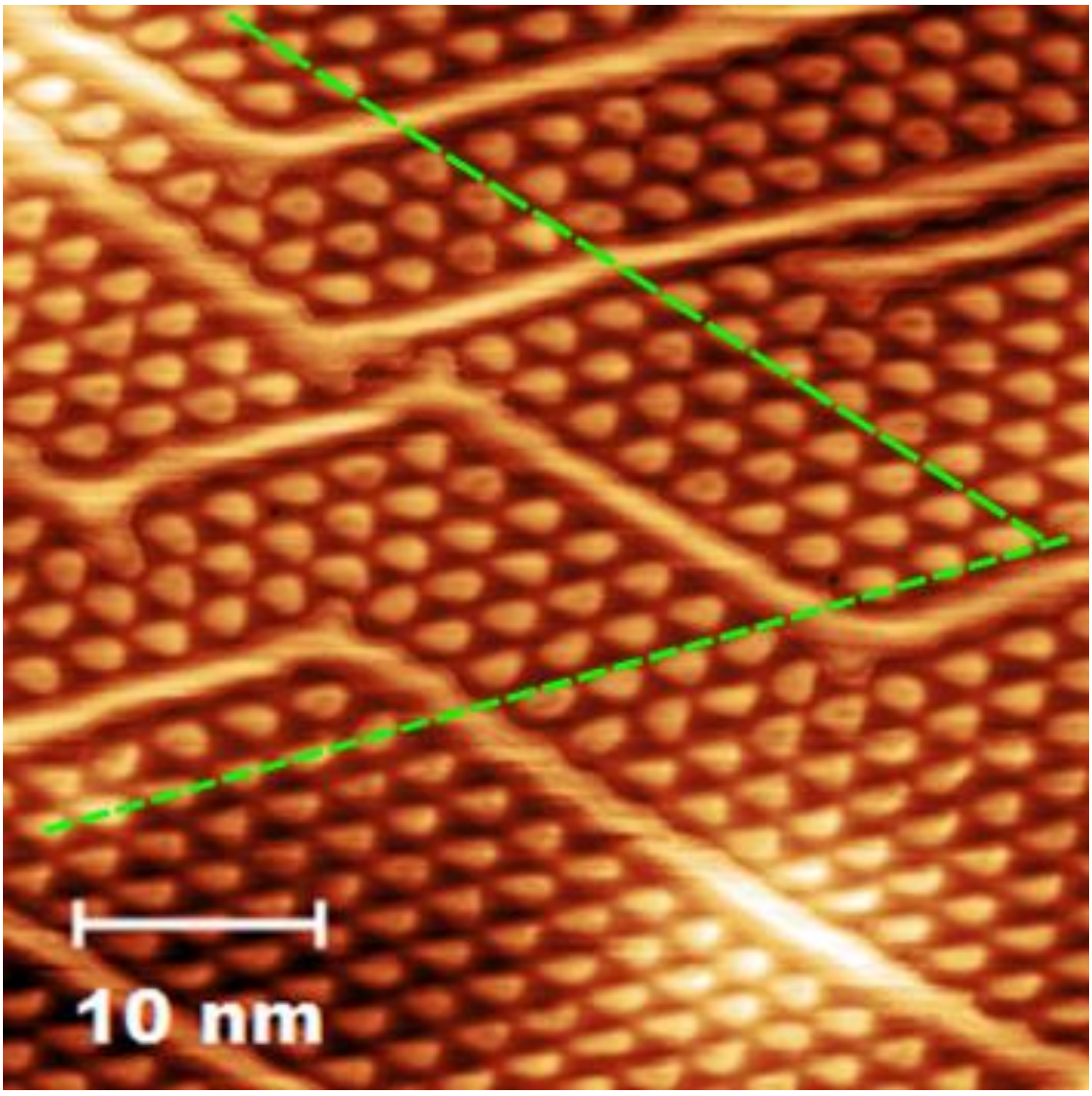

Figure 5-2 – Higher resolution STM topographic image of graphene/S/Ru(0001) taken at 300K after annealing at 1400K for 1min. Green lines follow two of the high symmetry directions and show the phase shift between domains: the line connecting the high parts of the moiré in one of the domains connects the low parts in each of the two other domains. S-intercalated regions appear as the bright GB lines 3nm wide. V_s=1V, I_t=300pA.

After annealing, the formation of different translational domains in graphene/Ru(0001) and graphene/S/Ru(0001) implies that the surface no longer presents a long-range translational order,

while the rotational symmetry is still the same as in the as-grown samples. The breaking of the long-range translational symmetry becomes more evident for longer annealing times, which lead to the desorption of larger quantities of sulfur, with the consequent size increase of the graphene/Ru(0001) domains. When two of these domains meet, a striped GB forms between them if their translational phase differs, in order to accommodate the lattice mismatch (Figure 5-2). These striped GBs appear as linear defects in the moiré lattice, ~3nm wide, separating two domains with a different translational phase in the moiré lattice. Formation of striped GBs between translational and rotational domains of graphene have also been observed in graphene/Cu(111) after intercalation of oxygen, both in the intercalated and non-intercalated zones, and their density and length increases with increasing annealing time [3]. They also form after europium intercalation in graphene/Ir(111) [4].

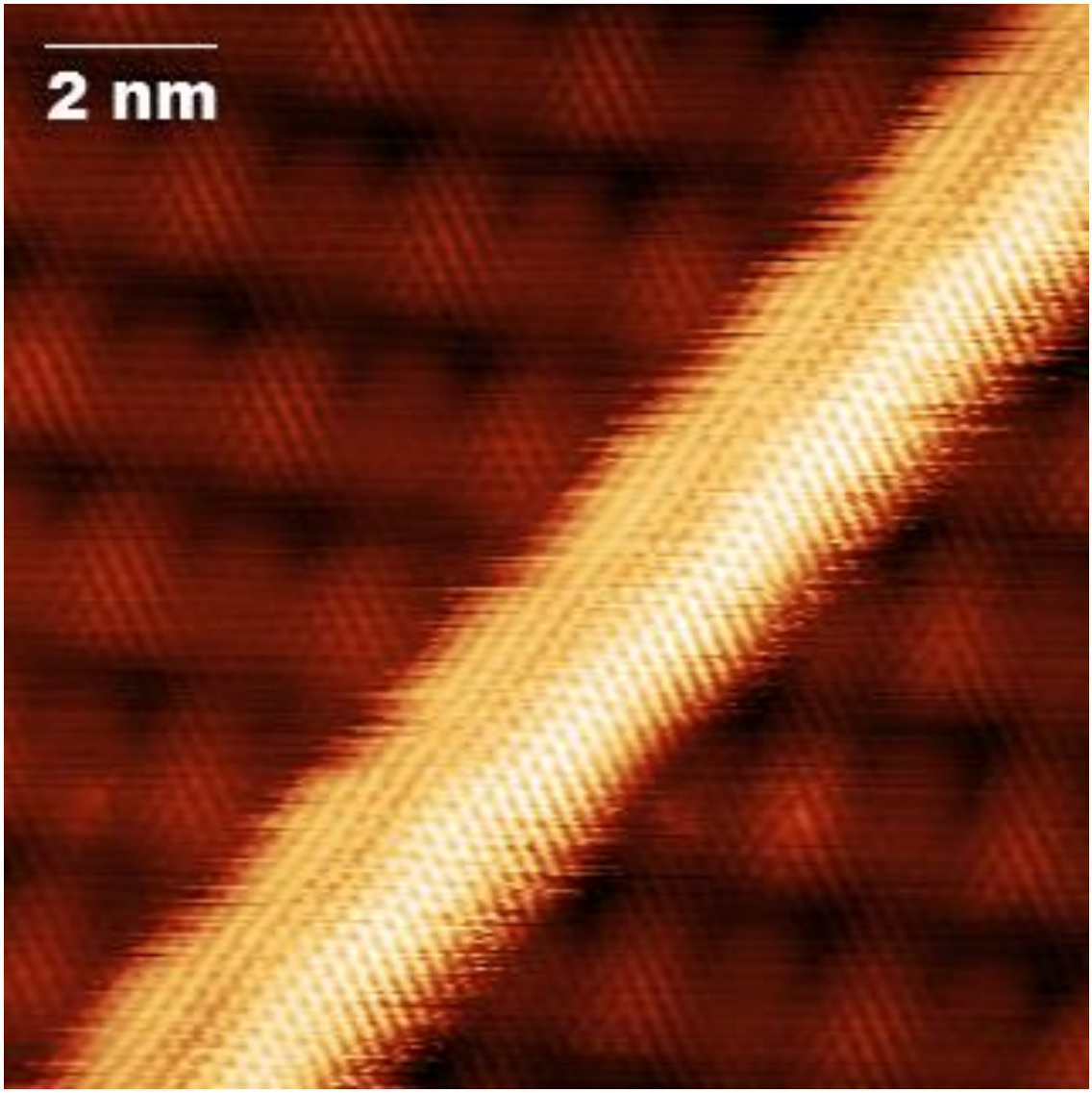

Figure 5-3 – Atomically resolved STM topography image of a GB (bright) separating two translational domains of the moiré superstructure in graphene/Ru(0001). The graphene/S/Ru(0001) sample was annealed at 1200K for 2min. T=300K, V_s=50mV, I_t=20nA.

The striped GBs observed after sulfur desorption are always parallel to the main symmetry directions of graphene/Ru(0001). They look like long wrinkles with apparent heights of 1.8±0.2Å with respect to the lower parts of the moiré (Figure 5-3). Their in-plane dimensions can be described in terms of the moiré lattice parameter of graphene/Ru(0001), $a_{moiré} = 2.7nm$.

Graphene/Ru(0001) GBs appearing after sulfur desorption are $a_{moiré}$ wide and $n \cdot a_{moiré}, n =$ 1,2,3, ... long.

In a similar fashion, we observe the appearance of "dark" striped GBs in the DW-intercalated areas of graphene/S/Ru(0001). In this case, the contrast of the GBs is the opposite to that of graphene/Ru(0001): we see these long defects as deep trenches in the graphene/S/Ru(0001) surface separating different domains of the almost flat moiré superstructure described in the previous chapter (Figure 5-4). The apparent dimensions of these GBs are in the same range of those appearing in graphene/Ru(0001), with an apparent depth of almost 2Å, one moiré unit-cell wide and n moiré unit-cells long (n=1,2,3,…). They usually start in the graphene/Ru(0001) domains formed after sulfur desorption, so they are likely linear regions of sulfur-free graphene/Ru(0001).

The three possible domains of graphene/Ru(0001) can be formed by shifting the graphene honeycomb lattice by one-third of its lattice parameter in one of its main symmetry directions. Such a shift in the graphene lattice will induce an equivalent shift in the moiré superstructure, displacing it by one third of its period in the same direction [5]. In the case of the moiré in graphene/Ru(0001), this is equivalent to changing the roles of the HCP, FCC and top regions at each side of the GB. The behavior of the moiré lattice of graphene/S/Ru(0001) when crossed by a GB is equivalent to that of GBs on graphene/Ru(0001). A GB introduces a phase shift in the moiré of 1/3 of its period along its main symmetry directions, resulting in the change of registry between graphene and Ru(0001) in the different parts of the moiré (Figure 5-4).

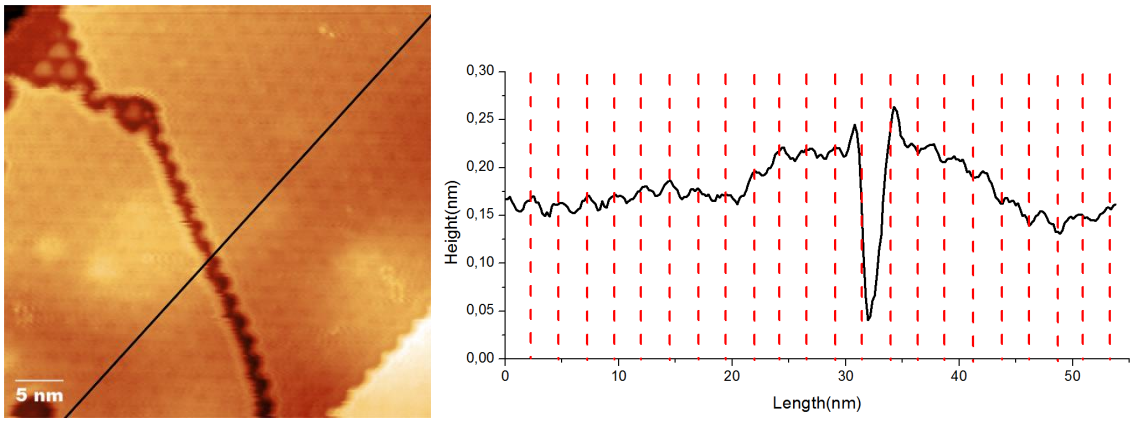

Figure 5-4 – (a) STM topographic image taken at 300K of a GB in graphene/S/Ru(0001).The sample was annealed at 1400K for 2min. The line crossing the figure corresponds to the profile in (b), where an array of dashed lines with the moiré periodicity shows the relative displacement of each zone in the different domains: the lines cross the high part of the moiré in the left domain and the low parts in the domain to the right of the wall. V_g=2.7V, I_t=1nA.

The contrast of the graphene honeycomb lattice in DW-intercalated graphene/S/Ru(0001) is very high and allows us to measure the phase shift the graphene lattice experiences at each side of a GB. Figure 5-5 shows that the relative displacement of graphene when crossed by one of these GBs changes is equivalent to that experienced by the moiré superstructure, as expected by geometric considerations regarding the moiré theory [5]. It is equivalent to moving the graphene lattice by 1/3 of its lattice constant along one of its main symmetry directions.

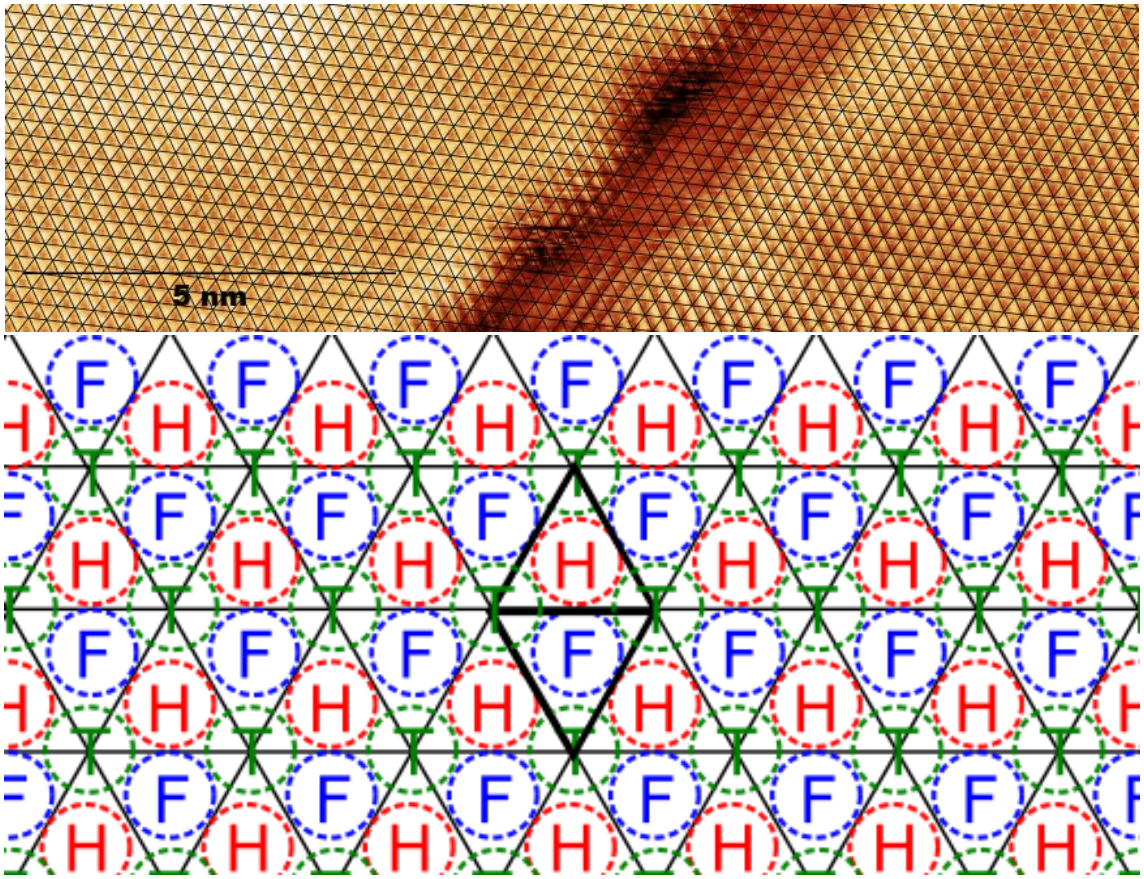

Figure 5-5 – (top) Topographic STM image taken at room temperature of a domain-wall intercalated region of graphene/S/Ru(0001) crossed by a "dark" GB. We have superimposed a triangular lattice to identify the position of the honeycomb hexagons relative to each other. In the left side of the GB, the dark spots are situated in the center of triangles that point upwards, while in the right side they fit in those which point downwards. V_g=50mV, I_t=20nA. (bottom) Schematic representation of a hexagonal reconstruction labelled as a function of their adsorption site on the substrate. H-HCP, F-FCC, T-Top. A triangular lattice has been superimposed in order to compare it with the upper image. The phase shift experienced by the honeycomb lattice of graphene is equivalent to the one that experiences the moiré superstructure.

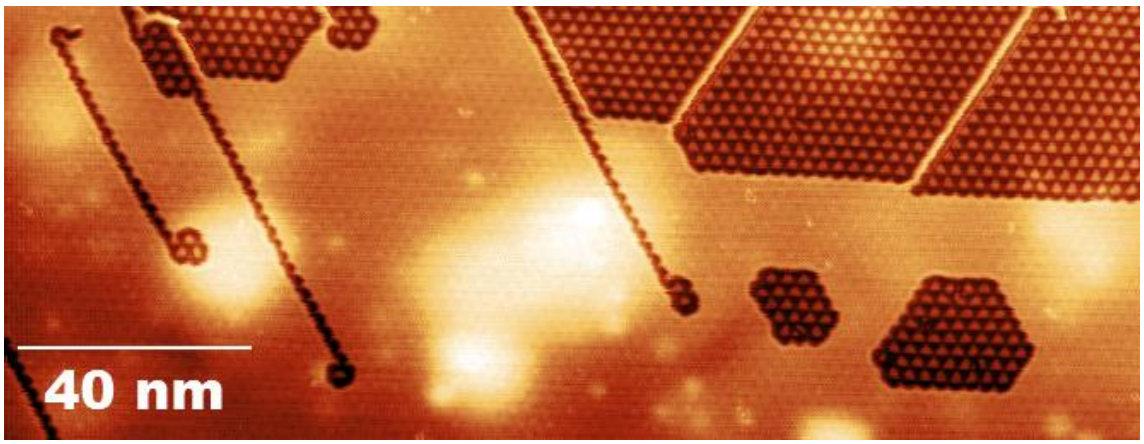

Figure 5-6 – STM topographic image of a graphene/S/Ru(0001) sample annealed at 1400K for 2min. Graphene/Ru(0001) domains start forming and GBs appear in both graphene/Ru(0001) and the remaining graphene/S/Ru(0001). T=300K, V_s=1V, I_t=0.2nA.

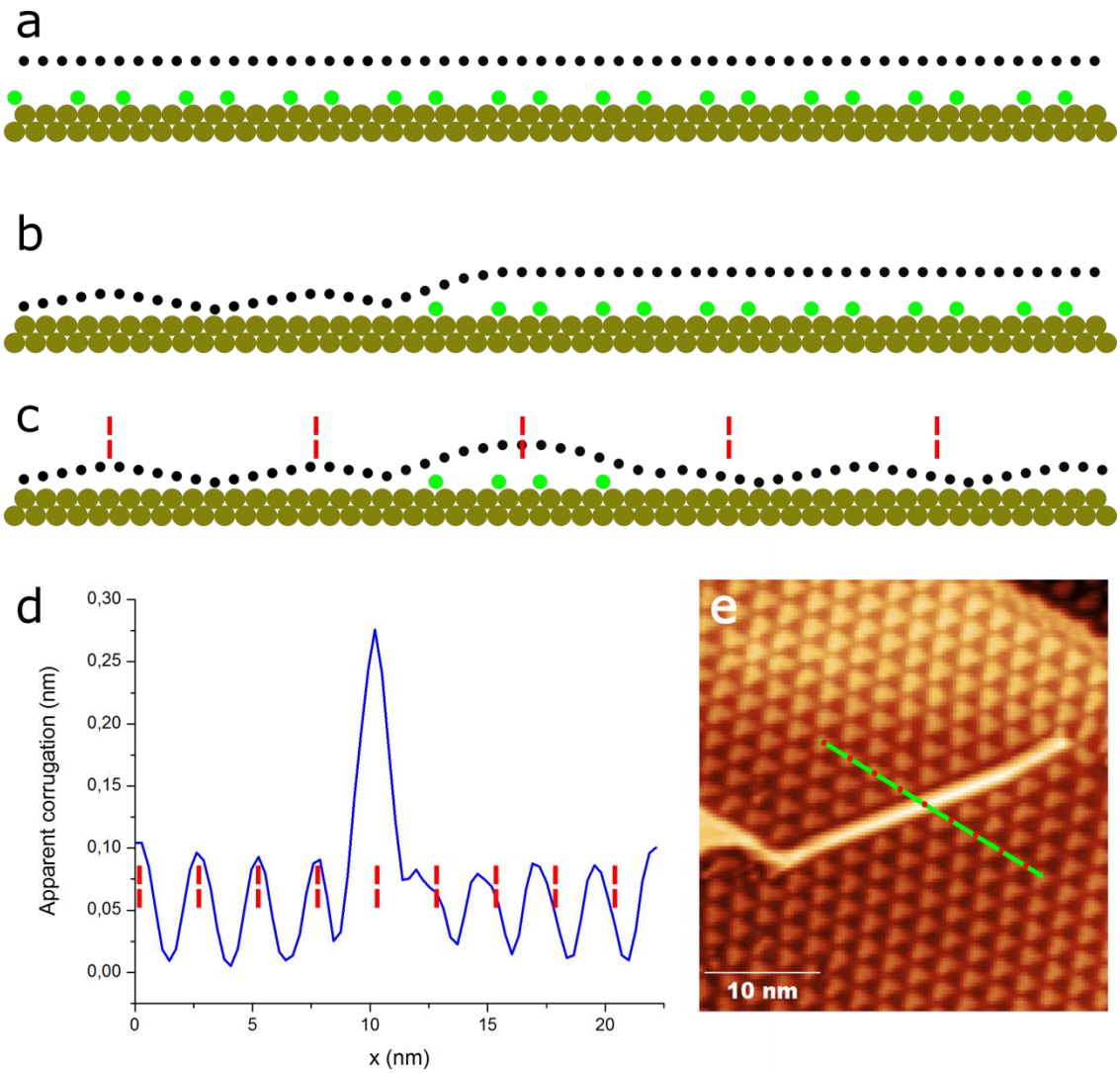

Figure 5-7 – (a, b, c) Schematic representation of the formation of a "bright" GB. Desorption of sulfur in graphene/S/Ru(0001) leads to the formation of two translational domains of graphene/Ru(0001) separated by a GB. Brown circles represent the two uppermost layers of Ru(0001), green circles the adsorbed sulfur in the DDW reconstruction, and black circles the graphene lattice, all cut in one of the main symmetry directions of Ru(0001). (a) Represents a completely intercalated region, (b) a intercalated/non-intercalated interface after desorption of part of the sulfur, and (c) the situation where two translational graphene/Ru(0001) domains meet after sulfur desorption, forming a grain boundary at the meeting point. (d) Shows a topographic profile extracted from the green line shown in (e), an STM topographic image of two graphene/Ru(0001) domains separated by a grain boundary (Anneal at 1200K for 1min, T=300K, V_s=1V, I_t=1nA). The red dashed lines in (c) and (d) are separated by the lattice constant of the moiré and follow the high parts of the left domain, showing the phase change when crossing the grain boundary.

Similar structures have been observed after europium intercalation in epitaxial graphene on iridium(111) and have also been related to tension relief mechanisms due to small lattice mismatches between adjacent domains [4]. In that system, the irregular islands and the striped structures are formed during intercalation of Eu at 720K, and not during desorption. In graphene/Eu/Ir(111) both kinds of stripes are thinner than the lattice parameter of the moiré of graphene/Ir(111), and the graphene lattice displacement is smaller than in our case, which is also reflected in a smaller relative displacement of the moiré at each side of the stripes. In the cited work, they identify two different types of edges in the graphene/Eu/Ir(111) islands, depending on the registry of graphene with the Ir(111) lattice, and it seems that one of them is favored over the other, since they observe irregular hexagonal islands with the longer sides corresponding to the preferred edge. In graphene/S/Ru(0001) we also observe two different kinds of edges (Figure 5-6), but we cannot assert the favoring of one over the other since they seem to be randomly

distributed (see, for example, Figure 5-1 or Figure 5-8). Apart from that, the resulting structure is very similar to the graphene/S/Ru(0001) case. We attribute the differences in strain and displacement to the strong interaction of graphene with ruthenium, which is much larger that with iridium, forcing graphene to anchor at very specific sites of the Ru(0001) surface.

We suggest that annealing a graphene/S/Ru(0001) sample leads to the desorption of sulfur and increases the mobility of the remaining intercalated atoms. The desorption of sulfur results in the recovery of graphene/Ru(0001) in extended areas as we have seen in the previous section, and also in the formation of graphene/Ru(0001) trenches that act as GBs between graphene/S/Ru(0001) domains (Figure 5-7).

The increased mobility of the sulfur layer during annealing also affects the domain structure of the c(2x4)-intercalated regions. The c(2x4) domains no longer have the striped appearance of the as-grown samples shown in the previous chapter, they have rather merged into wider areas, showing all the rotational domains and a relatively high amount of defects and dislocations (Figure 5-8). This indicates that the S atoms have moved and the whole surface has been reconfigured. We can conclude that the intercalated sulfur layer has a higher mobility at high temperatures, making it possible for the intercalated atoms to diffuse along the Ru(0001) surface, and cooling back the sample to room temperature blocks the movement of sulfur as the interaction of graphene prevents the sulfur atoms from moving.

Further study of these structures will be required in order to complete their characterization and their impact in the graphene properties. Wrinkles and curved features in 2D materials have been observed and studied for some time from different perspectives. Usually, when they appear disordered and with varying heights and widths, they are considered wrinkles or ridges that appear after applying a driving force such as temperature gradients [6] or mechanical stress [7] [8] [9], for example after exfoliation [3]; they appear as a strain-relief mechanism by means of the curvature of the 2D lattice at some point of the surface. When their shape is regular, periodic and can somehow be related to a topological alteration of the graphene lattice or its substrate, such as dislocations, grain boundaries or stacking faults, they are usually described as solitons in graphene [10] [11], as they behave as localized wavelets that preserve their shape and properties [12].

The appearance of wrinkles and soliton-like structures is not only interesting from the geometrical and topological point of view, their presence alters the properties of graphene in many different ways [13]. The electronic properties of wrinkled graphene have been theoretically studied because a change in the DOS is expected in the buckled region that can give rise to enhanced field emission properties of graphene [6]. Pseudo-Landau level quantization similar to that presented in Chapter 4 is present in corrugated graphene samples displaying linear wrinkles [14]. Topologically protected 1D conduction pathways are expected to form in the soliton boundary [11], and the thermal conductivity of graphene can depend on the presence of topological solitons [12].

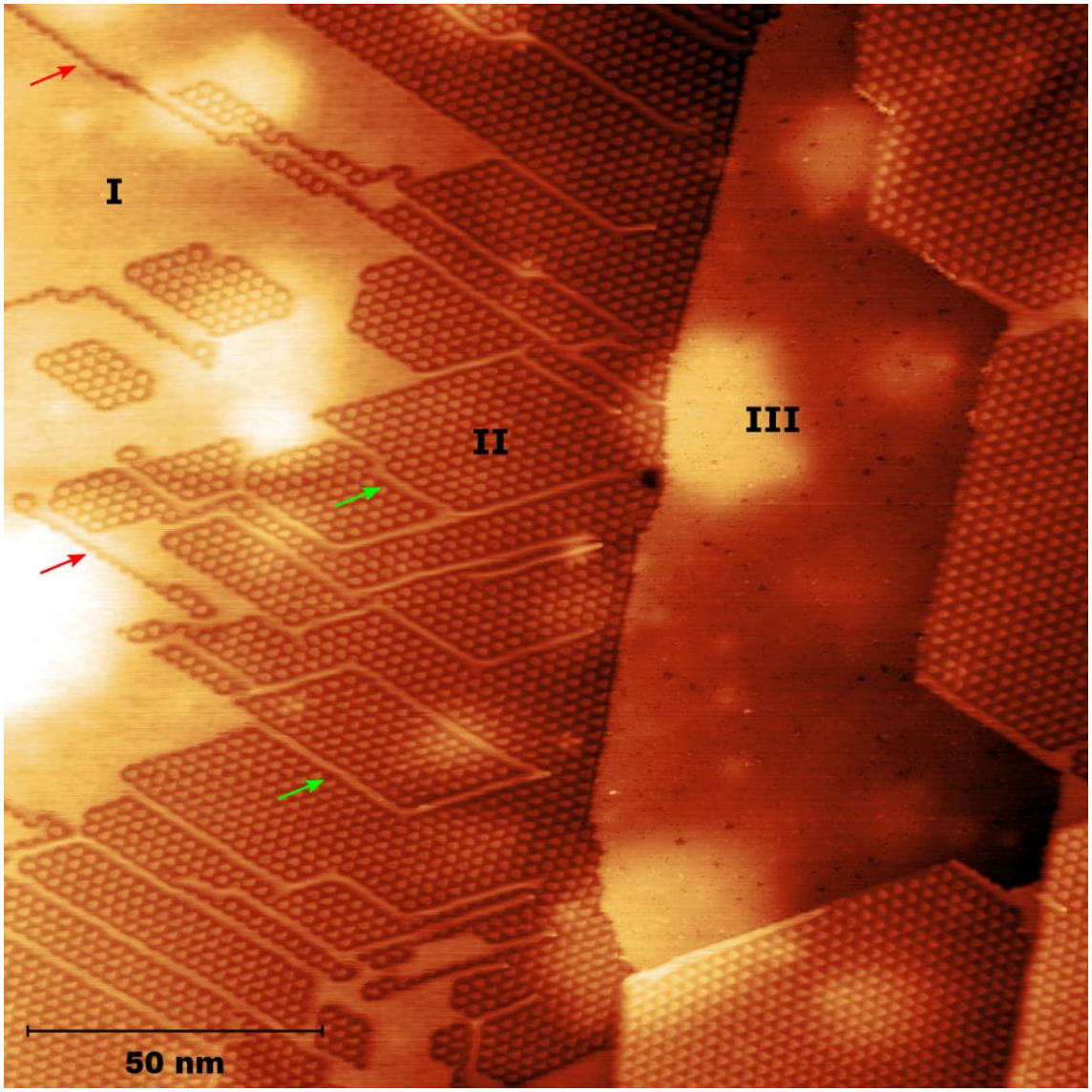

Figure 5-8 – STM topographic image taken at 300K of the overall appearance of an intercalated graphene/S/Ru(0001) sample after annealing at 1400K for 1min. The zones marked I, II, and III correspond respectively to DW-intercalated graphene, graphene/Ru(0001), and c(2x4)-intercalated graphene. "Bright" GBs crossing the moiré regions are marked with green arrows, and "dark" GBs in the DW-intercalated regions are marked with red arrows. The c(2x4)-intercalated domain (III) has lost the river-like appearance they usually have in the as-grown samples. V_g=1V, I_t=300pA.

5.2 FABRICATION AND MANIPULATION OF GRAIN BOUNDARIES IN GRAPHENE/RU(0001) AND GRAPHENE/S/RU(0001)

After annealing-induced sulfur desorption, the DW-intercalated graphene/S/Ru(0001) regions become less dense. In the case of S/Ru(0001), at coverages below 0.42ML the sulfur DWs present high mobility. As we showed in the previous section, in the case of graphene/S/Ru(0001), the domain walls remain static. Figures 5.9 and 5.10 show that by approaching the STM tip very close to the surface (few mV bias voltage and a high tunneling current, up to 40nA), we are able to manipulate the underlying sulfur layer, which results in the modification of the whole graphene/S/Ru(0001) system. The tip-surface interaction is sufficiently high to shift the sulfur atoms from their positions, what results in the formation of small graphene/Ru(0001) domains where the STM tip has passed. With these parameters, we are able to create graphene/Ru(0001) defects in the DW-intercalated graphene/S/Ru(0001) regions. As long as we follow the main

symmetry directions of the moiré lattice, these graphene/Ru(0001) regions will form GBs as the ones described in the previous section (Figure 5-9). We can also push the domain walls in the graphene/Ru(0001) by moving the tip parallel to them. In both cases, the resulting structures are stable and remain there for days at room temperature.

Soliton-like movement of wrinkles and GBs in graphene has already been observed in certain graphene systems, such as bilayer graphene in high electron currents in a transmission electron microscope (TEM) [11], by thermophoresis of mechanically transferred graphene/SiO_2 [6], and by means of a STM tip in multilayer graphene on SiC(0001) [8]. In this last case, they estimate that the pressure exerted by the STM tip in the topmost graphene layer reaches 5MPa, what leads to the displacement of graphene wrinkles and the formation of new ones. Nevertheless, the size and position of the so-formed wrinkles is not controlled, as they return in an elastic fashion to the former configuration [8].

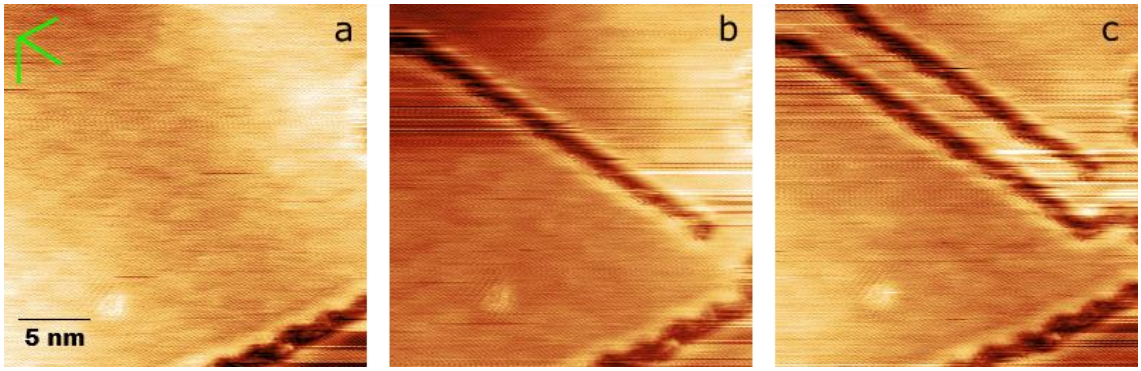

Figure 5-9 – Three consecutive STM topographic images of a graphene/S/Ru(0001) surface showing the creation of "dark" GB graphene/Ru(0001) stripes parallel to one of the high symmetry directions of the moiré superlattice (marked by green lines). (a) shows a domain-wall intercalated graphene region at a moment previous to the creation of any domain wall, while (b) and (c) show the result of approaching the tip to the sample at 5mV and 14nA and moving it parallel to one of the main symmetry directions. The lateral size of the GBs is ~3nm.

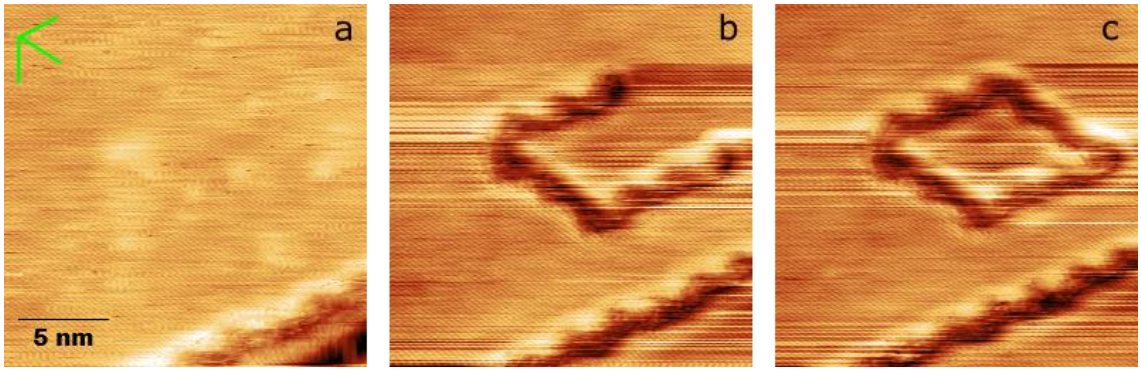

Figure 5-10 - Three consecutive STM images showing the creation of a closed structure following two of the high symmetry directions of the moiré superlattice (marked by green lines). (a) shows a domain-wall intercalated graphene region prior to the creation the structure, while (b) and (c) show the two steps of fabrication in order to get the resulting rhomb.

Using our patterning method, we are able to create parallel GBs as demonstrated in Figure 5-9, but we can also design closed structures as in Figure 5-10. The GBs created this way always form in the low areas of the moiré, just as those spontaneously formed during sulfur desorption. If we try to place two of them at a distance shorter than the moiré periodicity, very close to each other, we can create extended graphene/Ru(0001) domains (Figure 5-11). In all cases, the graphene lattice remains intact. We do not break the graphene's honeycomb lattice.

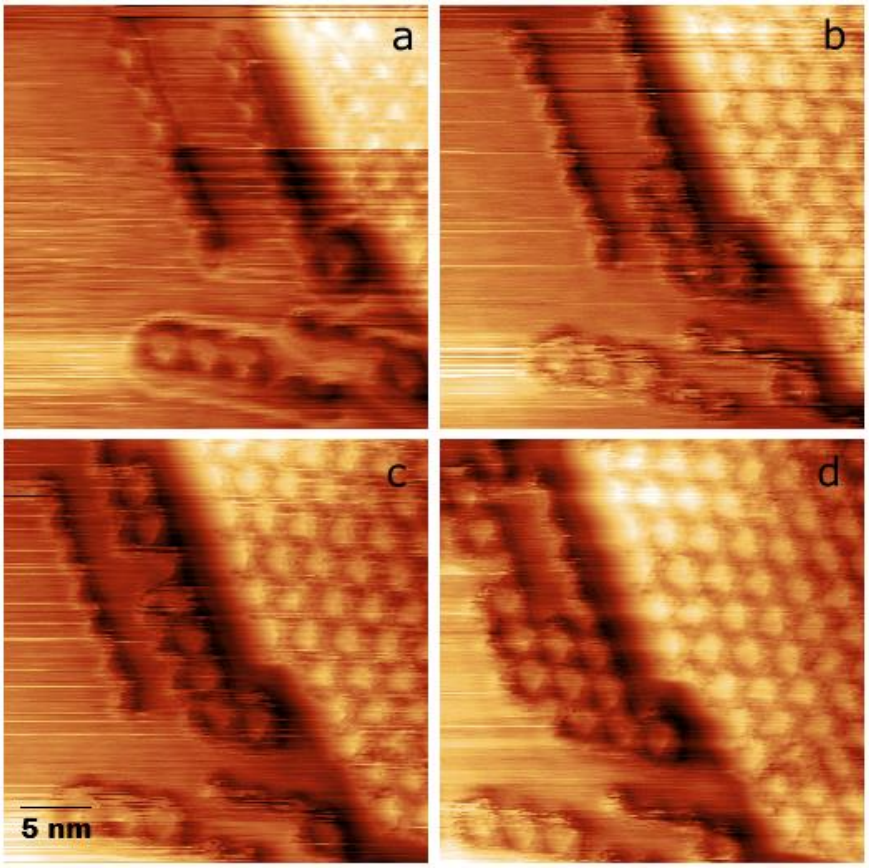

Figure 5-11 – Series of consecutive STM images after trying to place "dark" GBs into close proximity. When the distance between GBs is shorter than the moiré periodicity, we end up with a wide graphene/Ru(0001) domain.

In order to clarify what is actually happening, we performed a series of experiments to see if this intercalated layer modification has any kind of constraints.

The first thing we can observe is that we are not able to reproduce this effect when the intercalated layer presents a high density of DWs (before annealing); but we can always draw GBs in graphene/S/Ru(0001) when the DWs present a less dense structure (after annealing and sulfur desorption). This indicates us that in order to approach the graphene layer to the ruthenium we need some mobility in the sulfur layer, which we can only obtain after a controlled annealing as described in the previous section.

If we want to transfer a specific design to the intercalated layer, it is important to realize that, since the GBs are aligned with the tree high symmetry directions of the substrate crystal, we can only draw straight lines following those directions. Since they coincide with the high symmetry directions of the moiré pattern, it is easy to identify them even without atomic resolution. Trying to draw straight lines out of the high symmetry directions results in the formation of small graphene/Ru(0001) domains or short linear GBs parallel to the high symmetry directions (Figure 5-12).

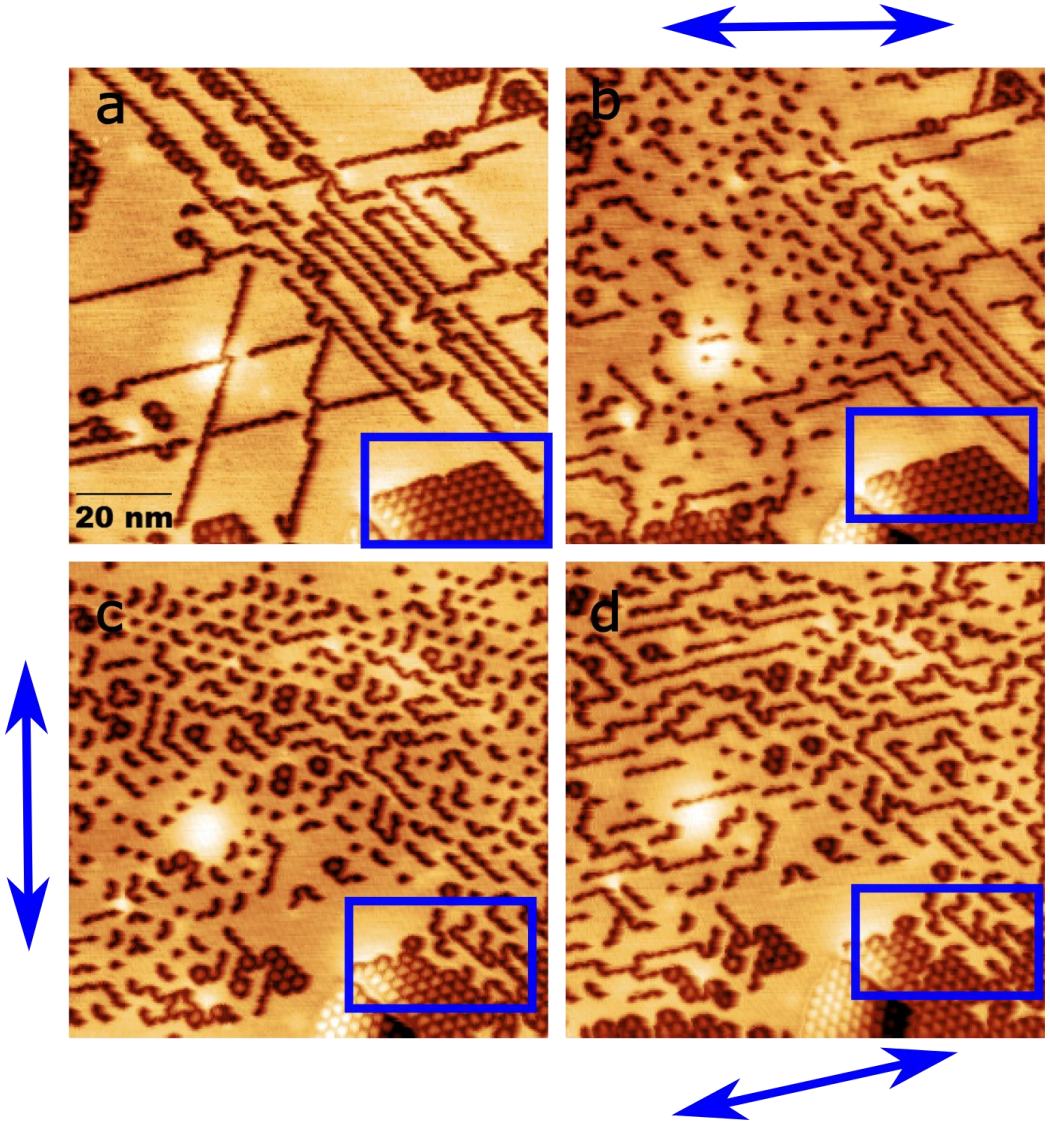

Figure 5-12 – Series of consecutive STM topographic images after (a) selective drawing (b) scanning the tip at 5mV and 40nA parallel to the horizontal axis, (c) scanning the tip at 5mV and 40nA parallel to the vertical axis, and (d) scanning the tip at 5mV and 40nA parallel to one of the high symmetry directions of the moiré lattice. Scanning the tip out of the high symmetry directions results in the formation of small (~2.7nm wide) graphene/Ru(0001) domains, while doing it along the high symmetry direction results in a higher amount of straight grain boundaries. The pre-existing GBs influence the result of each successive scan. Since the images and the patterning were performed at 300K, we suffer the effects of thermal drift, what separates the scanning direction from the set angle. The blue rectangles show a graphene/Ru(0001) domain that has been intercalated by sulfur islands after some scans. Imaging parameters: T=300K, V_s=1V, I_t=30nA.

We also studied the behavior of intersecting GBs in graphene/S/Ru(0001) as shown in Figure 5-13. When trying to draw a line through a high symmetry direction crossing an already existing one, the intersection is always broken. We attribute this behavior to the strain accumulation in the intersecting grain boundaries being too large. The graphene lattice can distribute the strain emerging from a change of direction and from a three-way intersection of GBs, but a fourth connection is always prevented. In the case of spontaneously created GBs on graphene/Ru(0001) we have also never observed that kind of intersection, when two of these lines cross, a gap always opens between them. When "drawing" these patterns, the intercalated sulfur must move somewhere else, increasing the density of sulfur atoms in the nearby areas. If the sulfur layer is too dense, it might push the sulfur layer and intercalate in graphene/Ru(0001) zones away from the tip, as shown in Figure 5-13.

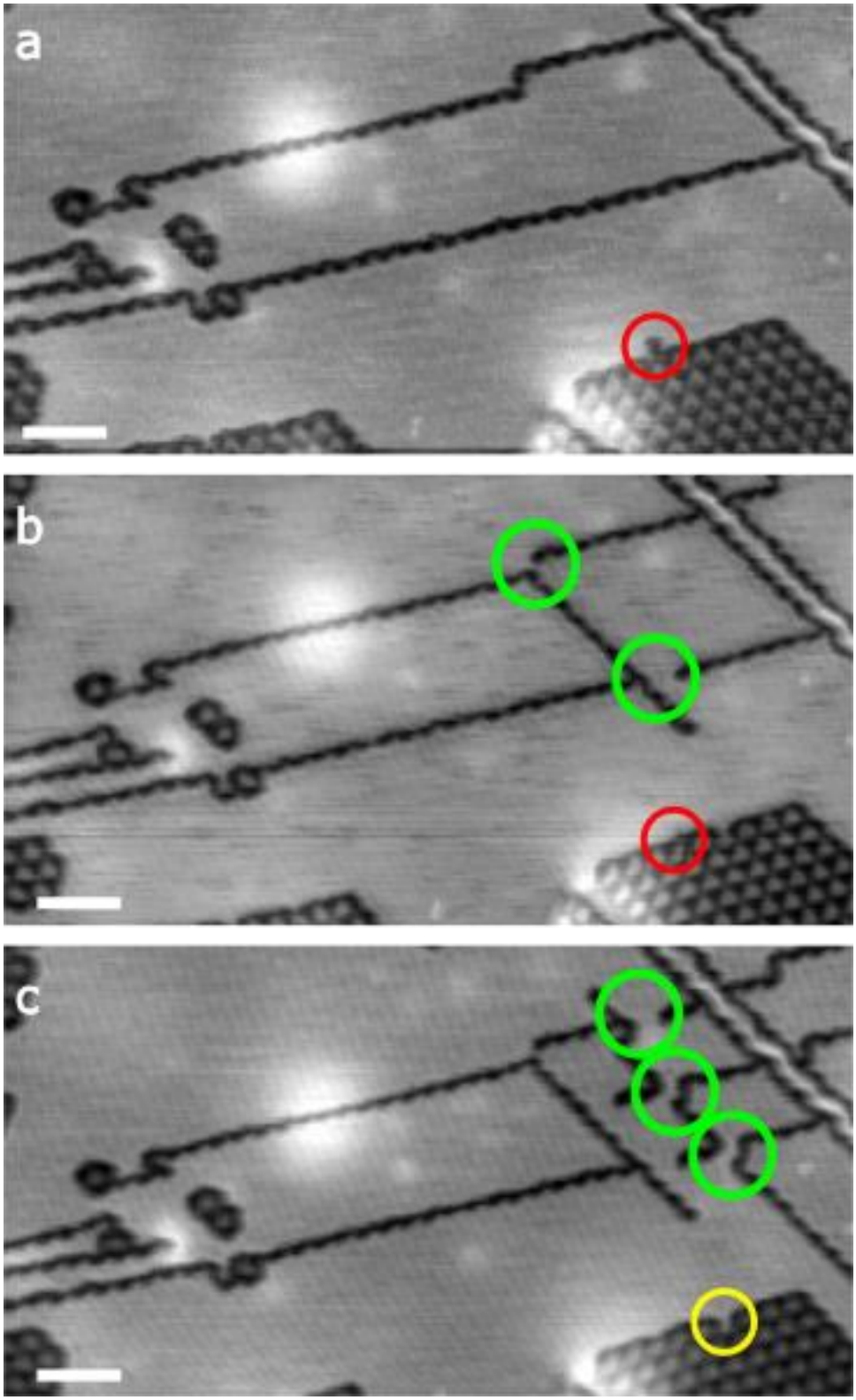

Figure 5-13 – Three consecutive STM images after trying to create intersecting GBs by the STM tip in graphene/S/Ru(0001) Whenever two GBs cross, a gap is open in one of the four ends of the intersection (circled in green). The red circles show how a graphene/Ru(0001) kink away from the tip disappears after creating the GBs. The yellow circle in (c) indicates the appearance of a graphene/S/Ru(0001) kink entering in graphene/Ru(0001) away from the tip after manipulating the surface with the STM tip a few nanometers away. T=300K, V_s=1V, I_t=30nA, scale bar=10nm. The sample was annealed at 1400K for 2min. The lines GBs fabricated at T=300K, 5mV and 40nA, and the images were taken at T=300K, 1V and 30nA

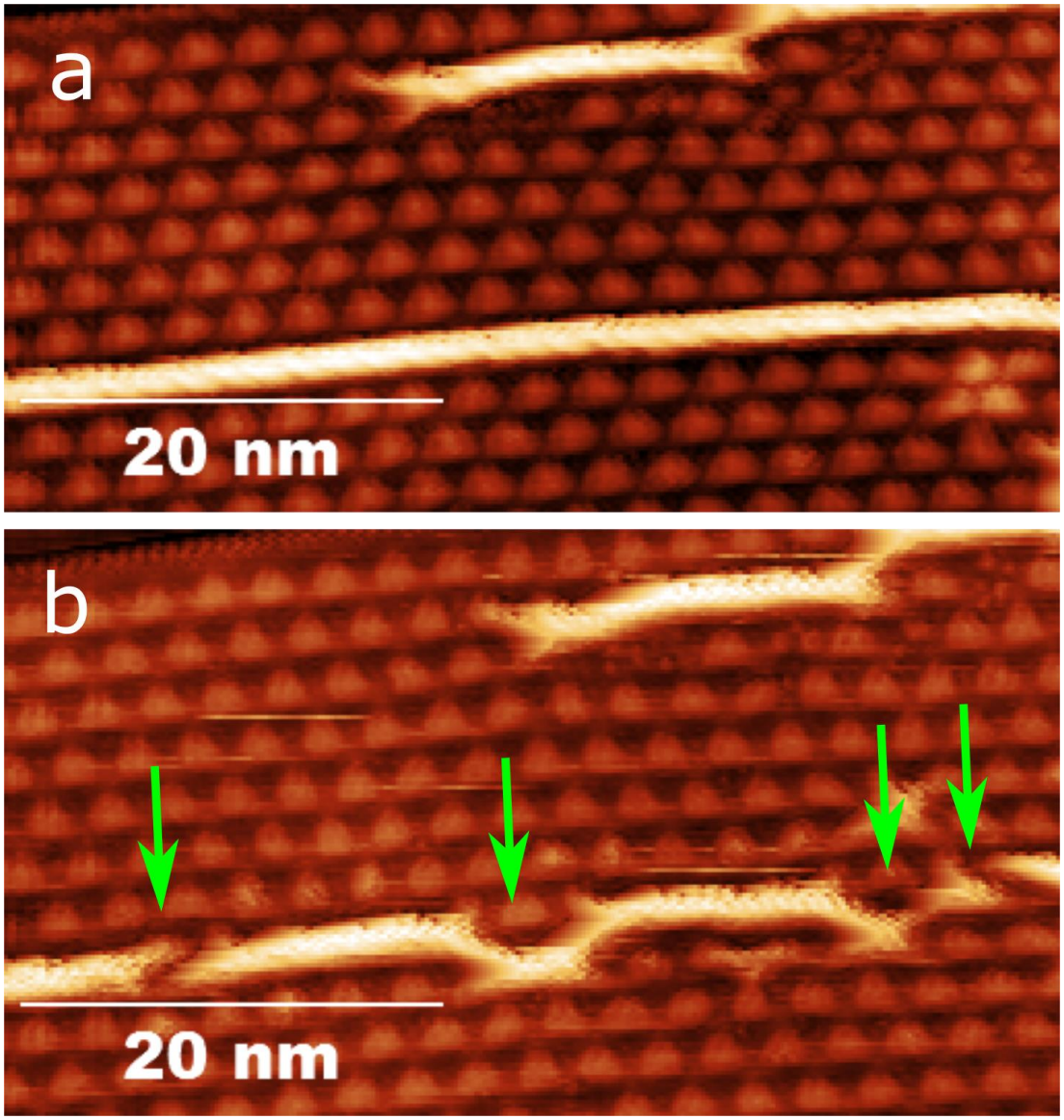

Figure 5-14 – Two STM topographic images of a graphene/Ru(0001) surface showing (a) a spontaneously created GB and (b) how it has been modified by scanning the tip at 5mV and 40nA along a vertical line crossing the GB at the spots marked by the green arrows. T=300K, V_s=1V, I_t=2nA.

Creating and manipulating "bright" GBs in graphene/Ru(0001) regions is not as easy as in graphene/S/Ru(0001), but it is still possible. Moving a long GB is complicated because it requires the joint displacement of the whole line. When we push the GB at specific places it results in the distortion of the GB (Figure 5-14). Continuously scanning the tip parallel to the GB results in the displacement of the GB as a whole, but it requires many scans and the GB may break at different points (Figure 5-15).

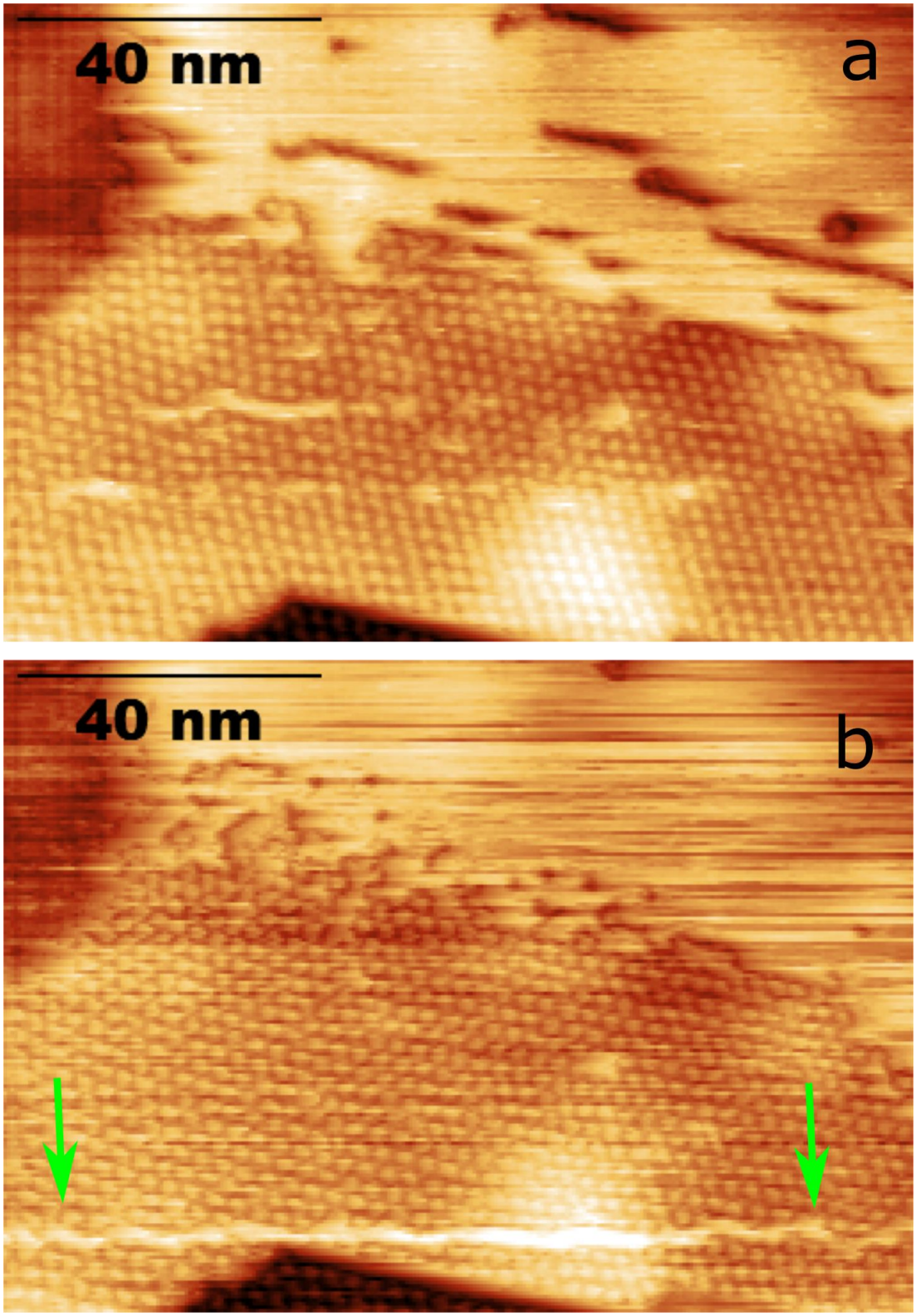

Figure 5-15 - Two STM topographic images of a graphene/Ru(0001) surface showing a graphene domain (a) after 2 top-down scans at 5mV and 40nA, and (b) after 10 top-down scans at 5mV and 40nA. The green arrows show two end of the newly-created GB. We pushed with the STM tip the intercalated sulfur of the graphene/S/Ru(0001) into the graphene/Ru(0001) domain, forming a new "bright" GB. T=300K, V_s=1V, I_t=1nA.

5.3 CONCLUSIONS

- Partial sulfur desorption after annealing of graphene/S/Ru(0001) samples leads to the recovery of graphene/Ru(0001), but it is no longer monocrystalline as it presents three different translational domains. When two different domains merge, linear "bright" grain boundaries, 3nm wide, appear between them. The graphene lattice is continuous over the grain boundaries. This can be considered a hexatic phase of graphene/Ru(0001) as it conserves the long-range orientational order while losing the long-range translational order.

- Partial sulfur desorption also leads to a decrease in the local coverage of DW-intercalated graphene/S/Ru(0001). "Dark" grain boundaries spontaneously form in this regions, and can also be created and modified with the STM tip, which can move the intercalated sulfur atoms and approach graphene and ruthenium into close proximity. Extended graphene/Ru(0001) domains can also be created this way.

- The increased sulfur mobility during the annealing process leads to the disruption of the elongated c(2x4) domains, that lose their river-like appearance and merge into wide domains.

5.4 REFERENCES

[1] S. R. Kelemen and T. E. Fischer, "Interaction of H2S with the Ru(001) surface," *Surface Science,* vol. 87, no. 1, pp. 53-68, 1979.

[2] H. Zhang, Q. Fu, Y. Cui, D. Tan and X. Bao, "Growth mechanism of graphene on Ru(0001) and O2 adsorption on the graphene/Ru(0001) surface," *Journal of Physical Chemistry C,* vol. 113, pp. 8296-8301, 2009.

[3] B. Yang, H. Xu, J. Lu and K. Loh, "Periodic grain boundaries formed by thermal reconstruction of polycrystalline graphene film," *Journal of the American Chemical Society,* vol. 136, pp. 12041-12046, 2014.

[4] S. Schumacher, D. Förster, M. Rösner, T. Wehling and T. Michely, "Strain in epitaxial graphene visualized by intercalation," *Physical Review Letters,* vol. 110, no. 086111, pp. 1-5, 2013.

[5] I. Amidror, "The superposition phase," in *The theory of the moiré phenomenon. Volume I: Periodic layers*, London, Springer-Verlag, 2009, pp. 165-190.

[6] Y. Guo and W. Guo, "Electronic and field emission properties of wrinkled graphene," *Journal of Physical Chemistry C,* vol. 117, pp. 692-696, 2013.

[7] A. Barboza, H. Chacham, C. Oliveira, T. Fernandes, E. Martins Ferreira, B. Archanjo, R. Batista, A. de Oliveira and B. Neves, "Dynamic negative compressibility of few-layer graphene, h-BN and MoS2," *Nano Letters,* vol. 12, pp. 2313-2317, 2012.

[8] G. Sun, J. Jia, Q. Xue and L. Li, "Atomic-scale imaging and manipulation of ridges on epitaxial graphene on 6H-SiC(0001)," *Nanotechnology,* vol. 20, p. 355701, 2009.

[9] H. Hattab, A. N'Diaye, D. Wall, C. Klein, G. Jnawali, J. Coraux, C. Busse, R. van Gastel, B. Poelsema, T. Michely, F.-J. Meyer zu Heringdorf and M. Horn-von Hoegen, "Interplay of wrinkles, strain and lattice parameter in graphene on iridium," *Nano Letters,* vol. 12, pp. 678-682, 2012.

[10] C. Woods, L. Britnell, A. Eckmann, R. Ma, J. Lu, H. Guo, X. Lin, G. Yu, Y. Cao, R. Gorbachev, A. Kretinin, J. Park, L. Ponomarenko, M. Katsnelson, Y. Gornostyrev, K. Watanabe, T. Taniguchi, C. Casiraghi, H.-J. Gao, A. Geim and K. Novoselov, "Commensurate-incommensurate transition in graphene on hexagonal boron nitride," *Nature Physics,* vol. 10, pp. 451-456, 2014.

[11] J. Alden, A. Tsen, P. Huang, R. Hovden, L. Brown, J. Park, D. Muller and P. McEuen, "Strain solitons and topological defects in bilayer graphene," *Proceedings of the National Academy of Sciences of the United States of America,* vol. 110, no. 28, pp. 11256-11260, 2013.

[12] J. Cheh and H. Zhao, "Solitons in graphene," *arXiv,* vol. arXiv:11073696v2, 2011 July 26.

[13] K. Xu, P. Cao and J. Heath, "Scanning tunneling microscopy of the electrical properties of wrinkles in exfoliated graphene monolayers," *Nano Letters,* vol. 9, no. 12, pp. 4446-4451, 2009.

[14] L. Meng, W.-Y. He, H. Zheng, M. Liu, H. Yan, W. Yan, Z.-D. Chu, K. Bai, R.-F. Dou, Y. Zhang, Z. Liu, J.-C. Nie and L. He, "Strain induced one-dimensional Landau-level quantization in corrugated graphene," *Physical Review B,* vol. 87, p. 205405, 2013.

CONCLUSIONES GENERALES

A la vista de los resultados obtenidos durante el trabajo experimental y de su correspondiente análisis, ambos discutidos extensamente en el cuerpo de esta tesis, se pueden extraer las siguientes conclusiones generales:

- La exposición de grafeno/Ru(0001) a H_2S, a temperatura ambiente en condiciones de ultra-alto vacío, resulta en la disociación de la molécula y la intercalación del azufre entre el grafeno y la superficie de Ru(0001). El primer objetivo de la tesis, es decir, la reducción de la interacción química entre el grafeno monocristalino fuertemente acoplado a un sustrato metálico mediante la intercalación de azufre, ha sido llevado a término (Capítulo 4).

- El azufre así intercalado forma una serie de estructuras geométricas y reconstrucciones superficiales, que se corresponden en cierta manera con las del sistema S/Ru(0001). Localmente, el recubrimiento nunca supera media monocapa de azufre, alcanzada en la reconstrucción c(2x4). Experimentos previos en el sistema S/Ru(0001) descritos en la literatura, sugieren que ese límite podría ser superado aumentando la temperatura de la muestra durante la exposición a H_2S.

- La presencia de grafeno previene la formación de ciertas estructuras existentes en el S/Ru(0001) y determina las estructuras de intercalación. El característico patrón de moiré del grafeno/Ru(0001) juega un papel importante en la geometría del sistema intercalado. Las fronteras entre grafeno/Ru(0001) y grafeno/S/Ru(0001), y entre los diferentes dominios de grafeno/S/Ru(0001), son abruptas y siguen las direcciones de alta simetría del grafeno/Ru(0001).

- La aparición de defectos topológicos puntuales en la superficie del grafeno tras la intercalación de azufre sugiere que estos son consecuencia del proceso de intercalación. En torno a ellos se pueden observar los patrones de interferencia característicos de los procesos de retrodispersión de electrones en sistemas bidimensionales.

- Los experimentos de STS muestran la aparición de una serie de resonancias en torno al nivel de Fermi cuyo origen no ha podido ser esclarecido. Su desplazamiento solidario en energía al cruzar las fronteras entre dominios con distinto recubrimiento de azufre muestran que el nivel de dopado tipo-n del grafeno se reduce a conforme la cantidad de azufre intercalado aumenta.

- Cuando se realiza un horneo de la muestra, se observa la formación de fronteras de grano lineales en el seno de los dominios de grafeno/Ru(0001) y grafeno/S/Ru(0001). Las fronteras de grano en los dominios de grafeno/S/Ru(0001) están formadas por regiones lineales de grafeno/Ru(0001) y viceversa. En ambos casos, su geometría está determinada por la simetría y las dimensiones del patrón de moiré. El desplazamiento

de las regiones de alta simetría del patrón de moiré muestra que los granos a cada lado de una frontera de grano son diferentes dominios traslacionales con la misma simetría rotacional. Esto es explicado a partir de la recuperación de la fuerte interacción C-Ru en diferentes zonas de la superficie a medida que se desorbe el azufre intercalado.

- En las muestras que han sido horneadas, la densidad de azufre intercalado es tal que permite desplazar sus átomos usando la punta del STM utilizando un voltaje punta-muestra muy bajo y una corriente túnel muy alta. Esto permite formar fronteras de grano de grafeno/Ru(0001) en dominios de grafeno/S/Ru(0001) con precisión nanométrica, siempre siguiendo las direcciones de alta simetría determinadas por el patrón de moiré del grafeno/Ru(0001). También se han conseguido modificar las fronteras de grano en grafeno/Ru(0001), aunque en este caso la técnica es menos efectiva debido a que la interacción entre la punta y la muestra es muy local.

GENERAL CONCLUSIONS

Taking into account the experimental data and the analysis carried out in this thesis, we can conclude de following:

- Exposure of graphene/Ru(0001) to H_2S, at room temperature and UHV conditions, results in the molecule dissociation and the subsequent intercalation of sulfur between graphene and the Ru(0001) substrate. The first goal of this thesis, i.e. decoupling graphene from a strongly interacting metallic substrate by sulfur intercalation, has been accomplished.

- The intercalated sulfur forms a series of geometric structures and surface reconstructions that can be directly related to those formed in S/Ru(0001). Local coverage never exceeds half a monolayer of sulfur, reached at the c(2x4). Previous experiments reported in literature for the s/Ru(0001) system, suggest that the half-monolayer limit could be overcome by increasing the sample temperature during H_2S exposure.

- The presence of graphene prevents the formation of some of the reconstructions observed in S/Ru(0001) and determines the intercalated structures. The characteristic moiré pattern of graphene/Ru(0001) plays an important role in the geometry of the intercalated system. The interfaces between graphene/Ru(0001) and graphene/S/Ru(0001), as well as in between different graphene/S/Ru(0001) domains, are abrupt and follow the high symmetry directions of the moiré pattern of graphene/Ru(0001).

- The appearance of local topological defects in the graphene's surface after intercalation suggest that they appear as a consequence of the intercalation process. Around them, the characteristic interference patterns attributed to backscattering processes can be observed.

- STS experiments show a series of resonances around the Fermi level whose origin is not clear. Their energy shifts when crossing between different coverage domains shows that the strong n-type doping of graphene/Ru(0001) is reduced as a function of the sulfur density.

- Annealing the sample results in the formation of linear grain boundaries among the graphene/Ru(0001) and graphene/S/Ru(0001). The grain boundaries separating graphene/S/Ru(0001) domains are formed by graphene/Ru(0001) stripes and vice-versa. In both cases it geometry is determined by the symmetry and dimensions of the moiré pattern. There is a translational phase-shift at each side of the grain boundaries but the rotational symmetry is conserved. This is explained in terms of the recovery of the strong C-Ru interaction in different zones of the surface after sulfur desorption.

- After annealing, the density of the intercalated sulfur layer is reduced. This allows us to displace the sulfur atoms with the STM tip using a low bias voltage and a high tunneling current. Using this technique we can create graphene/Ru(0001) grain boundaries in graphene/S/Ru(0001) domains with nanometric precision, always following the high symmetry directions dictated by the moiré pattern. We can also modify the grain boundaries in graphene/Ru(0001), but in this case the technique is less effective since the tip-surface interaction is very local.

APPENDIX A – LIST OF MATERIAL PROPERTIES

Ruthenium (Ru)	Atomic number: 44
	Electronic configuration: $[Kr]4d^7 5s^1$
	Lattice constants: a_{Ru}=2.706Å, c_{Ru}=4.282Å, hcp [1]
Ru(0001) surface	Lattice constant a=a_{Ru}=2.706Å [1]
	Step height= c_{Ru} /2=2.141Å
	1ML=$1.57 \cdot 10^{15}$atoms/cm^2
Sulfur (S)	Atomic number: 16
	Electronic configuration: $[Ne]3s^2 2p^4$
	Lattice constants(bulk): a_S=12.47Å, b_S=12.87Å, c_S=24.49Å [2]
S/Ru(0001)	(2x2) lattice constant: $a_{(2x2)}=2 \cdot a_{Ru}$=5.4Å
	(2x2) apparent corrugation(V_s=1V): 0.34Å
	(√3x√3)R30º lattice constant: $a_{(\sqrt{3}x\sqrt{3})R30^o}=\sqrt{3} \cdot a_{Ru}$=4.7Å
	(√3x√3)R30º apparent corrugation(V_s=1V): 0.26Å
	DDW lattice constants: $a_{DDW}=\sqrt{3} \cdot a_{Ru}$=4.7Å, $b_{DDW}=7 \cdot a_{Ru}$=18.9Å
	DDW apparent corrugation(V_s=1V): 0.21Å(HCP), 0.17Å(FCC)
	c(2x4) lattice constants: $a_{c(2x4)}=2 \cdot a_{Ru}$=5.4Å, $b_{c(2x4)}=4 \cdot a_{Ru}$=10.2Å
	c(2x4) apparent corrugation(V_s=1V): 0.17Å
Carbon (C)	Atomic number: 6
	Electronic configuration: $1s^2 2s^2 2p^2$
	Lattice constant (graphite, in-plane): $a_{Graphite}$=2.464Å [3] [4]
	Interlayer distance(graphite): $d_{graphite}=c_{Graphite}/2$=3.4Å [5] [4]
Free standing graphene	C-C bond distance: $d_{c\text{-}c}$=1.422Å [6]
	Lattice constant: $a_{Gr}= d_{c\text{-}c} \cdot \sqrt{3}/3$=2.464Å
Graphene/Ru(0001)	Lattice constant: $a_{Gr/Ru} \approx 10 \cdot a_{Ru}/11$=2.4Å [7]
	Moiré periodicity$\approx 10 \cdot a_{Ru}$=2.7nm [7]
	Moiré apparent corrugation(V_s=1V): 1Å [7]
Graphene/S/Ru(0001)	Lattice constant: $a_{Gr/S/Ru} \approx a_{Gr/Ru}$=2.4Å
	Moiré periodicity$\approx 10 \cdot a_{Ru}$=2.7nm
	Moiré apparent corrugation(V_s=1V): 0.1Å

A.1 REFERENCES

The crystallographic data was obtained from the following research papers. The data which is not referenced in the list is either derived from referenced data, or part of the results from this thesis.

[1] J. Arblaster, "Crystallographic properties of ruthenium," *Platinum Metals Review,* vol. 57, no. 2, pp. 127-136, 2013.

[2] A. Cooper, W. Bond and S. Abrahams, "The lattice and molecular constants in orthorhombic sulfur," *Acta Crystallographica,* vol. 14, p. 1008, 1961.

[3] Y. Baskin and L. Meyer, "Lattice constants of graphite at low temperature," *Physicall Review,* vol. 100, no. 2, p. 544, 1955.

[4] G. Bacon, "Unit-cell dimensions of graphite," *Acta Crystallographica,* vol. 3, pp. 137-139, 1950.

[5] G. Bacon, "The interlayer spacing of graphite," *Acta Crytallographica,* vol. 4, pp. 558-561, 1951.

[6] A. Castro Neto, F. Guinea, N. Peres, K. Novoselov and A. Geim, "The electronic properties of graphene," *Review of Modern Physics,* vol. 81, pp. 109-161, 2009.

[7] A. Vázquez de Parga, F. Calleja, B. Borca, M. Passeggi Jr., J. Hinarejos, F. Guinea and R. Miranda, "Periodically rippled graphene: Growth and spatially resolved electronic structure," *Physical Review Letters,* vol. 100, p. 056807, 2008.

APPENDIX B – RECIPROCAL SPACE REPRESENTATION OF THE DIFFERENT STRUCTURES APPEARING IN S/RU(0001) AND GRAPHENE/S/RU(0001)

Diffraction techniques and Fourier transforms of real-space images give us the possibility to study systems in the frequency domain. Their analysis gives important information regarding symmetries and ordering that cannot be easily extracted from real-space techniques. Nevertheless, interpretation of frequency domain images can become fairly complicated if the system under study presents more than one symmetry, different phases, superlattices or short-range order.

During this thesis we have extensively used phase-space techniques in order to characterize the surfaces of S/Ru(0001) and graphene/S/Ru(0001). We have relied mainly in the FFT of STM topographic images, but LEED difractograms have also been used to characterize the samples after preparation and before introducing them into the STM. These techniques allows us to differentiate between the different geometries at a glance. Once the symmetries and periodicities of the surface are defined by the analysis of the FFT, it is easier to identify the real-space geometries in the STM images.

The phase diagrams of S/Ru(0001) and graphene/S/Ru(0001) are fairly complex, presenting different symmetries, coexistence of different phases, a moiré superlattice and domain-wall networks. This results in complex frequency domain images that have to be properly analyzed in order to extract all the information they can give us.

This appendix is intended as a summary of the different frequency domain structures we found in S/Ru(0001) and graphene/S/Ru(0001). The different spots are color-coded in order to identify their relation with the different species in the samples. After a table with the schematics of the different FFT spot arrangements, some of them are presented along with the real-space STM topographic image and the corresponding FFT. In order to keep the same orientation as in the diagrams, some of the images were rotated with respect to their original configuration.

S/Ru(0001)
(2x2)

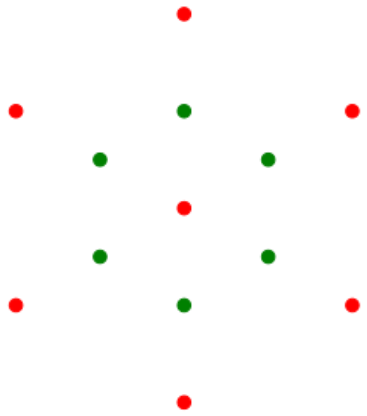

S/Ru(0001)
c(2x4) Single-domain

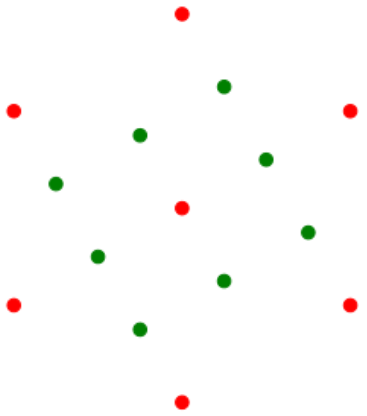

S/Ru(0001)
(R3xR3)

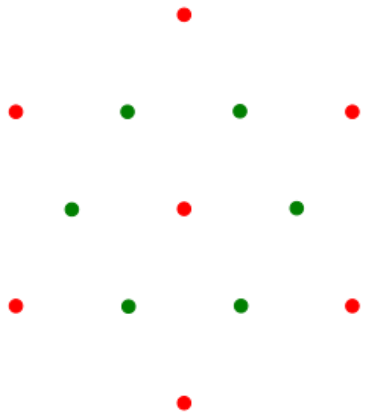

S/Ru(0001)
c(2x4) Two domains

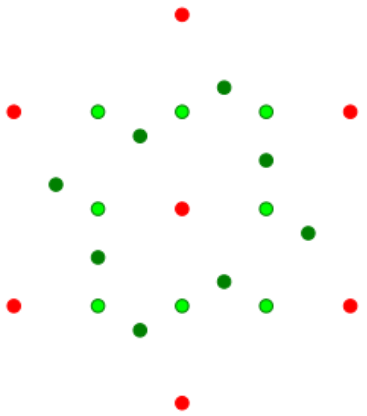

S/Ru(0001)
(2x2)+(R3xR3)

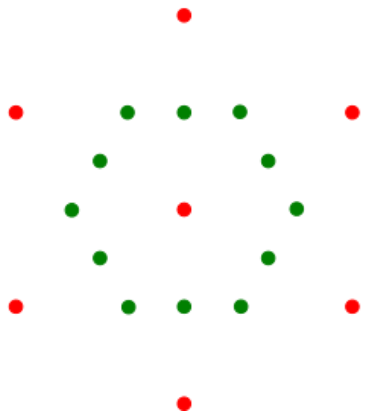

S/Ru(0001)
c(2x4) Three domains

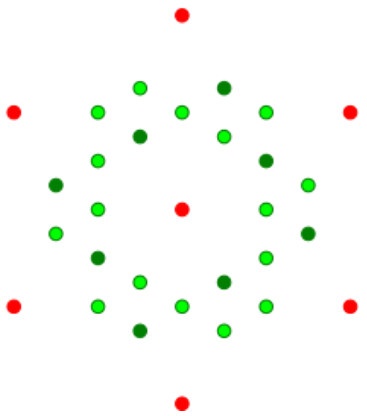

S/Ru(0001)
DDWs Single-domain

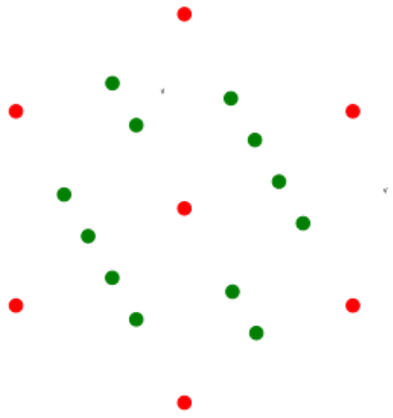

S/Ru(0001)
DDWs Three domains

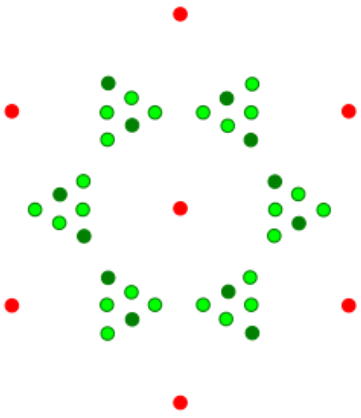

S/Ru(0001)
(R3xR3)+DWs

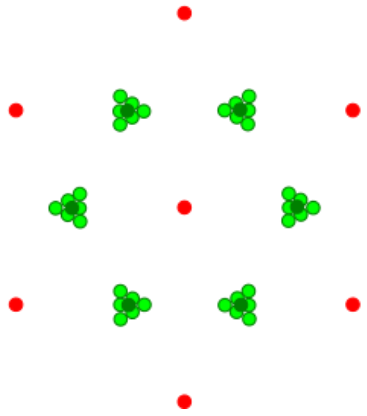

Graphene

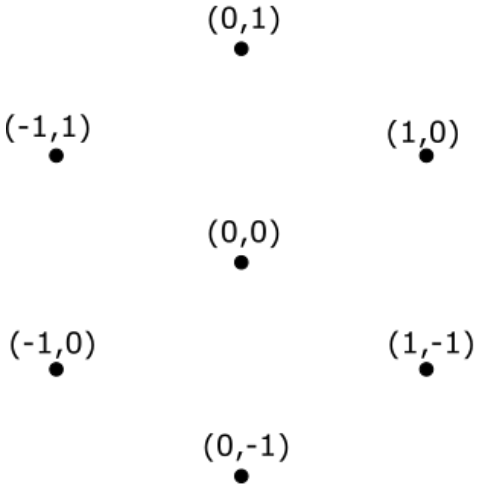

Graphene/Ru(0001)

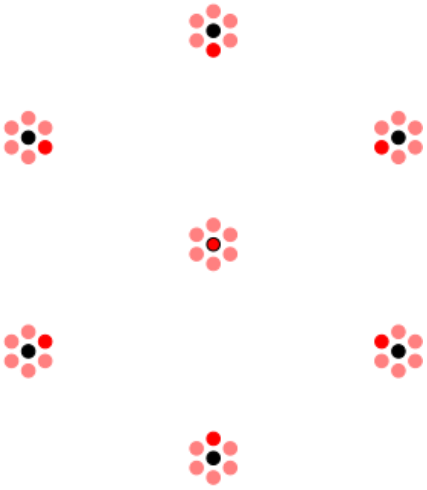

Graphene backscattering processes

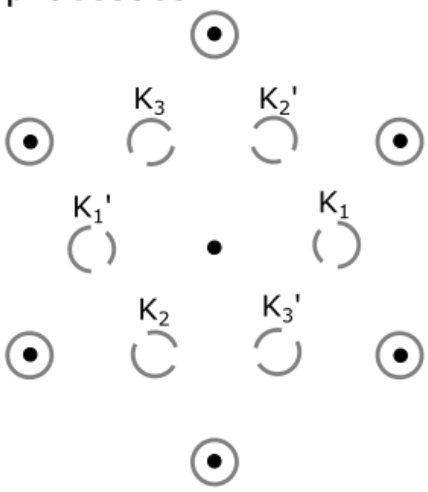

Graphene/S/Ru(0001)
Single-domain S DWs

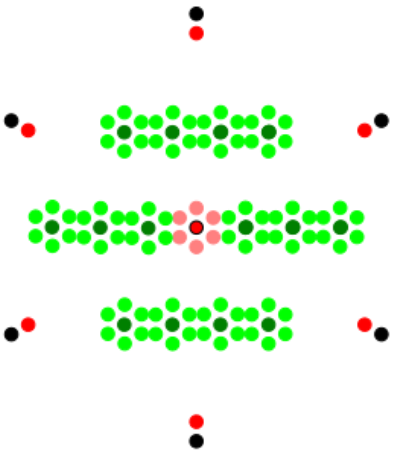

Graphene/S/Ru(0001)
Three domains S DWs

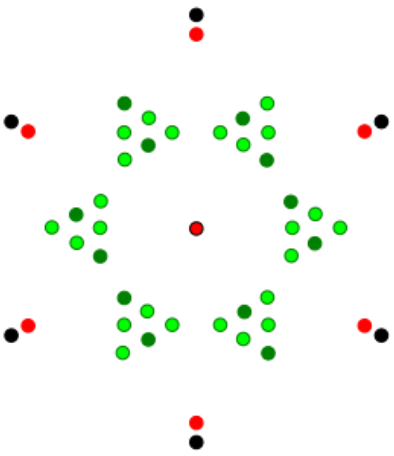

Graphene/S/Ru(0001)
with backscattering

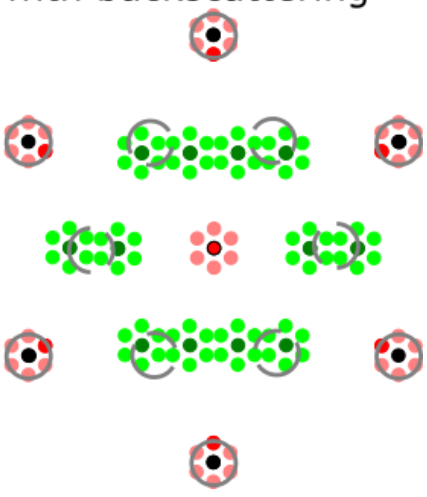

B.1 S/Ru(0001)

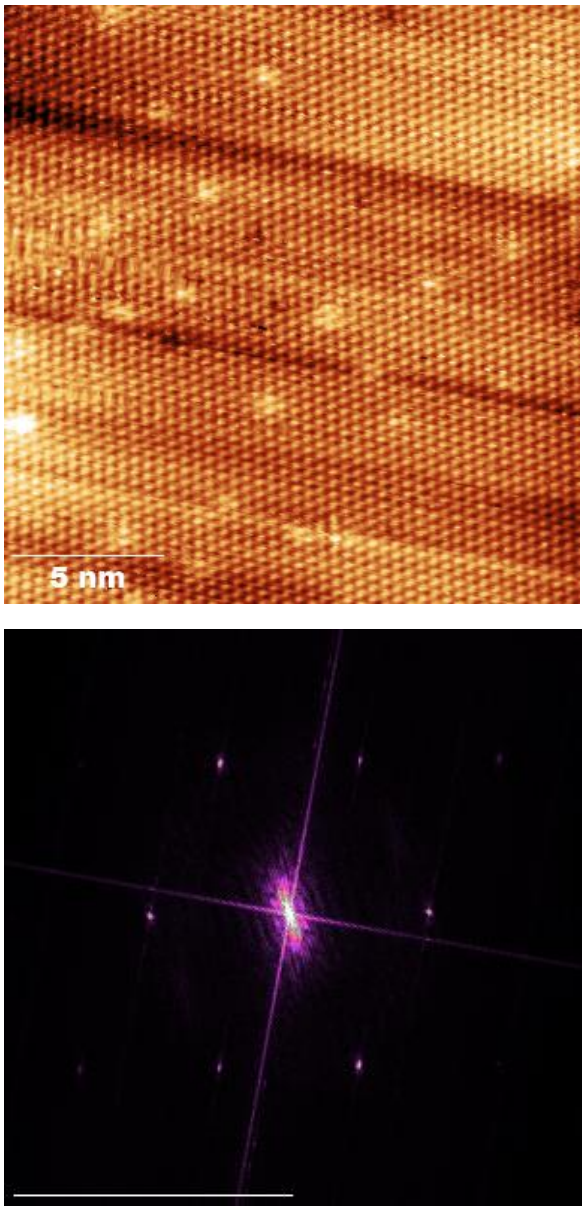

Figure B – 1 – STM, FFT and schematic representation of the FFT of a S/Ru(0001) surface in a (√3x√3)R30 reconstruction. T=300K, V_s=-100mV, I_t=1nA. FFT scale-bar: 5nm^{-1}.

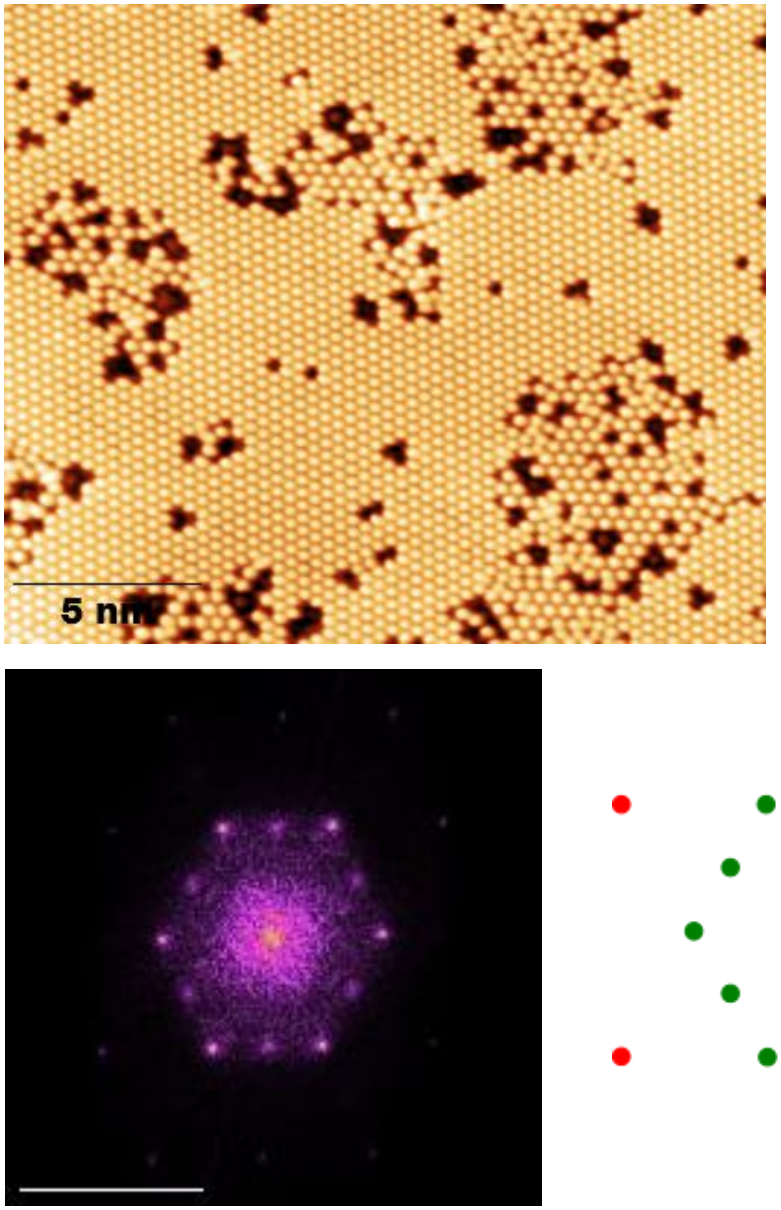

Figure B – 2 – STM, FFT and schematic representation of the FFT of a S/Ru(0001) surface with coexisting (2x2) and (√3x√3)R30 reconstructions. T=77K, V_s=2V, I_t=100pA. FFT scale-bar: 5nm^{-1}.

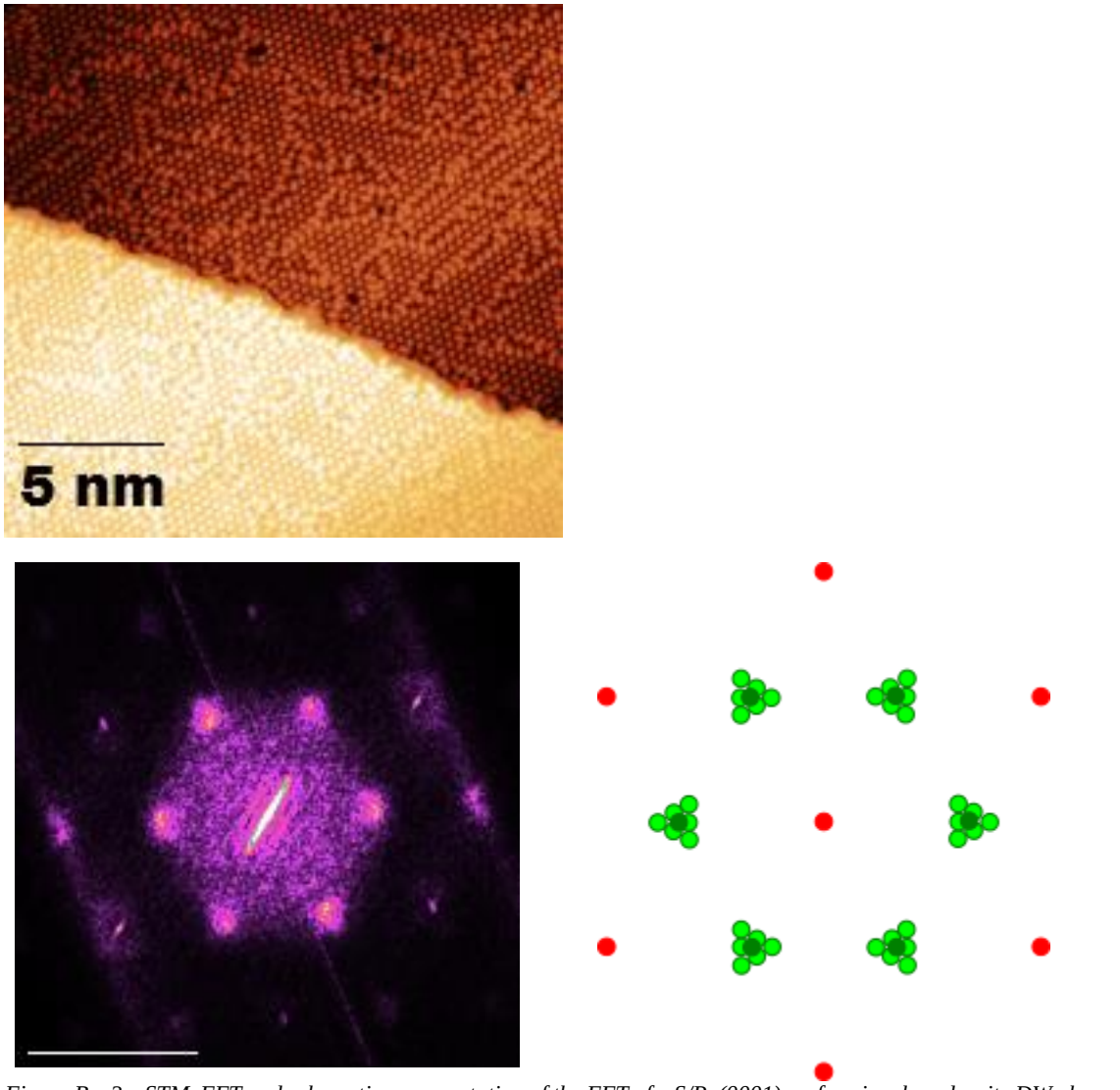

Figure B – 3 – STM, FFT and schematic representation of the FFT of a S/Ru(0001) surface in a low-density DW phase. T=77K, V_s=2V, I_t=100pA. FFT scale-bar: 5nm^{-1}.

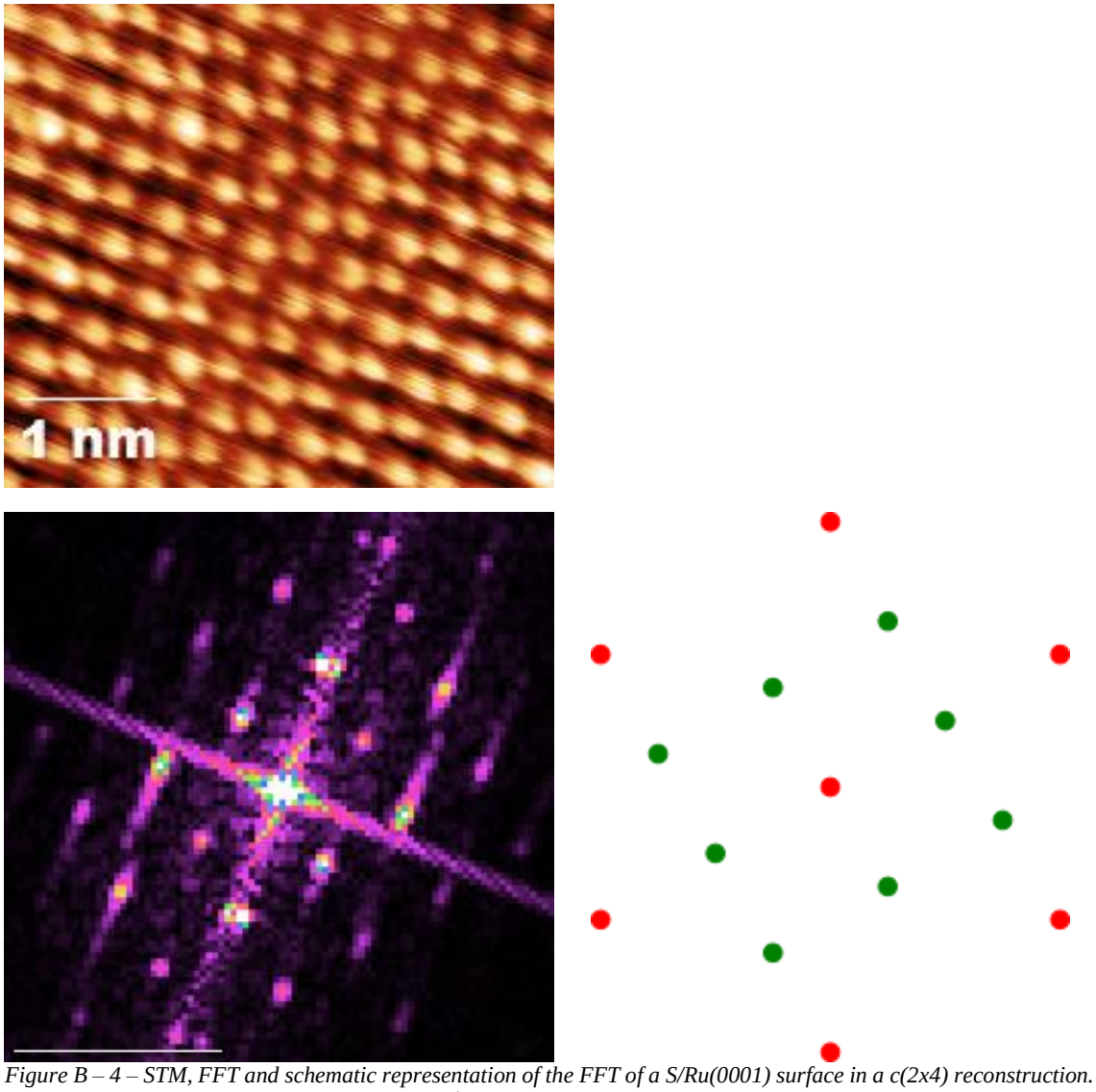

Figure B – 4 – STM, FFT and schematic representation of the FFT of a S/Ru(0001) surface in a c(2x4) reconstruction. T=300K, V_s=5mV, I_t=1nA. FFT scale-bar: 5nm^{-1}.

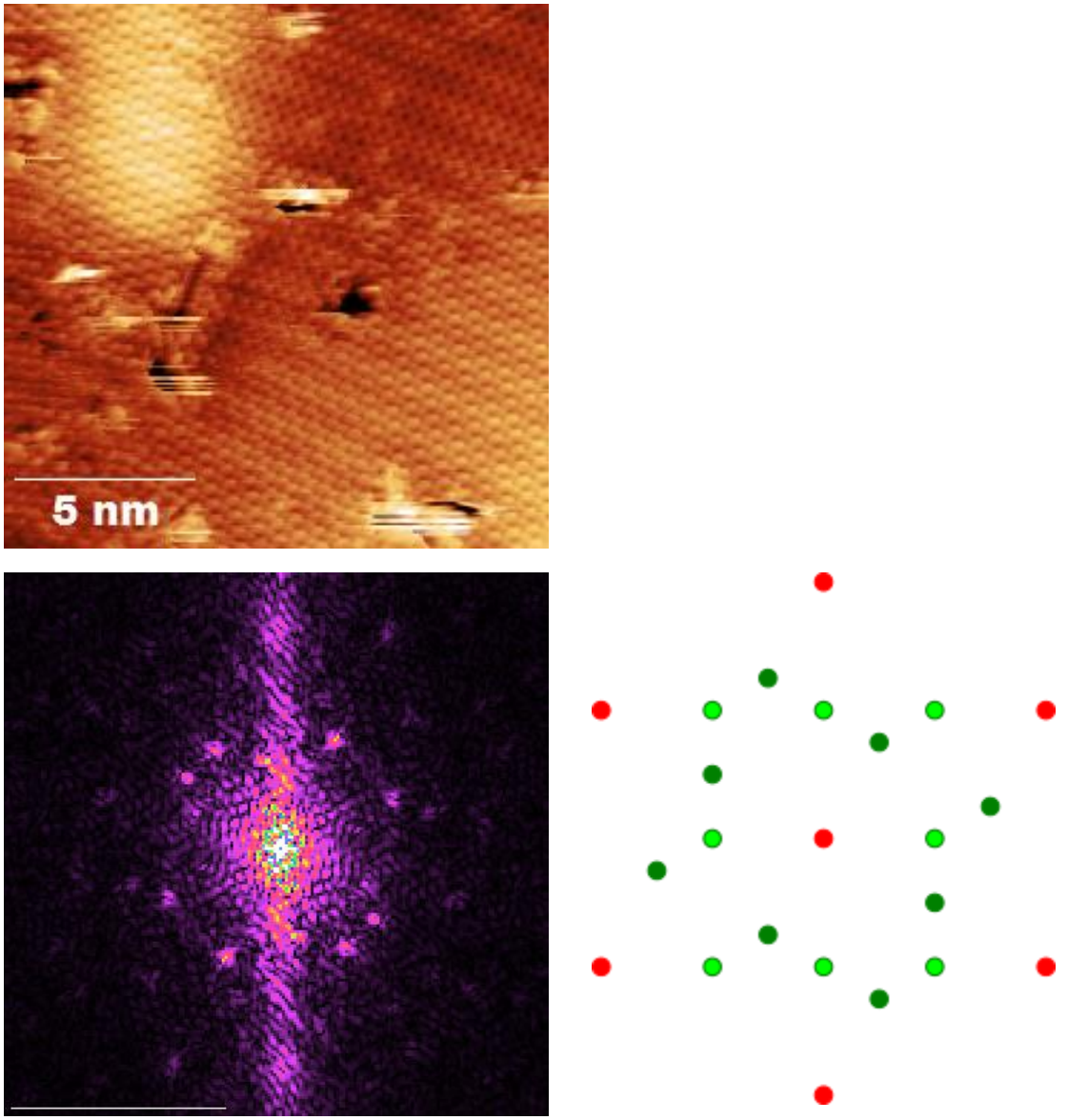

Figure B – 5 – STM, FFT and schematic representation of the FFT of a S/Ru(0001) surface in a c(2x4) reconstruction showing two domains. T=300K, V_s=5mV, I_t=1nA. FFT scale-bar: 5nm^{-1}.

B.2 GRAPHENE/S/RU(0001)

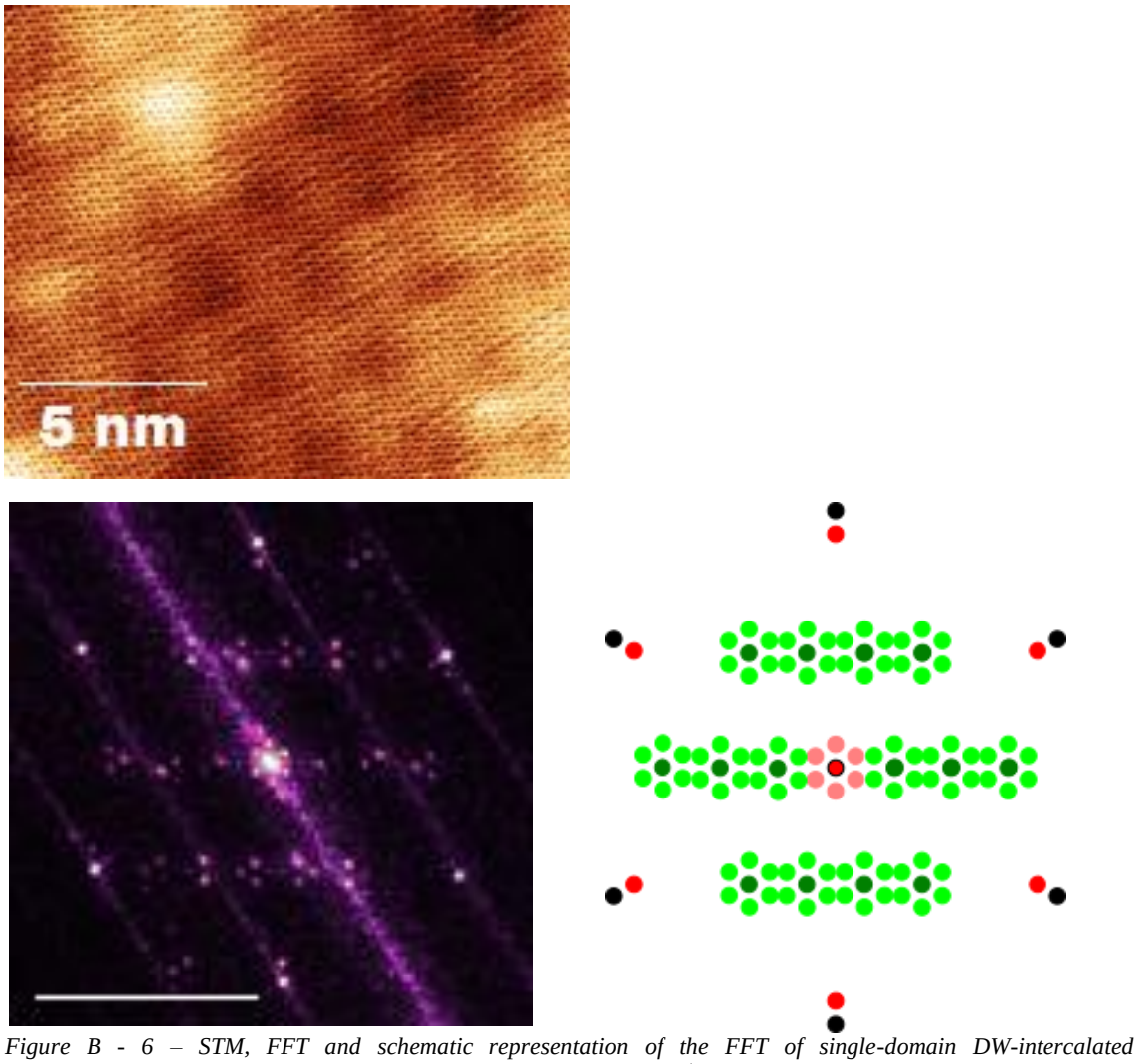

Figure B - 6 – STM, FFT and schematic representation of the FFT of single-domain DW-intercalated graphene/S/Ru(0001). T=300K, V_s=5mV, I_t=1nA. FFT scale-bar: 5nm^{-1}.